Study on Luminescent Properties of Eu^{2+} and Ce^{3+} in High Symmetry Crystal Field

高対称性結晶場における Eu^{2+} および Ce^{3+} の蛍光特性に関する研究

2016

Takuya Hasegawa

Doctoral Program in Advanced Materials Science and Technology
Graduate School of Science and Technology, Niigata University
8050 Ikarashi 2-nocho, Niigata 950-2181, Japan

Preface

The works of this thesis have been carried out under the guidance of Associate Professor Dr. Kenji Toda at Graduate School of Science and Technology, Niigata University, 8050 Ikarashi 2-nocho, Niigata 950-2181, Japan.

This thesis intendeds to reveal emission properties of Ce^{3+} and Eu^{2+} located at high symmetry crystal field, and to build a new effective and useful design concept for phosphor materials.

The author wishes that the achievements obtained from this work provide a positive information for the further development of luminescent materials.

Takuya Hasegawa

Graduate School of Science and Technology, Niigata University

8050 Ikarashi 2-nocho, Niigata 950-2181, Japan

September, 2016

Contents

Contents

Chapter 1

General introduction

Commercial technologies for lighting device were based on a natural gas that served thousands of streets, offices, factories, and homes at the beginning of the 19th century. The gas-lights were replaced by incandescent bulbs first demonstrated in the late 19th century.[1] Moreover, fluorescent and compact fluorescent lamps became widely available in the 1950s and 1990s, respectively. Along with high intensity discharge lamps, they offer a longer lifetime and lower power consumption than incandescent sources, and have become the mainstream lighting technology. However, in times of economic crises, shortage of resources and the increased sensibility of people to their environment, there is a large demand for new materials or improved applications to enhance energy and cost efficiency together with environmental compatibility.

In 1993, Nakamura (Nichia Corporation) has been developed the demonstration of InGaN based a blue light emitting diode (LED) with a high brightness and high efficacy along with earlier materials advances by Akasaki and Amano group.[2-4] The bright blue LED can provides a phosphor converted white-LED by combining with blue-light excitable phosphors. The white-LED has many advantages over the problems of the conventional lighting devices, such as a high efficiency, a long life, compactness, low power consumption, low toxicity and designable features.[5,6] In 1995, the most basic white-LED system, which applies blue-LED chips with Ce^{3+}-doped yttrium aluminum garnet (YAG:Ce) yellow-emitting phosphor, was discovered and first enabled to be commercially available.[7,8] The market for white-

LEDs is growing rapidly in various applications such as a large size flat panel backlighting, a street lighting, vehicle headlamps, museum illumination and residential illumination.[9-11] The great scientists, Nakamura, Akasaki and Amano have been awarded to The Nobel Prize in Physics 2014 for honoring their significant invention of the blue LEDs.

Figure 1.1 presents excitation and emission spectra of conventional phosphors for fluorescent lamps and white-LEDs. The phosphors for fluorescent lamps require an efficient optical absorption of ultra-violet (UV) light region at 254 nm due to an resonance line of mercury.[12] On the other hand, the phosphors for white-LEDs require an efficient optical absorption of violet or blue light region from the emission of LED chip,[13] which is a most important and different characters of phosphors for white-LED compared to that for conventional fluorescent application. In addition, the luminescence due to 4f-4f spin forbidden transitions of Eu^{3+} and Tb^{3+} are used for almost phosphors for fluorescent lamps as a luminescent center.[14] These trivalent lanthanide ions have high emission efficiency under the UV light region at 254 nm, but those emission efficiency under the violet and blue light excitation are

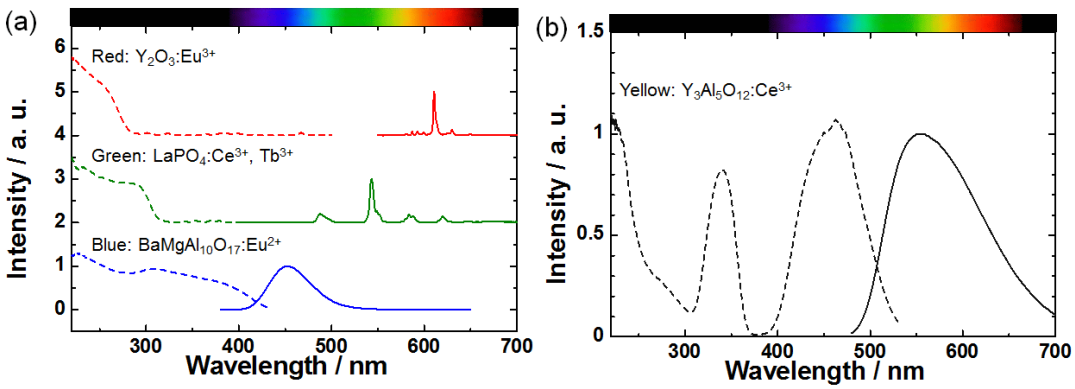

Fig. 1.1 Excitation (dotted lines) and emission (solid lines) spectra of the conventional phosphors for (a) fluorescent lamps and (b) white-LEDs.

significantly quite low because of weak absorption at those excitation region. Therefore, Eu^{2+} and Ce^{3+} ions, which are due to 4f-5d spin allowed transitions, are used in the general white-LED.[15]

White light of a general white-LED is obtained by combining the InGaN based blue LED and a yellow-emitting phosphor, such as a Ce^{3+}-activated yttrium aluminum oxide with a garnet structure (YAG:Ce).[15,16] The emission spectrum of the commercial white-LED is shown in Fig. 1.2. The emission spectrum is composed of the blue emission peaked at 450-460 nm from blue LED and the broad yellow emission peaked at 555 nm from yellow phosphor (YAG:Ce). However, the general white LED has a low color rendering index (CRI) owing to a lack of a red spectral region, as see Fig. 1.2.[13,17]

In order to enhance the CRI, other type of white-LEDs, which consist of blue LED and green- (or yellow-) and red-emitting phosphors, or violet LED and blue-, green- and red-emitting phosphors, have been proposed in recent year.[15,18,19] Thus, it is required to develop the phosphors with various emission colors for improved white-

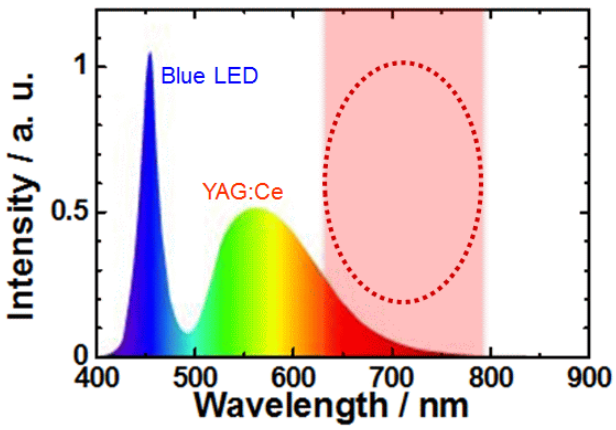

Fig. 1.2 Emission spectrum of the general white-LED, which is composed of InGaN based blue LED and YAG:Ce phosphor.

LEDs, in which the red emitting phosphors are particularly important for solving above problem.

Most oxides are suitable for the commercial materials because of the higher chemical and physical stability, easily synthesis and lower toxicity, compared to nitrides and fluorides.[17] However, the blue-light excitable red-emitting phosphors with the Eu^{2+} and Ce^{3+} are extremely unusual in oxide host materials. Although this can be often explained that a covalency of oxides is generally lower than that of nitrides and sulfides, the red emitting materials are not more in such non-oxide hosts with stronger covalency, as listed in Table 1.1. Therefore, the precise cause of the red emission is as yet not well-known.

Empirical equation to estimate the emission band position of Ce^{3+} and Eu^{2+} have been proposed by van Uitert;[31]

$$E = Q\left[1 - \left(\frac{V}{4}\right)^{1/V} 10^{-(n\,ea\,r)/80}\right] \qquad \text{Eq. 1.1}$$

where, E is the position in the energy of the 5d band edge for the Ce^{3+} and Eu^{2+} ion, Q is the energy position of the lowest 5d band edge for the free ion (50,000 cm^{-1} for Ce^{3+}, 34,000 cm^{-1} for Eu^{2+}), V is the valence state of the activators, n represents the number of anions in the immediate shell about the activator, ea is the electron affinity of the anion atoms dependent on the anion complex type, and r is the ionic

Table 1.1 Typical red-emitting phosphors for white-LED.

Composition	λex (nm)	λem (nm)	Ref.
$LiSrBO_3:Eu^{2+}$	460	618	20
$NaMgPO_4:Eu^{2+}$	450	628	21
α'_L-$Ca_2SiO_4:Eu^{2+}$	450	653	22
$M_4(PO_4)_2O:Eu^{2+}$	~465	~680	23,24,25
$CaAlSiN_3:Eu^{2+}$	460	660	26
$Sr_2Si_5N_8:Eu^{2+}$	450	620	27
$Sr[LiAl_3N_4]:Eu^{2+}$	440	654	28,29
$(Ca,Sr)S:Eu^{2+}$	460	~647	30

M = Ca and Sr

radius of the host cation replaced by activators. Although this formula is actually useful for the estimation of activator doping site from emission spectrum, the results of the calculation using the Eq. 1.1 often give the large errors, and cannot be used in some cases.[32] The Eq. 1.1 considers to the coordination number of the Ce^{3+} and Eu^{2+}, whereas its geometrical shape is not considered yet.

In this thesis, the relationship between the geometrical shape of Ce^{3+} and Eu^{2+} coordination, particularly high symmetry coordination, and luminescence properties via synthesis of some novel oxide phosphors with Ce^{3+} (Eu^{2+}) as an activator. This work is composed of eight chapters as follows;

In chapter 2, novel reddish yellow- and red-emitting $M_3(Sc,Ce)_4O_9$ (M = Ba and Sr) phosphors were synthesized by a conventional solid state reaction method. The crystal structure of the $M_3(Sc,Ce)_4O_9$ were refined by Rietveld method using powder XRD patterns. The luminescence properties of $M_3(Sc,Ce)_4O_9$ were measured, and also the effect of replacing the Ba^{2+} to Sr^{2+} were discussed.

In chapter 3, novel Ce^{3+}-activated phosphors based on $LiSr_2YO_4$ were synthesized by a conventional solid-state reaction method. The $LiSrYO_4$:Ce phosphor can be efficiently excited by blue light irradiation and exhibit extremely broad emission bands, which can cover all visible light region (blue to red emission), with peaks at 520 and 620 nm due to 5d → 4f transition of Ce^{3+}. The broad emission due to two type luminescent mechanisms were discussed as individual emission bands.

In chapter 4, a novel Ce^{3+}-activated borate phosphor, $(Y,Ce)_{17.33}B_8O_{38}$ was discovered. $(Y,Ce)_{17.33}B_8O_{38}$ phosphor exhibits a blue emission peaked at 430 nm under UV light irradiation at 360 nm, and the red emission peaking at 620 nm was also observed under the blue light excitation at 430 nm. In order to enhance the

luminescence intensity of red emission, heterogeneous lanthanide ions, such as La^{3+}, Gd^{3+} and Lu^{3+}, were incorporated in the $(Y,Ce)_{17.33}B_8O_{38}$ lattice. The doping effects on the luminescent properties of heterogeneous lanthanide ions were discussed.

In chapter 5, novel reddish-yellow emitting $BaCa_2Y_6O_{12}:Ce^{3+}$ phosphors were discovered by a melt synthesis technique using an arc imaging furnace, and the crystal structure was analyzed by Rietveld refinement using powder X-ray diffraction. The emission spectra was consisting of the Gaussian bands due to the Ce^{3+} in two different crystallographic site of YO_6 octahedra with $\lambda_{em.}$ = 608 and 680 nm and CaO_6 trigonal prism with $\lambda_{em.}$ = 608 and 680 nm.

In chapter 6, a novel red-emitting olivine-type $NaMgPO_4:Eu^{2+}$ phosphor was synthesized for the first time by the melt synthesis technique using arc-imaging furnace. The crystal structure of $NaMgPO_4:Eu^{2+}$ phosphor was analyzed by Rietveld refinement using a powder XRD pattern for the first time. The crystal structure is newly crystal phase as a $NaMgPO_4$, and the deference between structure and luminescence properties were discussed.

In chapter 7, blue-emitting $(K,Na)Mg_4(PO_4)_3:Eu^{2+}$ phosphors having lower symmetric coordination were synthesized and the luminescent properties were revealed. The K^+ substitution into the Na^+ including lattice gave a strong impact on the luminescence properties.

In chapter 8, the relationship of the geometrical symmetry of Ce^{3+} and Eu^{2+} coordination and luminescent properties were summarized.

The contents of this thesis are composed of the following papers;

1. T. Hasegawa, S.W. Kim, T. Ishigaki, K. Uematsu, H. Takaba, K. Toda, and M. Sato, Novel Reddish Yellow-emitting Ce^{3+}-Doped $Ba_3Sc_4O_9$ Phosphors for Blue-light-based White LEDs, *Chem. Lett.*, 43, 828-830, 2014.

2. S.W. Kim, T. Hasegawa, T. Ishigaki, K. Uematsu, K. Toda, and M. Sato, Efficient Red Emission of Blue-Light Excitable New Structure Type $NaMgPO_4:Eu^{2+}$ Phosphor, *ECS Solid State Letters*, 2, R49-R51, 2013.

3. S.W. Kim, T. Hasegawa, T. Ishigaki, K. Uematsu, M. Sato, and K. Toda, Synthesis of blue-emitting $(K_{1-x}Na_x)Mg_4(PO_4)_3:Eu^{2+}$ phosphors, *J. Info. Disp.*, 15, 53-57, 2014.

In addition, the following are cited as a related papers.

1. S.W. Kim, T. Hasegawa, S. Hasegawa, R. Yamanashi, H. Nakagawa, K. Toda, T. Ishigaki, K. Uematsu and M. Sato, Improved Synthesis of $SrLiAl_3N_4:Eu^{2+}$ Phosphor using Complex Nitride Raw Material, *RSC Adv.*, 6, 61906–61908, 2016.

2. T. Hasegawa, S.W. Kim, S. Kamei, T. Ishigaki, K. Uematsu, K. Ohmi, K. Toda, and M. Sato, Rare-earth Free White-emitting $Ba_2TiP_2O_9$ Phosphor; Revelation of the Crystal Structure and Photoluminescence Properties, *Dalton Trans.*, 45, 11554-11559, 2016.

3. K. Sugimoto, T. Hasegawa, S.W. Kim, K. Uematsu, K. Toda and M. Sato, Novel yellowish white-emitting Eu^{2+}-activated phosphate phosphor based on $Rb_2Ba_3P_4O_{14}$, *J. Ceram. Process. Res.*, 17, 1-4, 2016.

4. T. Hasegawa, S.W. Kim, T. Abe, S. Kumagai, R. Yamanashi, K. Seki, K. Uematsu, K. Toda, and M. Sato, Improvement of Emission Intensity for Near Infrared Emitting $Ca_{14}Zn_6Al_{10}O_{35}:Mn^{4+}$ Phosphor by Oxygen Pressure Method, *Chem. Lett.*, accepted.

5. Y. Imanari, T. Hasegawa, M. Watanabe, K. Toda, T. Ishigaki, S. Kamei, S. W. Kim, K. Uematsu, M. Sato, Suppress of Concentration Quenching by Site Engineering Concept, *Appl. Mech. Mater.*, accepted.

6. S.W. Kim, T. Hasegawa, T. Abe, H. Nakagawa, S. Hasegawa, K. Seki, K. Toda, K. Uematsu, T. Ishigaki, and M. Sato, Abnormal improvement in emission of lanthanum oxysulfide phosphor $La_2O_2S:Tb^{3+}$ synthesized by a novel method,

thermal decomposition in eutectic molten salt, *Ceram. Int.*, 42, 10389-10392, 2016.

7. T. Hasegawa, N. Sato, S.W. Kim, T. Ishigaki, K. Uematsu, K. Toda, and M. Sato, Synthesis and Luminescent Properties of Novel $Ca_3Y_3Ge_2BO_{13}:Ln^{3+}$ (Ln^{3+} = Tb^{3+} and Eu^{3+}) phosphors, *J. Ceram. Soc. Jpn.*, 123, 507-511, 2015.

8. S.W. Kim, T. Hasegawa, M. Inoue, T. Ishigaki, K. Uematsu, K. Toda, and M. Sato, Synthesis of Eu^{2+}-activated Rb-Ba-Sc-Si-O glass phosphors using melt synthesis technique, *J. Ceram. Soc. Jpn*, 122, 452-455, 2014.

9. S.W. Kim, T. Hasegawa, H. Yumoto, T. Ishigaki, K. Uematsu, K. Toda, and M. Sato, Synthesis and photoluminescence properties of Mn^{2+} co-doped white emitting $(Sr,Sn)ZnP_2O_7$ phosphor, *J. Ceram. Process. Res.*, 15, 177-180, 2014.

Chapter 2

Synthesis and Luminescent Properties of Novel Red-Emitting $M_3(Sc,Ce)_4O_9$ (M = Sr and Ba) Phosphors for White-LEDs

2.1 Introduction

As described in general introduction, white-LEDs using yellow phosphor, YAG:Ce have excellent features such as high luminescent efficiency, a long lifetime, good environmental consideration and compactness.[34-36] However, the conventional white-LEDs have a disadvantage such as a low color rendering index (CRI) because YAG:Ce phosphor shows a weak emission intensity in red spectrum region.[37,38] To solve the problem, the white-LEDs combined to blue-LED and two different phosphors, green (or yellow)- and red-emission phosphor, have been proposed.[37,38] As red-emission phosphors, Eu^{3+}-activated oxide phosphors have been actively investigated because these phosphors have a high luminescent intensity with high color purity, and can be simply prepared in air.[39-42] However, the emission intensity of the conventional Eu^{3+}-activated oxide phosphors is insufficient for use in blue LED based white-LEDs, because these phosphors show narrow optical absorption band due to $^7F_0 \rightarrow {}^5D_2$ spin-forbidden transition of Eu^{3+} in blue light region. [43] Consequently, the luminescence intensity of these phosphors are lower than that of yellow- or green-emitting phosphor under the blue-light excitation.[44-46] In addition, the emission bands of Eu^{3+}-activated phosphors have narrow emission band in red spectrum region. The narrow emission band is necessary for a display backlight,[28,47,48] whereas the broad emission band is required to represent a sunlight spectrum for the lighting devices because of obtaining higher *Ra* value. Thus, the

Eu^{3+}-activated phosphors are not suitable as a red component for the white-LEDs lighting devices. In contrast, Eu^{2+}-doped nitride phosphors, $CaAlSiN_3:Eu^{2+}$ and $Sr_2Si_5N_8:Eu^{2+}$, which exhibit a broad red emission under the blue-light irradiation, have been developed as a red-emission phosphor for white-LEDs.[26,49-51] However, these nitride phosphors are hard to synthesize in a single phase form and require a special high-temperature and high-pressure furnace.[26,49-51] Therefore, many investigations have been devoted to search new oxide phosphor materials, which exhibit broad red-emission spectra and high luminescent efficiency under blue-light irradiation.[21-23,52,53]

In order to design a novel phosphor having emission spectra in longer wavelength side including red emission, it is significant to select the crystal structure of the host material. In the series of the activator ions, Eu^{2+} or Ce^{3+} ion are generally used in the phosphor materials for white-LEDs because these ions-doped phosphors present the broad excitation and emission band due to the energy transitions between the 4f ground state and 5d excited state configuration of Eu^{2+} or Ce^{3+}.[21,26,27,37,54,55] In addition, the peak wavelengths in the excitation and emission band of Eu^{2+} or Ce^{3+}-doped phosphors strongly depend on the host crystal structure since the involved 5d orbital is not shielded by outer orbital electrons.[56,57] The energy gap between the 4f ground state and the 5d excited state decreases with increasing the crystal field strength around the Eu^{2+} or Ce^{3+} in the host material because the lowest level of the 5d configuration decreases due to crystal field splitting of the 5d excited level.[58] Therefore, the energy for the electron transfer between the 4f ground state and the 5d excited state becomes smaller, as a result, the excitation and emission band wavelengths shift to longer wavelength side.

In this study, we focused on $Ba_3Sc_4O_9$ as a host material for the phosphor to develop a novel Ce^{3+}-doped yellow-emitting phosphor with high luminescence efficiency under blue light excitation. The crystal structure of $Ba_3Sc_4O_9$ is firstly reported by V. I. Spitsyn *et al.* in 1968.[59] $Ba_3Sc_4O_9$ has a rhombohedral structure with the space group *R*3 (No. 146), which is built out of BaO_n (n = 6, 9 and 12) polyhedron and ScO_6 octahedron, and a part of the Sc^{3+} sites in the $Ba_3Sc_4O_9$ lattice is substituted with Ce^{3+}. Figure 2.1 shows the crystal structure of $Ba_3Sc_4O_9$, which is illustrated using the VESTA program.[60] In the crystal structure, ScO_6 coordination octahedron is a slightly distorted octagonal bipyramid and the distance between Sc^{3+} and nearest O^{2-} is 0.1739 nm, which is shorter than that of the Y^{3+}–O^{2-} in $Y_3Al_5O_{12}$ (0.2397 nm). This indicates that the crystal field strength around the Ce^{3+} in the $Ba_3(Sc_{1-x}Ce_x)_4O_9$ phosphor is stronger than that of the YAG:Ce phosphor; therefore, the phosphors based on $Ba_3Sc_4O_9$ are expected to obtain the excitation and emission bands to longer wavelengths than that of the YAG:Ce phosphor.

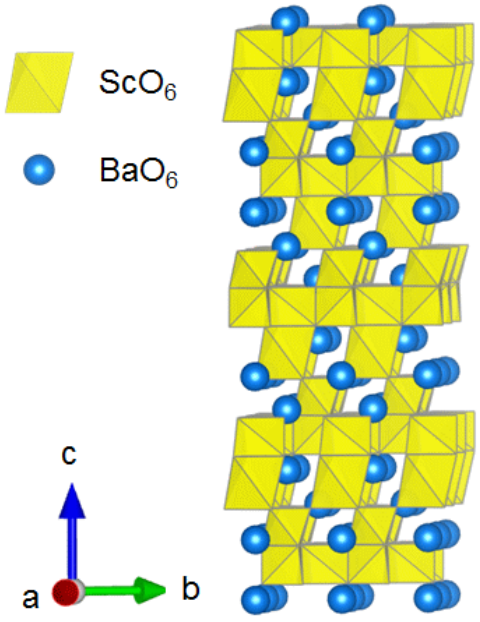

Fig. 2.1 Crystal structure of rhombohedral $Ba_3Sc_4O_9$.

Furthermore, the overall lattice contraction is expected by the replacing the Ba^{2+} ions (ionic radius: 0.147 nm for 9-coordination and 0.161 nm for 12-coordination)[61] in the host $Ba_3Sc_4O_9$ lattice to a smaller Sr^{2+} ion (ionic radius: 0.131 nm for 9-coordination and 0.144 nm for 12-coordination)[61] which results in the decrease between Sc^{3+}-O^{2-} bond distance. Small ion doping is carried out to shift the emission band to longer wavelength side owing to increasing the crystal field strength around Ce^{3+} in the host lattice. The chemical composition of $Sr_3Sc_4O_9$ already suggested from the reports of the SrO-Sc_2O_3 binary phase diagram,[62] but there is no description on the crystal structure, chemical and physical properties.

In this chapter, novel $M_3(Sc_{1-x}Ce_x)_4O_9$ (M = Sr and Ba) phosphors were synthesized in first time, and their precise crystal structure of the $Sr_3Sc_4O_9$ was determined by Rietveld refinement analysis from X-ray diffraction of the synthesized powder sample and their luminescence properties, such as an emission and excitation spectra, quantum efficiency and thermal properties, were investigated in the detail.

2.2 Experimental section

Synthesis of materials. Novel $M_3(Sc_{1-x}Ce_x)_4O_9$ (M = Sr and Ba) phosphors were synthesized by a conventional solid-state reaction method. $BaCO_3$ (purity 99.9%; Kanto Chemical, Co., Inc.), $SrCO_3$ (purity 99.9%; Kanto Chemical, Co., Inc.), Sc_2O_3 (purity 99.99%; Shin-Etsu Chemical, Co., Ltd.) and CeO_2 (purity 99.99%; Kanto Chemical, Co., Inc.) were mixed in a stoichiometric ratio using a mortar with acetone for obtaining a homogeneous chemical mixture, and then the homogeneous mixture was calcined at 1500 °C for 12 h in air. After these calcinations, the samples were reground in a mortar and heated again at 1300 °C for 6 h in a flow of 5%H_2-95%N_2 gas for the reduction of Ce^{4+} to Ce^{3+}.

Materials characterization. The samples were characterized by X-ray powder diffraction (XRD; Mac Science Ltd. MX-Labo), and the crystal structure analysis was carried out by the Rietveld refinement of powder XRD data using the program RIETAN-FP.[63] The emission (PL) and excitation (PLE) spectra were measured at room temperature using a spectrofluorometer (Jasco Corp. FP-6500/6600).

2.3 Result and discussion

Reddish-yellow emitting $Ba_3(Sc_{1-x}Ce_x)_4O_9$ phosphors. The XRD patterns of the $Ba_3(Sc_{1-x}Ce_x)_4O_9$ ($0 \le x \le 0.01$) phosphors are shown in Fig. 2.2. The standard XRD pattern of $Ba_3Sc_4O_9$ from the CIF (Crystal Information File) of inorganic crystal structure database (ICSD #20621) is also shown in Fig. 2.2 as a reference. The diffraction patterns were in good agreement with that of a single phase of the $Ba_3Sc_4O_9$ structure of high crystallinity, and diffraction peak evidence of impurities corresponding to the starting materials was not observed in the patterns. A peak shift to a lower diffraction angle was observed with an increase in the Ce^{3+} content in the host $Ba_3Sc_4O_9$ lattice, and thereby the lattice volume of the $Ba_3(Sc_{1-x}Ce_x)_4O_9$ phosphors linearly increased with increasing Ce^{3+} concentration in the host $Ba_3Sc_4O_9$ lattice as shown in the Fig. 2.3. These results indicate that Ce^{3+} successfully substituted for the Sc^{3+} sites in the host lattice to form solid solutions, because the ionic radius of Ce^{3+} (0.101 nm for 6 coordination)[61] is larger than that of Sc^{3+} (0.0745

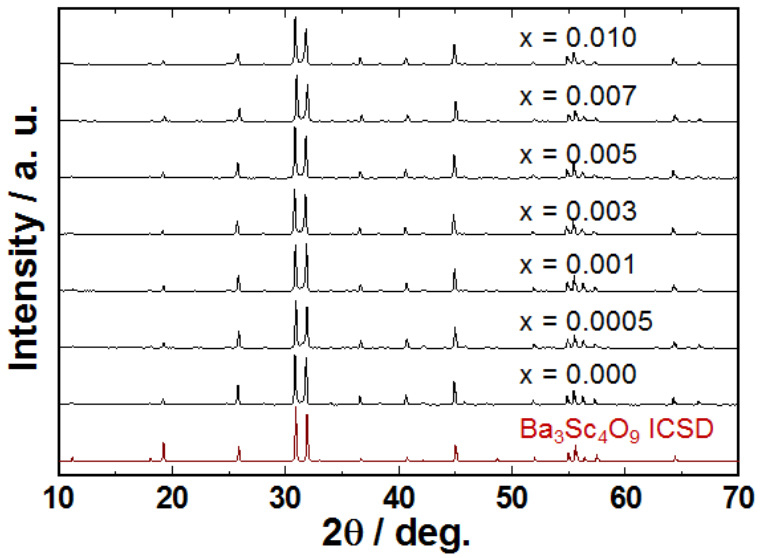

Fig. 2.2 Powder XRD patterns of the $Ba_3(Sc_{1-x}Ce_x)_4O_9$ ($0 \le x \le 0.01$) phosphors.

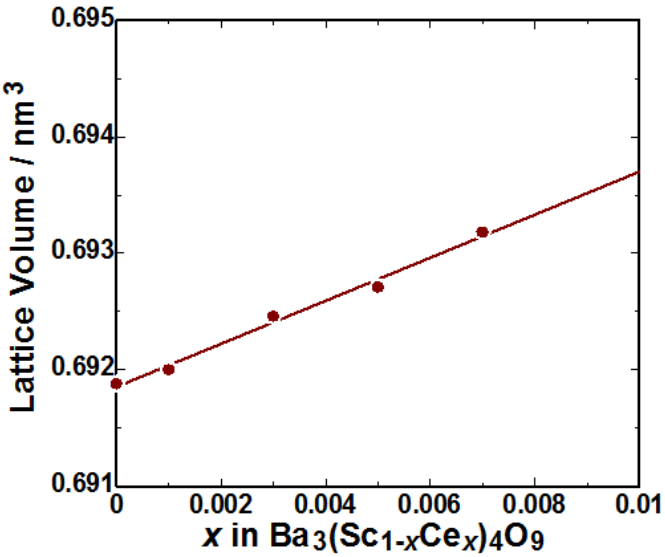

Fig. 2.3 The lattice volume dependence on the Ce^{3+} concentration in the $Ba_3(Sc_{1-x}Ce_x)_4O_9$ ($0 \le x \le 0.01$) phosphors.

for 6 coordination)[61], while it is much smaller than that of Ba^{2+} (0.135 nm for 6 coordination).[61]

Figure 2.4 shows the excitation and emission spectra of a $Ba_3(Sc_{0.999}Ce_{0.001})_4O_9$ phosphor. The excitation spectrum of the $Ba_3(Sc_{0.999}Ce_{0.001})_4O_9$ phosphor obtained in the present study is consisted of a strong broad band covering the region from violet to visible light part, which indicates that the phosphor can be excited by violet and blue light. The emission spectrum exhibits the broad reddish yellow emission band from 480 to 750 nm with the highest intensity at 583 nm, which can be ascribed to the $5d^1 \rightarrow 4f^7$ allowed transition of Ce^{3+} ions,[43,56] under excitation at 437 nm. In addition, the peak position of the Ce^{3+} $5d^1 \rightarrow 4f^7$ allowed transition depends on the crystal field,[58] which is affected by the bond length between Ce^{3+} and nearest O^{2-}. As mentioned above, since the bond length between Sc^{3+} and nearest O^{2-} (0.1739 nm) in $Ba_3Sc_4O_9$ lattice is shorter than that of Y^{3+}–O^{2-} (0.2397 nm) in $Y_3Al_5O_{12}$, the crystal field strength of O^{2-} around Ce^{3+} in the $Ba_3Sc_4O_9$:Ce phosphor is

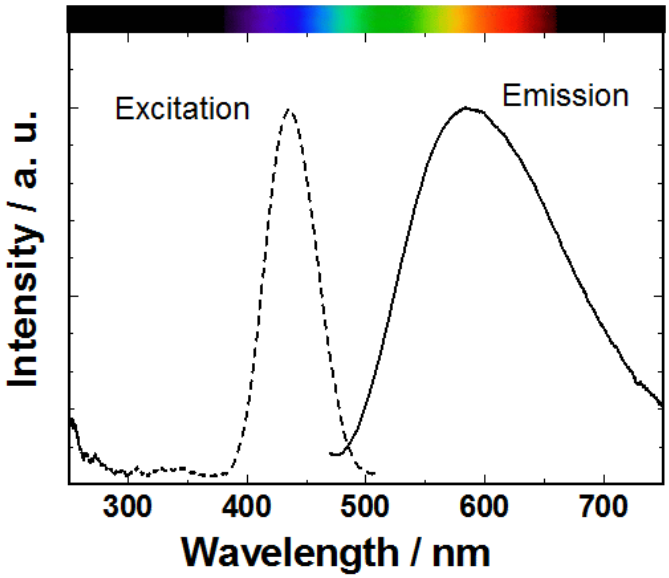

Fig. 2.4 Excitation (broken line) and emission (solid line) spectra of $Ba_3(Sc_{0.999}Ce_{0.001})_4O_9$ phosphor.

stronger than that of the YAG:Ce phosphor. Therefore, the emission peak wavelength of the $Ba_3Sc_4O_9$:Ce phosphor observed in longer wavelength than that of a commercial yellow-emitting YAG:Ce phosphor, which shows the highest wavelength at 555 nm in emission spectrum. Furthermore, the $Ba_3Sc_4O_9$:Ce phosphor shows the stronger emission intensity in red spectral region. These results indicate that the $Ba_3Sc_4O_9$:Ce phosphors are expected to find application as yellow emitting phosphor for blue LED based white-LEDs.

Figure 2.5 shows the dependence of the emission intensities on the Ce^{3+} concentration in the $Ba_3(Sc_{1-x}Ce_x)_4O_9$ ($0.0005 \leq x \leq 0.01$) phosphors. The luminescence emission intensity increased with the amount of Ce^{3+} and reaches a maximum at $x = 0.001$ in the $Ba_3(Sc_{1-x}Ce_x)_4O_9$ ($0.0005 \leq x \leq 0.01$) phosphors. However, the emission intensity tends to decrease with increase with increasing Ce^{3+} content beyond the optimum concentration due to the concentration quenching.

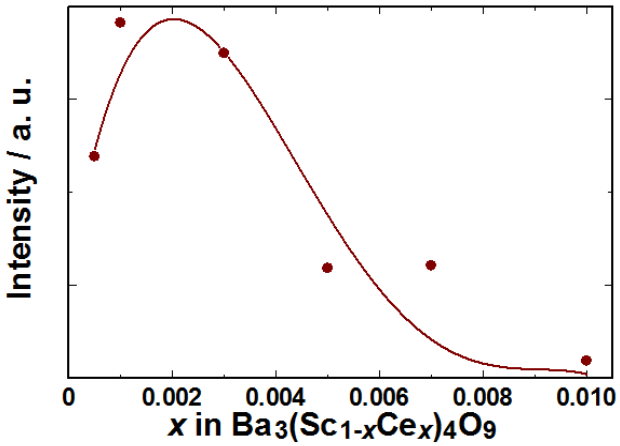

Fig. 2.5 Dependence of the emission peak intensity on the Ce^{3+} concentration in the $Ba_3(Sc_{1-x}Ce_x)_4O_9$ ($0.0005 \leq x \leq 0.01$) phosphors.

It is necessary to consider the thermal quenching behavior in order to apply the high power white-LEDs.[64] Temperature dependence of the emission intensity for the $Ba_3(Sc_{0.999}Ce_{0.001})_4O_9$ phosphor is showed in Fig. 2.6. At 150°C, the emission intensity of the $Ba_3(Sc_{0.999}Ce_{0.001})_4O_9$ phosphor was reduced to 5.6% compared to that at room temperature. The thermal stability of $Ba_3(Sc_{0.999}Ce_{0.001})_4O_9$ phosphor cannot be comparable to that of YAG:Ce (P-46) phosphor.

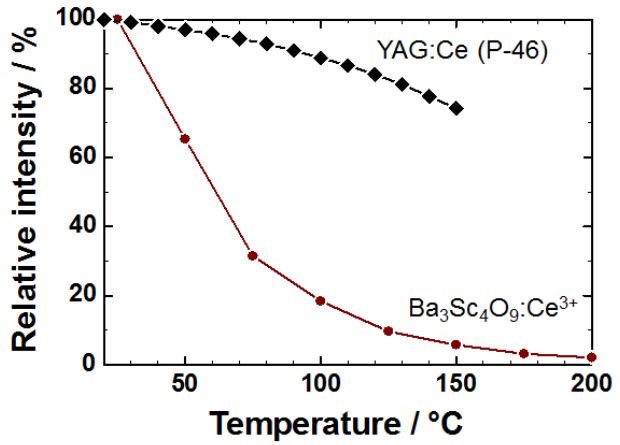

Fig. 2.6 Temperature dependence of the emission peak intensity in the $Ba_3(Sc_{0.999}Ce_{0.001})_4O_9$ phosphor.

Red emitting $Sr_3(Sc_{1-x}Ce_x)_4O_9$ phosphors. Generally, the excitation and emission band wavelength of the Ce^{3+}-doped phosphors strongly depend on the crystal structure of the host materials.[58] Therefore, the investigation of the crystallographic for host materials is significantly important for understanding the luminescence properties of the Ce^{3+}-doped phosphors. However, the XRD pattern and the crystal structure of $Sr_3Sc_4O_9$ host material have not been investigated until now, i.e., the reports of the SrO-Sc_2O_3 binary phase diagram that has not been also investigated the crystal structure of $Sr_3Sc_4O_9$ in the detail. In order to determine the crystal structure of the $Sr_3Sc_4O_9$ host material, the lattice parameters were refined by Rietveld analysis method for the diffraction peaks with the 2θ range from 5 to 90° of the XRD pattern, in which $Ba_3Lu_4O_9$ structure data from the inorganic crystal structure data (ICSD #38383) used as a starting structural model. The result of the Rietveld refinement is shown in Fig. 2.7, and the final crystal lattice and

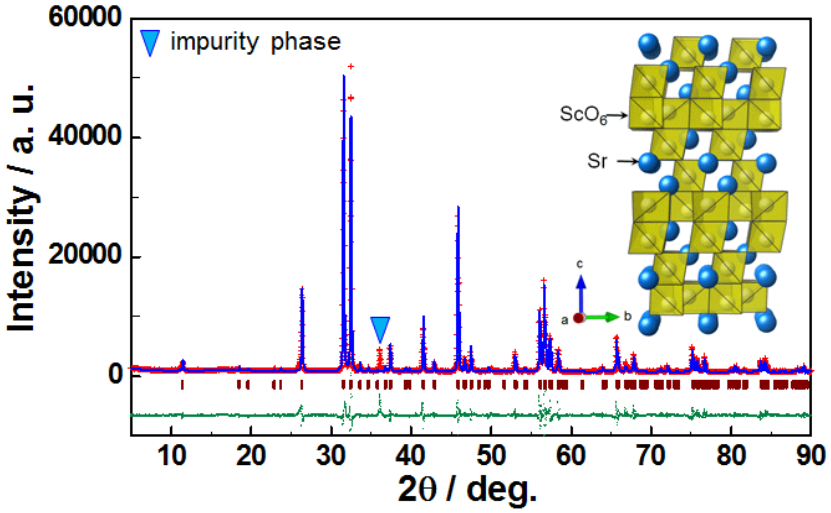

Fig. 2.7 Observed (red cross) and calculated (blue line) X-ray powder diffraction data of $Sr_3Sc_4O_9$ host crystal prepared in this study as well as the difference profile (bottom green line) between them. Bragg reflection peak positions are shown as vertical bars. (Inset) The proto-type crystal structure model of the $Sr_3Sc_4O_9$ host material obtained from Rietveld refinement.

crystallographic parameters and refinement data are summarized in Table 2.1 and 2.2, respectively. The XRD patterns of the $Sr_3Sc_4O_9$ host material mainly consisted of the diffraction peaks due to the refined Bragg position of rhombohedral $Sr_3Sc_4O_9$, whereas, the unknown impurity peak with weak intensity was included at $2\theta = 36.1°$. This impurity peak leads to the decline of the reliability of *R*-factors and *S* value. The final lattice parameters were a = 0.56792(1) nm, c = 2.33534(5) nm and V = 0.65231(3) nm^3 of a rhombohedral system with the space group of *R*3 (No. 146), which has three general position sites (anion sites; 9b Wyckoff position) and seven

Table 2.1 The lattice parameters and the R-factors of $Sr_3Sc_4O_9$ obtained from Rietveld refinement of XRD data.

Lattice parameters	
Crystal System	rhombohedral
Space group	*R*3 (No. 146)
a (nm)	0.56835(1)
c (nm)	2.33693(4)
V (nm^3)	0.65374(2)
R-factors	
R_{wp}	14.820%
R_p	10.025%
S	5.524
R_B	8.659%
R_F	5.139%

Table 2.2 The atomic parameters of the $Sr_3Sc_4O_9$ obtained from Rietveld refinement using powder XRD pattern.

$Sr_3Sc_4O_9$						
Atom	Site	Occ.	x	y	z	B_{eq} (nm^2)
Sr1	3a	1.0	0	0	0	0.03139
Sr2	3a	1.0	0	0	0.1640(6)	-0.00326
Sr3	3a	1.0	0	0	0.5781(9)	0.0116
Sc1	3a	1.0	0	0	0.427(1)	0.004(6)
Sc2	3a	1.0	0	0	0.863(2)	0.006(5)
Sc3	3a	1.0	0	0	0.7366(9)	-0.017(4)
Sc4	3a	1.0	0	0	0.300(2)	0.015(8)
O1	9b	1.0	0.910(9)	0.68(1)	0.254(5)	0.04(1)
O2	9b	1.0	0.980(6)	0.547(8)	0.142(2)	-0.018(9)
O3	9b	1.0	0.008(8)	0.613(9)	0.037(2)	0.05(1)

special position sites (cation sites; 3a Wyckoff position). *R*-factors obtained from Rietveld refinement were R_{wp} = 15.951%, R_p = 10.933%, S = 5.9457, R_B = 8.331%, R_F = 5.689%, respectively (summarized in Table 2.1). From the Table 2.1 and 2.2, these results were not enough good fitting the simulated XRD pattern of $Sr_3Sc_4O_9$ because of low R-factors and S. (R-factors and S) and the minus iso-temperature factors, such as Sr2, Sc3 and O2 sites. This indicates that the refined crystal structure was presented as the proto-type crystal data. Although the precise crystal structure data were not obtained in this study, we can be illustrated prototype crystal structure of $Sr_3Sc_4O_9$ based on the crystallographic data obtained by Rietveld refinement analysis using the VESTA program (Fig. 2.7 (inset) and Fig. 2.8).[60] As shown in Fig. 2.8 (a), the ScO_6 octahedra are to form the rigid three-dimensional framework owing to a corner-, edge- and face-sharing of each other in the crystal structure. In three-dimensional framework, the Sc1 and Sc3 sites were formed two-dimensional layer

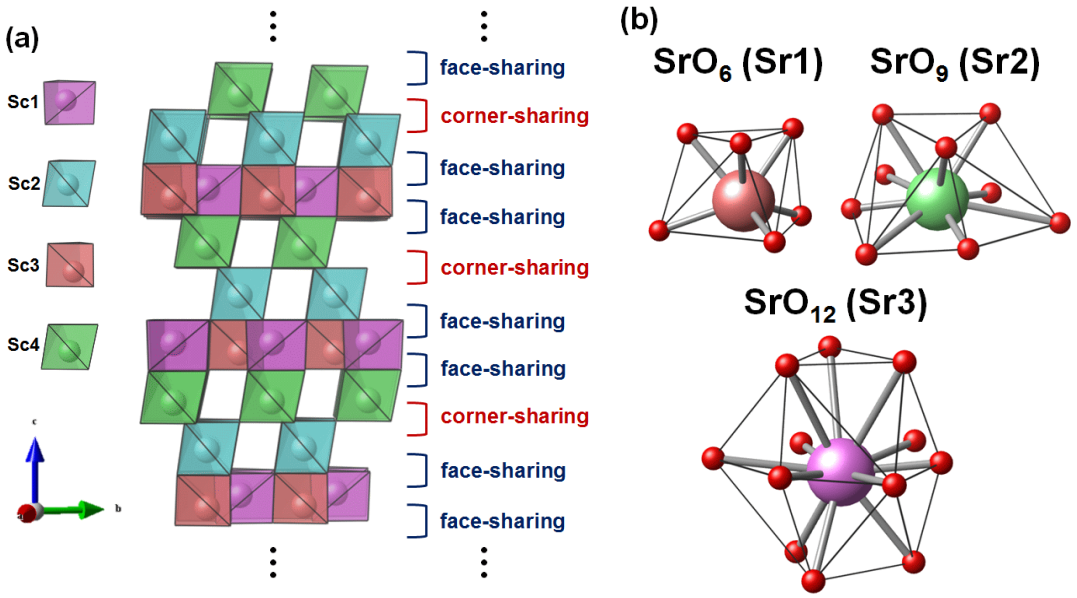

Fig. 2.8 (a) The ScO_6 octahedra framework in $Sr_3Sc_4O_9$. (b) The coordination environment of the SrO_n (n = 6, 9 and 12) in $Sr_3Sc_4O_9$ host material.

along to (00*l*) plane by an edge-sharing with O2-O3 of ScO_6 octahedra. The layers are separated by layers connected ScO_6 each other in direction of the c-axis.

In the stacking of the ScO_6 layers along *c*-axis direction, Sc1 and Sc3 site layers are connected to Sc2 and Sc4 sites layers by O2 and O3 triangle face-sharing, respectively. In addition, Sc2 and Sc4 site layers are connected by the corner-sharing into O1 atoms (see Fig. 2.8 (a)). Sr^{2+} ions are located at the space of the three-dimensional framework and Sr^{2+} ions are coordinated by 6, 9, and 12 oxygen atoms (Fig. 2.8 (b)), SrO_6 (Sr1 site), SrO_9 (Sr2 site), and SrO_{12} (Sr3 site), respectively. The calculated bond valence sum of the three different Sr sites using equation proposed by Brown[65] were 2.3208 (Sr1 site), 1.7718 (Sr2 site) and 1.7787 (Sr3 site), respectively. This result indicates that the coordination numbers of these Sr sites are reliable because the values of the bond valence sum are near to expect the charge value of Sr^{2+}.

Figure 2.9 (a) shows the XRD patterns of the $Sr_3(Sc_{1-x}Ce_x)_4O_9$ ($0 \leq x \leq 0.007$) phosphors. The simulation pattern of $Sr_3Sc_4O_9$ obtained by Rietveld refinement analysis in this study is also shown in Figure 2.9 (a) as a reference. The diffraction peaks corresponding to rhombohedral $Sr_3Sc_4O_9$ structure were observed as a main phase in all sample prepared in this study. In addition, weak impurity peak corresponding to unknown phase is also observed in all samples; however, the peak intensity was not affected by increasing the Ce^{3+} concentration in the $Sr_3(Sc_{1-x}Ce_x)_4O_9$ ($0 \leq x \leq 0.007$) phosphors. This result indicates that the luminescence behavior of the $Sr_3(Sc_{1-x}Ce_x)_4O_9$ ($0 \leq x \leq 0.007$) phosphors with Ce^{3+} concentration is not affected by a small amount of the unknown phase. The diffraction peaks corresponding to the $Sr_3Sc_4O_9$ structure shift to lower diffraction angle side with

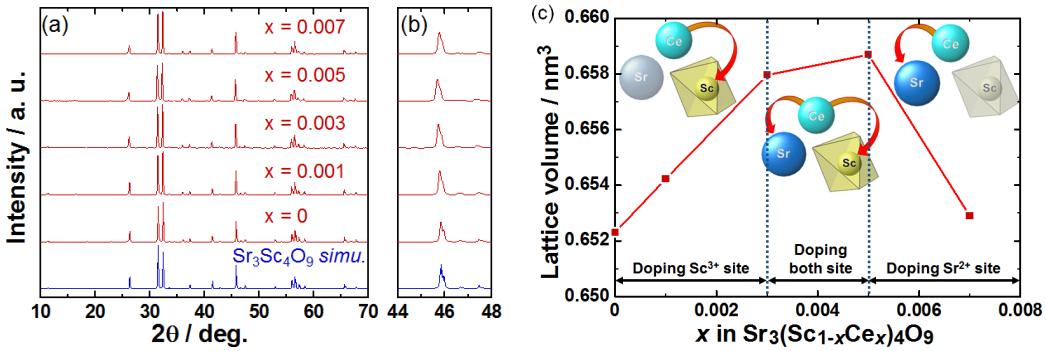

Fig. 2.9 (a) XRD patterns of $Sr_3(Sc_{1-x}Ce_x)_4O_9$ ($0 \le x \le 0.007$) samples, (b) the enlarged view (45-47°) of XRD patterns of $Sr_3(Sc_{1-x}Ce_x)_4O_9$ ($0 \le x \le 0.007$) samples. (c) Dependence of the lattice volume on the Ce^{3+} concentration in the $Sr_3(Sc_{1-x}Ce_x)_4O_9$ ($0 \le x \le 0.007$) samples.

increasing the Ce^{3+} content in the host $Sr_3Sc_4O_9$ lattice for the samples with $x \le 0.005$ (Fig. 2.9 (b)). The lattice volume of the rhombohedral $Sr_3Sc_4O_9$ phase in the samples with $x \le 0.003$ increases monotonously with the increase in the Ce^{3+} content as shown in Fig. 2.9 (c). These results indicate that Ce^{3+} successfully substituted into the Sc^{3+} site in the host $Sr_3Sc_4O_9$ lattice, because ionic radius of Ce^{3+} is larger than that of the Sc^{3+} and it is smaller than that of the Sr^{2+} ion. Although the lattice volume of the sample with x = 0.005 is larger compared to the sample with x = 0.003, the increase range of lattice volume is small. In addition, the lattice volume of the sample with x = 0.007 is became smaller than of the sample with x = 0.003. This indicated that the Ce^{3+} ion begin to occupy the larger Sr^{2+} site in the host $Sr_3Sc_4O_9$ lattice as the Ce^{3+} concentration increased beyond the solid solubility limit (x = 0.003) in replacement of the Sc^{3+} site. On the other hand, in the case of the $Ba_3(Sc_{1-x}Ce_x)_4O_9$ phosphors, the lattice volume monotonously increases with increasing the Ce^{3+} concentration at the more than x = 0.003. The deference of the lattice volume dependence on the Ce^{3+} content can be explained that the Ce^{3+} ion in $Ba_3(Sc_{1-x}Ce_x)_4O_9$

phosphor is substituted in the only Sc ion on the higher Ce^{3+} concentration than $x > 0.003$.

Figure 2.10 shows the excitation and emission spectra of the $Sr_3(Sc_{0.997}Ce_{0.003})_4O_9$ phosphor. Results for the conventional $Ba_3(Sc_{0.999}Ce_{0.001})_4O_9$ phosphor are also plotted in the Fig. 2.10 for comparison. The excitation spectrum of the $Sr_3(Sc_{0.997}Ce_{0.003})_4O_9$ phosphor consisted of a strong optical absorption band from 380 to 500 nm due to 4f-5d transition of Ce^{3+},[43] which is good matched to emission of InGaN-based blue LED chips. The emission spectrum of the $Sr_3(Sc_{0.997}Ce_{0.003})_4O_9$ phosphor exhibited a broad red emission band from 480 to 800 nm with a peak at 620 nm, which is corresponding to 5d–4f transition of Ce^{3+},[43] under excitation wavelength at 425 nm. Ce^{3+}-doped red-emitting sulfide phosphors have been recently investigated by Chen[66] and Kakihana,[67] however, Ce^{3+}-doped red-emitting oxide phosphors have not been reported. The emission peak wavelength of

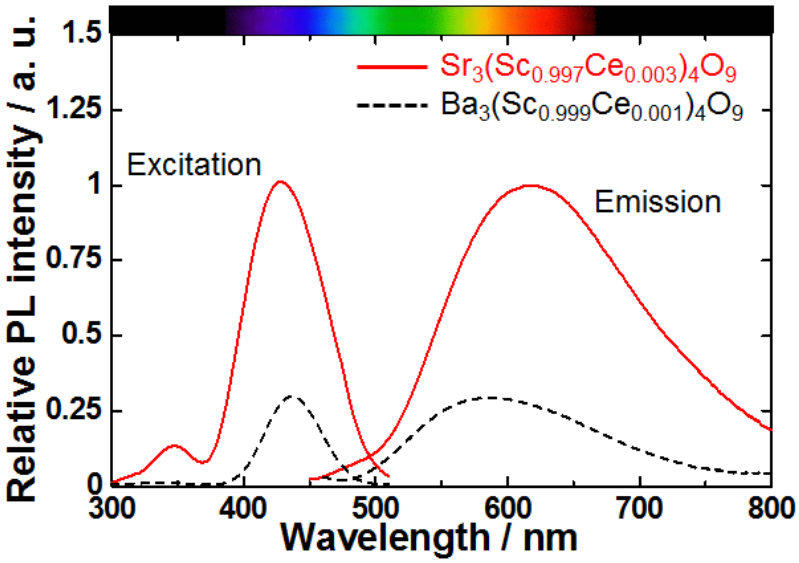

Fig. 2.10 Excitation and emission spectra of the $Sr_3(Sc_{0.997}Ce_{0.003})_4O_9$ (solid line) and $Ba_3(Sc_{0.999}Ce_{0.001})_4O_9$ (dotted line) phosphors. The excitation and emission spectra were recorded at maximum peak wavelength for each samples.

the Ce^{3+}-doped $Sr_3Sc_4O_9$ phosphor effectively shifted to the longer wavelength side (approximately 37 nm) compared to the Ce^{3+}-doped $Ba_3Sc_4O_9$ phosphor (583 nm). The emission intensity of $Sr_3(Sc_{0.997}Ce_{0.003})_4O_9$ phosphor was increased to about 3.5 times compared with that of $Ba_3(Sc_{0.999}Ce_{0.001})_4O_9$ phosphor. The internal quantum efficiency of $Sr_3(Sc_{0.997}Ce_{0.003})_4O_9$ phosphor under the excitation wavelength of 425 nm at the room temperature was 53%, which is higher than that of $Ba_3(Sc_{0.999}Ce_{0.001})_4O_9$ phosphor (40%).

Furthermore, to the best of our knowledge, the emission band of the Ce^{3+}-activated $Sr_3Sc_4O_9$ phosphor (620 nm) located at the longest wavelength side in the Ce^{3+}-doped oxide phosphors such as $Y_3Al_5O_{12}:Ce^{3+}$ (550 nm),[16] γ-$Ca_2(Si,Al)O_4:Ce^{3+}$ (575 nm),[68] $Sr_6Y_2Al_4O_{15}:Ce^{3+}$ (600 nm)[52] and $Lu_2CaMg_2(Si,Ge)_3O_{12}:Ce^{3+}$ (600 nm)[53]. It is extremely difficult to obtain the red emission by the 5d-4f transition of Ce^{3+} in the oxides because the free energy level of the Ce^{3+} ion (49340 cm^{-1}) locates at higher than that of Eu^{2+} ion (34000 cm^{-1}).[69,70] As the results, the almost emission bands in the Ce^{3+}-doped oxides generally locate from UV- to blue-light region at ~500 nm. Therefore, it is extremely difficult to obtain the red emission due to Ce^{3+} ion in oxide materials. The full width half maximum (FWHM) of emission band of $Sr_3(Sc_{0.997}Ce_{0.003})_4O_9$ phosphor at room temperature was estimated at 177 nm (4530 cm^{-1}). In comparison to other known red-emitting phosphors, such as $(Sr,Ca)AlSiN_3:Eu^{2+}$ (50 nm; 2100~2500cm^{-1}),[71,72] the FWHM of broad emission band of $Sr_3(Sc_{0.997}Ce_{0.003})_4O_9$ phosphor is unusual. These results support that $Sr_3Sc_4O_9:Ce^{3+}$ phosphors are suitable as a red emission phosphor for development of the white-LEDs lighting system with high CRI.

Figure 2.11 shows the dependence of the emission intensity on the Ce^{3+} concentration in $Sr_3(Sc_{1-x}Ce_x)_4O_9$ ($0.0005 \leq x \leq 0.007$) phosphors. The emission intensity increased with the amount of Ce^{3+} until it reached a maximum at $x = 0.003$ in $Sr_3(Sc_{1-x}Ce_x)_4O_9$, and then decreased probably due to concentration quenching, which occurs via the nonradiative energy transfer among the nearest-neighbor ions.[73,74] The critical transfer distance among the Ce^{3+}-Ce^{3+} nearest-neighbor ions, *Rc* were calculated by a following equation;[75]

$$R_c = 2\left(\frac{3V}{4\pi x_c z}\right)^{1/3} \qquad \text{Eq. 2.1}$$

where, *V* represents the unit cell volume, x_c refers to the critical concentration of Ce^{3+}, and *N* represents the number of total Ce^{3+} doping sites in the unit cell. In the case of the Ce^{3+}-doped $Sr_3Sc_4O_9$ phosphor, using the values $V = 0.65374$ nm^3, $x_c = 0.3\%$ and $N = 12$, R_c was found to be 3.3 nm, which indicates larger value compared to the other Ce^{3+}-doped oxides phosphors, such as 2.6 nm for $Lu_2CaMg_2Si_3O_{12}$:Ce^{3+} and 2.0 nm

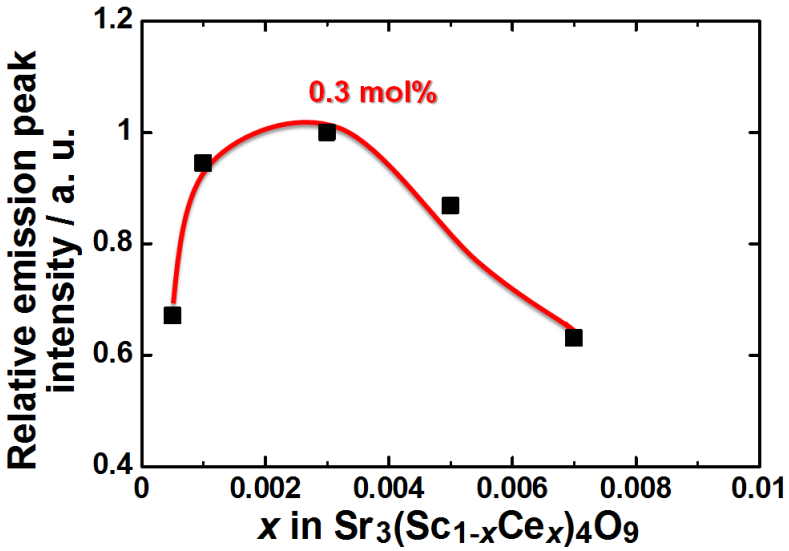

Fig. 2.11 Dependence of the emission intensities on the Ce^{3+} concentrations in the $Sr_3(Sc_{1-x}Ce_x)_4O_9$ ($0.0005 \leq x \leq 0.007$) under the each maximum excitation peak wavelength.

for $CaSc_2O_4:Ce^{3+}$, respectively.[53,76] In the $Sr_3Sc_4O_9$ structure, the Sc atoms each other are very closely because of the face-sharing connection in the structure. Therefore, the inhomogeneous Ce^{3+} ion causes to the large quenching at the low Ce^{3+} concentration in this phosphor.

The understanding of the thermal quenching property on phosphor materials is one of the key application criterion for white-LEDs phosphors because the InGaN blue-LED chip rises the temperature up to 150°C on the operated in a high-power white-LEDs. The temperature dependence of the emission spectra for the $Sr_3(Sc_{0.997}Ce_{0.003})_4O_9$ phosphor under the excitation at 425 nm is shown in Fig. 2.12 (a). It is obvious that the emission band shows a blue-shift, from 620 to 600 nm, with the increase of temperature. The blue-shifts with increasing the temperature are generally observed in the Ce^{3+}-activated phosphors, $(Ca,Li)AlSiN_3:Ce^{3+}$,[77] $(La,Ca)_3Si_6N_{11}:Ce^{3+}$,[78] $(Ca,Na)O:Ce^{3+}$ [79] and *etc*. The blue-shifts are usually explained to be the reduction of crystal field splitting of the Ce^{3+} 5d-orbital owing to the increase of the bond distance of Ce^{3+}–O^{2-} in accordance with the lattice expansion. The reduction of the crystal field splitting of the 5d-orbital results in the increase of the energy gap between the excited 5d level and ground state 4f level of the Ce^{3+}, consequently, emission band shifted to shorter wavelength side (i.e. higher energy side).[80] Fig. 2.12 (b) shows the temperature dependence of the emission peak intensity on $Sr_3(Sc_{0.997}Ce_{0.003})_4O_9$ phosphor under the excitation at 425 nm and that of $Ba_3(Sc_{0.997}Ce_{0.003})_4O_9$ phosphor for comparison. The phosphor showed a steep reduction of the emission peak intensity with increasing the temperature from 25 to 150°C, which can be accounted by the thermal quenching. At 150 °C, the relative emission intensity of the phosphor was 19.1% compared at 25°C. The emission

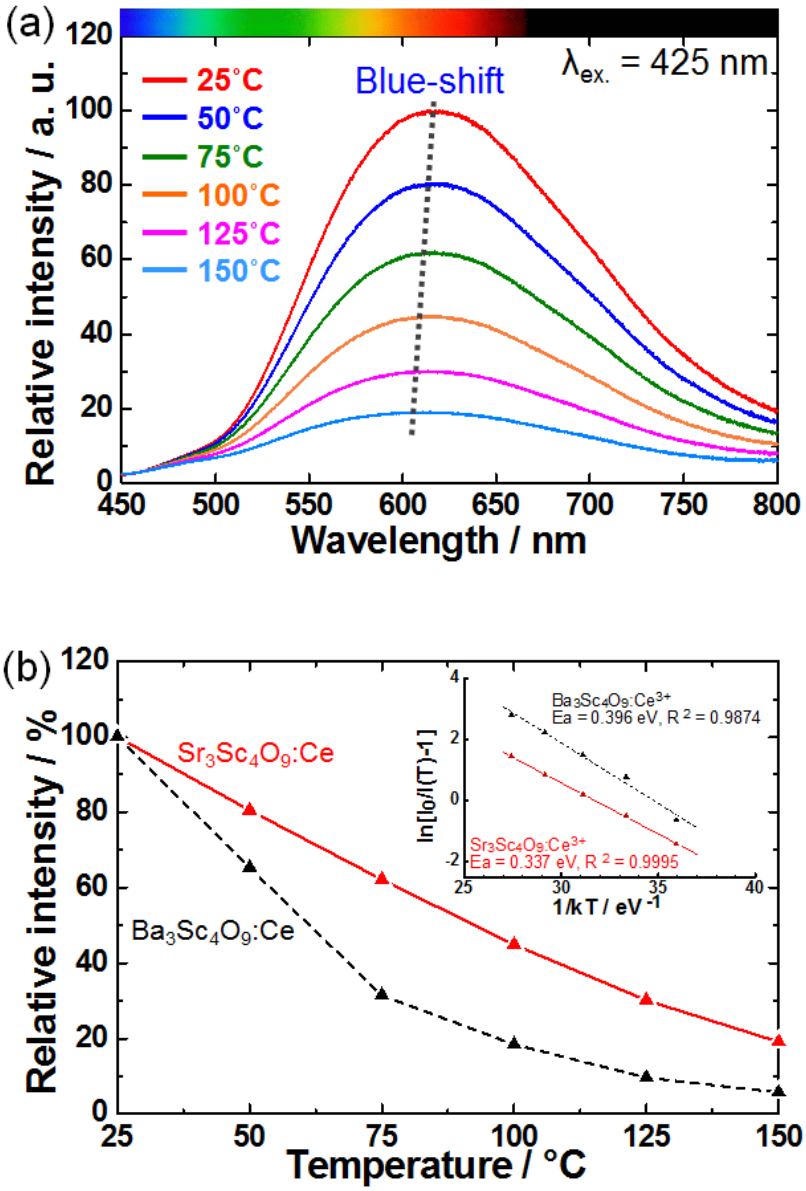

Fig. 2.12 (a) Thermal dependence of the emission spectra and (b) intensity on the Ce^{3+} concentrations in the $Sr_3(Sc_{0.997}Ce_{0.003})_4O_9$ under the blue light excitation at 425 nm. (Inset) The plot of $\ln[I_0/I(T)-1]$ vs. 1/T of the $Sr_3(Sc_{0.997}Ce_{0.003})_4O_9$ phosphors.

intensity of $Sr_3(Sc_{0.997}Ce_{0.003})_4O_9$ at 150°C is higher than that of $Ba_3(Sc_{0.999}Ce_{0.001})_4O_9$ (5.75% at 150°C) which shows highest emission intensity in the $Ba_3(Sc_{1-x}Ce_x)_4O_9$ phosphors.

The thermal stability of emission peak intensity has been usually discussed by an activation energy E_a (eV), which can be calculated by following equation:[81]

$$I(T) = \frac{I_0}{1+c\ exp\left(\frac{-E_a}{kT}\right)} \qquad \text{Eq. 2.2}$$

where I_0 and $I(T)$ are emission intensities of the phosphor at an initial (25°C) and the recording temperatures (~150°C), respectively; c is a constant; k is the Boltzmann's constant (8.617×10^{-5} eV·K^{-1}) and T is the operating temperature. The $\ln[(I_0/I_T)-1]$ vs. $1/k_BT$ plot can be concluded that the activation energy for the $Sr_3(Sc_{0.997}Ce_{0.003})_4O_9$ phosphor and $Ba_3(Sc_{0.999}Ce_{0.001})_4O_9$ is found to be 0.334 and 0.396 eV, respectively (inset of Fig. 2.12 (b)). Thus, the thermal quenching behavior of $Sr_3(Sc_{0.997}Ce_{0.003})_4O_9$ phosphor occurred at the higher temperature compared to those of $Ba_3(Sc_{0.999}Ce_{0.001})_4O_9$ phosphor, which leads to the enhancement of the internal quantum efficiency.

2.4 Summary

Novel Ce^{3+}-activated $M_3Sc_4O_9$ (M = Sr and Ba) phosphors were synthesized by a conventional solid-state reaction method. These structures were built out by the connection of the edge-sharing of ScO_6 polyhedra along to c-axis direction, as well as, the stacking for the corner- and face-sharing of ScO_6 polyhedra along to *c*-axis. The XRD patterns of Ce^{3+}-activated $M_3Sc_4O_9$ (M = Sr and Ba) phosphors were good agreement with the simulation pattern obtained by Rietveld refinement, but it included a small amount of unknown impurity phase in the $Sr_3(Sc_{1-x}Ce_x)_4O_9$ ($0.0005 \leq x \leq 0.007$) phosphors. The $Ba_3(Sc_{0.999}Ce_{0.001})_4O_9$ phosphor was excited efficiently under excitation at 437 nm, and exhibited a broad reddish yellow emission peaking 583 nm including red light region. The result indicates that the $Ba_3(Sc_{0.999}Ce_{0.001})_4O_9$ phosphor is a suitable candidate for the yellow-emitting phosphor of blue LED based white-LEDs lamps as an alternative to commercial YAG:Ce phosphor. On the other hands, the emission band of $Sr_3(Sc_{0.997}Ce_{0.003})_4O_9$ phosphor, which showed highest emission intensity, located in red region peaking at 620 nm with broad band of FWHM = 4530 cm^{-1}. To the best of our knowledge, this phosphor is the first reported material as red-emission phosphor having an emission band at 620 nm among the reported Ce^{3+}-doped oxide phosphors. The result obtained in this study will contribute to provide new avenues for enhancing the CRI of white-LEDs, as well as for developing the novel Ce^{3+}-doped oxide phosphor having longer wavelength emission.

Chapter 3

Unusual Broad Emission Phosphor Using $LiSr_2YO_4$ host with Ce^{3+} as an Activator

3.1 Introduction

Recently, phosphors with a very wide emission spectrum that cover green and red spectrum region have been realized using an energy transfer between Eu^{2+}/Ce^{3+} and Mn^{2+}. These phosphor materials are expected to use white-LED with the high CRI because they can exhibit a tri-color emission by blue-light excitation in the single host. In contrast, the Ce^{3+} ion, which is located at the multiple crystallographic sites in the single host, is expected to show a broad emission spectrum.

In this chapter, we focused on the $LiSr_2YO_4$, as a host material to develop the novel phosphors having high emission intensity in very wide emission spectra including red emission region. The crystal structure of $LiSr_2YO_4$ is shown in Fig. 3.1 (a), which is illustrated using the VESTA program.[60] $LiSr_2YO_4$ has orthorhombic structure with space group of *Pnma* (No. 62), in which LiO_4 tetrahedra and YO_6 octahedra shared the points and edge of each other to form a framework, and SrO_n (n = 6 and 7) polyhedra occupied in space of framework.[83] Since both Sr^{2+} and Y^{3+} ions has a similar ionic radius to that of Ce^{3+} ion, Ce^{3+} can be possible to substitute in the three different sites having different crystallographic environments with SrO_n (n = 6 and 7) polyhedra and YO_6 octahedron. The crystallographic environments of SrO_n (n = 6 and 7) polyhedra and YO_6 octahedron are shown in Fig. 3.1 (b). Among

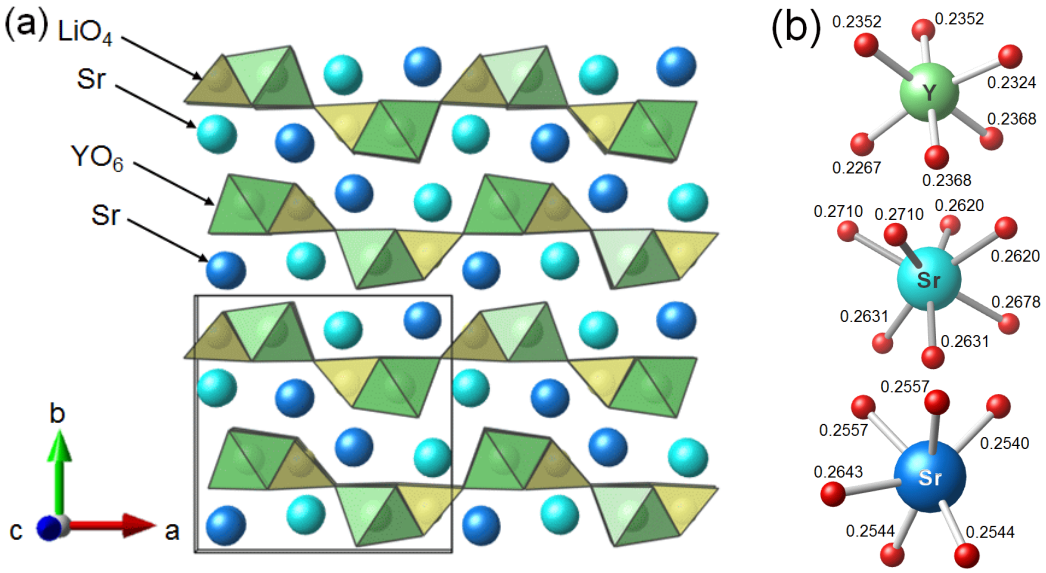

Fig. 3.1 (a) Crystal structure of $LiSr_2YO_4$. (b) Coordination environment of YO_6, SrO_6, and SrO_7 polyhedron in $LiSr_2YO_4$ lattice (the number shows bond distance between a cation and nearest oxygen). The unit is nm.

these different sites, distorted YO_6 octahedral site has shorter average bond distance of Y–O (0.2339 nm) compared with SrO_6 (0.2564 nm) and SrO_7 (0.2657 nm) polyhedral sites. The Y–O average bond distance of the YO_6 octahedral in the $LiSr_2YO_4$ lattice is also shorter than that of the YO_8 in the $Y_3Al_5O_{12}$ (YAG; 0.2372 nm) lattice.[83]

The excitation and emission band positions of the Ce^{3+}-activated phosphors strongly depend on the crystal field strength around Ce^{3+} ions in the host lattice and the crystal field strength increases with decreasing the bond distance between Ce^{3+} and O^{2-}.[55,84] A strong crystal field strength will contribute to shift the excitation and emission band of Ce^{3+}-activated phosphors to longer wavelength side owing to the larger energy splitting of the 5d excited level of Ce^{3+}. When Ce^{3+} substituted in distorted YO_6 octahedral site of $LiSr_2YO_4$, the $LiSr_2YO_4$:Ce^{3+} phosphors are expected to obtain longer wavelength emission compared with YAG:Ce phosphor. In this

chapter, therefore, the $LiSr_2Y_{1-x}O_4:Ce^{3+}_x$ ($0.01 \leq x \leq 0.10$) phosphors were synthesized by a convention solid-state reaction method and their luminescence properties were characterized.

3.2 Experimental section

Synthesis of materials. $LiSr_2Y_{1-x}O_4:Ce^{3+}_x$ ($0.01 \leq x \leq 0.10$) phosphors were synthesized by the conventional solid-state reaction method. Li_2CO_3 (99.99%; Kanto Chemical, Co., Inc.), $SrCO_3$ (99.99%; Kanto Chemical, Co., Inc.), Y_2O_3 (99.99%; Kanto Chemical, Co., Inc.) and CeO_2 (99.99%; Kanto Chemical, Co., Inc.) were used as the raw materials. These starting powders were mixed using an agate mortar with acetone for obtaining a homogeneous chemical mixture. The homogeneous mixture was pressed into 15 mm diameter disk pellets under a pressure of 10 MPa and then the pelletized samples were clacined at 900 °C for 12 h in a flow of 95 vol% Ar-5 vol% H_2 mixed gas. Finally, the samples were reground in a mortar.

Materials characterization. The crystal structure of $LiSr_2Y_{1-x}Ce_xO_4$ ($0.01 \leq x \leq 0.10$) phosphors obtained in this study were characterized by X-ray diffractometor (XRD; Mac Science Ltd. MX-Labo) using CuKα radiation. Photoluminescence (PL) excitation and emission spectra were measured at room temperature using spectrofruorometer (Jasco Corp. FP-6500/6600).

3.3 Results and discussion

The XRD patterns of the $LiSr_2Y_{1-x}Ce_xO_4$ ($0.01 \leq x \leq 0.10$), which is theoretical composition, phosphors are shown in Fig. 3.2. The XRD pattern of $LiEu_3O_4$, which can be presented by the sample formula of LiA_2BO_4 (A = divalence metal ions and B = trivalence rare earth ions),[85,86] from the inorganic crystal structure database (ICSD #15111) is also shown in Fig. 3.2 as a reference. A single phase of orthorhombic $LiSr_2YO_4$ structure was successfully obtained for all samples. A peak shift to lower diffraction angle is observed with increasing the Ce^{3+} concentration in the $LiSr_2Y_{1-x}O_4:Ce^{3+}_x$. This indicates that Ce^{3+} is preferentially occupied in the Y^{3+} site in the $LiSr_2YO_4$ host lattice because ionic radius of Ce^{3+} (0.101 and 0.107 nm for 6 and 7-fold coordinations)[61] is larger than that of Y^{3+} (0.090 nm for 6-fold coordination)[61] while it is smaller than that of Sr^{2+} (0.118 and 0.121 nm for 6 and 7-fold coordinations).[61]

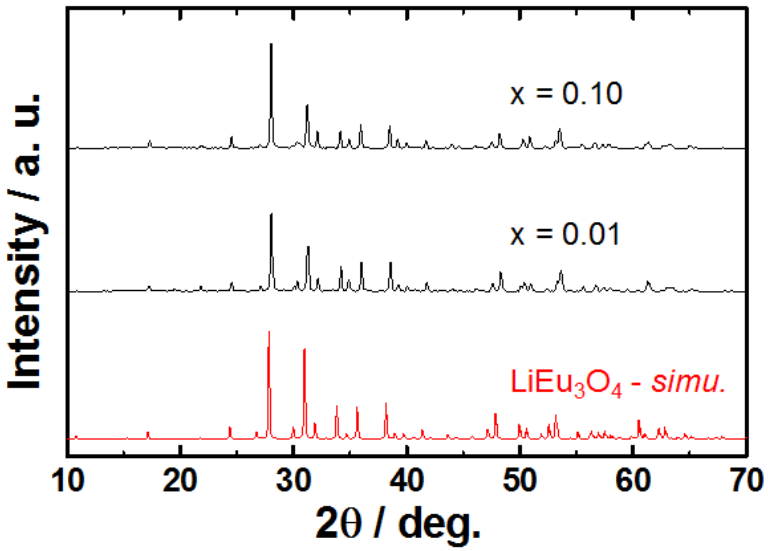

Fig. 3.2 Powder XRD patterns of $LiSr_2Y_{1-x}O_4:Ce^{3+}_x$ phosphors.

Figure 3.3 shows the excitation and emission spectra of the $LiSr_2Y_{0.99}Ce_{0.01}O_4$ phosphor, which showed the highest emission peak intensity in the $LiSr_2Y_{1-x}Ce_xO_4$ phosphors. The excitation spectrum recorded for emission at 620 nm consisted of a strong broad band in blue light region, which means that this phosphor can be suitable for application in white-LEDs excited by blue LED. The excitation band correspond to the 4f → 5d transition of Ce^{3+} ion. These phosphors exhibit an extremely broad emission band due to the $4f^65d^1 \rightarrow 4f^7$ transition of Ce^{3+} under excitation at 445 nm. The full width at half maximum (FWHM) of the emission band of the $LiSr_2Y_{0.99}Ce_{0.01}O_4$ phosphor is approximately 200 nm and it is the broadest compared to the conventional Ce^{3+}-activated phosphors reported in previous studies;[52,87] e.g. the FWHM of the emission band of YAG:Ce phosphor is 100 nm.[16,88] In addition, the emission band of the $LiSr_2Y_{0.99}Ce_{0.01}O_4$ phosphor can be covered the wide visible light region from blue light to deep red light region, especially it shows

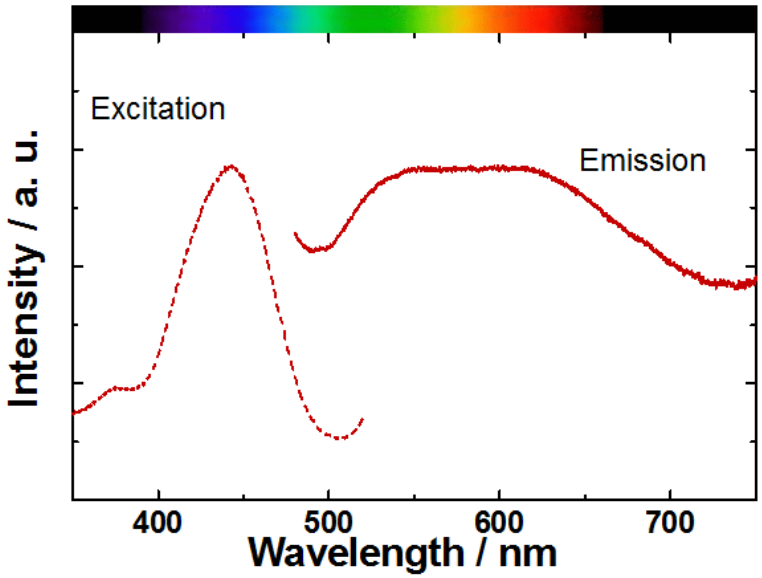

Fig. 3.3 Emission and excitation spectra of $LiSr_2YO_4:Ce^{3+}_{0.01}$ phosphor. The emission curve (in solid line) has been measured for a constant excitation wavelength of 445 nm. The excitation curve is shown in dotted line and has been recorded at 620 nm.

the high emission intensity in the green and red emission spectra. These results indicate that this phosphor is very suitable to obtain high CRI of white-LEDs based blue LED.

The broad emission band can be separated two broad band with peaks at 520 and 620 nm by Gaussian components. The Ce^{3+}-activated phosphors are well known to show broad emission band because the 4f electron configurations of Ce^{3+} has two ground states: $^2F_{5/2}$ and $^2F_{7/2}$.[49,84,89] The theoretical energy difference of the splitting between $^2F_{5/2}$ and $^2F_{7/2}$ level is approximately 2000 cm^{-1},[56,89,90] but the difference of the emission band position separated by Gaussian components of the $LiSr_2Y_{0.99}Ce_{0.01}O_4$ phosphors is approximately 3102 cm^{-1}. This result indicates that the extremely broad emission band of the $LiSr_2Y_{0.99}Ce_{0.01}O_4$ phosphors is due to the different emission centers in accordance with the different crystallographic environment of Ce^{3+} in the $LiSr_2YO_4$ host lattice. As pointed out in the introduction, the $LiSr_2YO_4$ has the crystallographically different three cation sites, which can be substituted by the Ce^{3+} ions, such as SrO_n (n = 6 and 7) polyhedral and YO_6 octahedral sites. According to the crystal field theory,[91] the crystal field strength around Ce^{3+} greatly depends on the bond distance between the Ce^{3+} and O^{2-} in the host lattice, namely, the crystal field strength generally increases with decreasing the bond distance of M−O in the crystal lattice. Where M is cation of dopant site for Ce^{3+}. The strong crystal field strength contribute to the larger energy splitting of 5d excited level of Ce^{3+}, which usually results in the emission band shift to longer wavelength side.[53,84] In the crystal structure of $LiSr_2YO_4$, the average bond distances of SrO_6, SrO_7, and YO_6 are 0.2564, 0.2657, and 0.2339 nm, respectively (Fig. 3.1(b)). The crystal field strength around Ce^{3+} ion in the $LiSr_2YO_4$ host lattice become in order of SrO_7 <

SrO_6 < YO_6, indicating that the green and red emission of the $LiSr_2Y_{0.99}O_4:Ce^{3+}_{0.01}$ phosphor can be ascribed to Ce^{3+} ion doped into the SrO_6 and YO_6 octahedral site, respectively.

Figure 3.4 shows the temperature dependence of the green and red emission peak intensities of the $LiSr_2Y_{0.99}Ce_{0.01}O_4$ phosphor. Since the temperature dependence of the phosphor is to have strong influence on the light output and CRI of white-LEDs, it is significantly important to use in the white-LEDs application.[92] The emission intensity of the phosphors is well known to decrease with increasing the temperature due to the thermal quenching.[53] The emission peak intensity of the $LiSr_2Y_{0.99}Ce_{0.01}O_4$ phosphor is also decreased with increasing the temperature and the peak intensities of the green and red emission measured at 100 °C are 54% and 25%, respectively, of that measured at 20 °C. The thermal quenching behavior of the phosphors is generally described due to the thermal relaxation process from the potential curve of the 5d electron to the potential curve of the 4f ground state

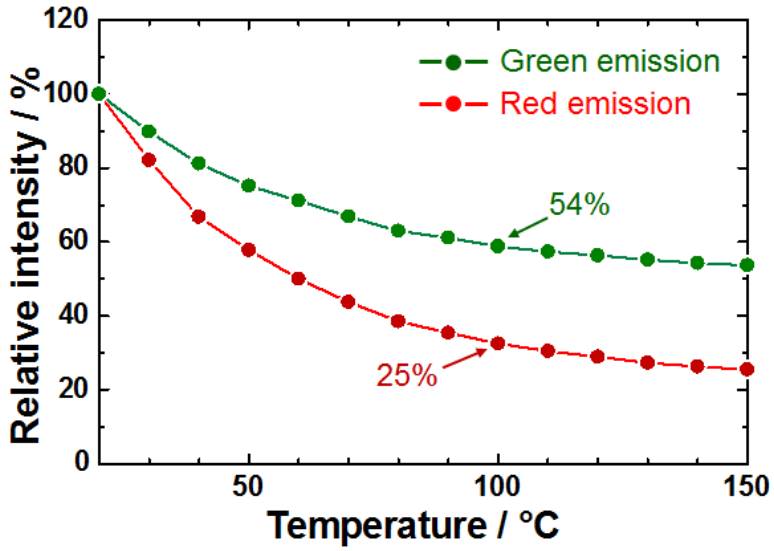

Fig. 3.4 Temperature dependence of normalized intensities for green (circle) and red (triangle) emission of $LiSr_2YO_4:Ce^{3+}_{0.01}$ phosphor.

through the crossing point in the configuration coordinate diagram.[93-95] The thermal activation energy (ΔE) for the thermal quenching of the Ce^{3+}-activated phosphors due to the thermal relaxation process can be estimated approximately using the following Arrhenius equation:[96]

$$\ln\left(\frac{I_0}{I_T} - 1\right) = \ln A - \frac{\Delta E}{kT} \qquad \text{Eq. 3.1}$$

where I_0 and I_T are the emission intensity at initial temperature and the testing temperature, respectively, A is a constant, ΔE is activation energy for thermal quenching, and k_B is the Boltzmann Constant (8.629×10^{-5} eV). The plot of $\ln[(I_0/I_T)-1]$ as a function of 1000/T for the green and red emission of $LiSr_2Y_{0.99}O_4:Ce^{3+}_{0.01}$ phosphor based on the temperature dependence is shown in Fig. 3.5. A linear relation between $\ln[(I_0/I_T)-1]$ and kT is obviously found and the slopes of green and red emission are −0.3660 and −0.4338, respectively. According to the Arrhenius equation, the activation energy (ΔE) of the green and red emission were calculated to be approximately 0.3660 and 0.4338 eV, respectively. The different activation

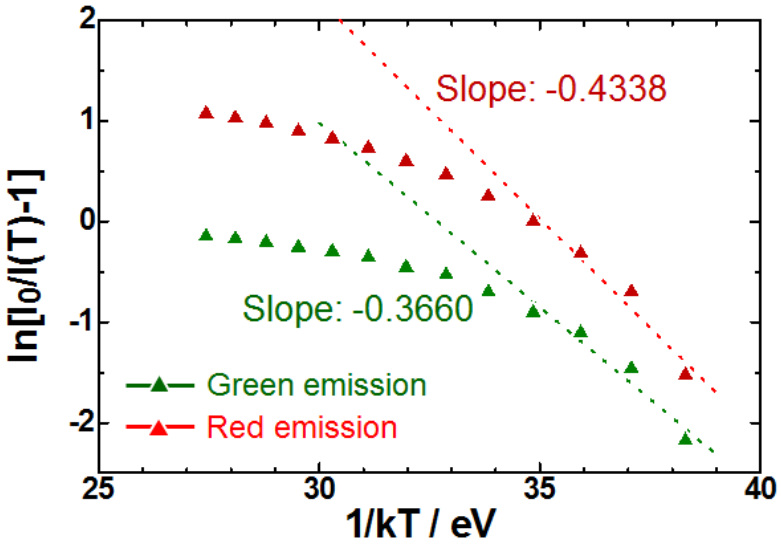

Fig. 3.5 Arrhenius fitting of the emission intensity of $LiSr_2YO_4:Ce^{3+}_{0.01}$ phosphor.

energy is become the cause of the different thermal quenching behavior of the green and red emission of $LiSr_2Y_{0.99}Ce_{0.01}O_4$ phosphor.

3.4 Summary

Novel Ce^{3+}-activated $LiSr_2YO_4$ phosphors were synthesized by a conventional solid-state reaction method. By the X-ray diffraction (XRD) measurement, the orthorhombic $LiSr_2YO_4$ structure with high crystalline was obtained as main phase in all samples. These phosphors exhibit two broad emission bands with peaks at around 520 and 620 nm due to 5d → 4f transition of Ce^{3+} under blue light excitation (λ_{ex} = 443 nm). The $LiSr_2YO_4:Ce^{3+}$ phosphors are expected to be promising phosphor for use in blue-LED based white-LEDs phosphor with high color rendering index.

Chapter 4

Double Emission with Blue and Red of Novel $Y_{17.33}B_8O_{38}:Ce^{3+}$ phosphors and Enhancement of Red Emission Efficiency by Crystal Site Engineering Technique by Co-doping with Heterogeneous Lanthanides

4.1 Introduction

Ce^{3+}-activated phosphors have been attracted much attention for white-LEDs because it can be expected to show the high CRI,[97] which exhibits extremely broad emission band owing to two ground states of $^2F_{5/2}$ and $^2F_{7/2}$.[43] In addition, the excitation and emission bands due to 4f-5d spin allowed transition of Ce^{3+} ions strongly depend on the crystal field strength of the 5d orbital of Ce^{3+} in the host lattice.[4] Thus, it is important to appropriately select the host material in order to obtain the red-emission corresponding to 5d-4f transition of Ce^{3+}. The crystal field strength generally increases with the shortening of the bond distance between the center metal and coordinated anions.[91] Therefore, the emission band position of Ce^{3+}-activated phosphor generally located at longer wavelength side when Ce^{3+} doped into the small site with a short bond distance between the cation and oxide anion in the lattice.

In this chapter, we focused on $Y_{17.33}B_8O_{38}$ ($Y_{17.33}(BO_3)_4(B_2O_5)_2O_{16}$) as the host lattice for the Ce^{3+}-activated oxide phosphor. The crystal structure of the $Y_{17.33}B_8O_{38}$ is illustrated in Fig. 4.1(a), which used a VESTA program.[60] $Y_{17.33}B_8O_{38}$ has a monoclinic structure with a space group of *Cm* (No. 8), which contains two kinds of different independent triangular borate units, BO_3 and B_2O_5. [24] In the $Y_{17.33}B_8O_{38}$ host

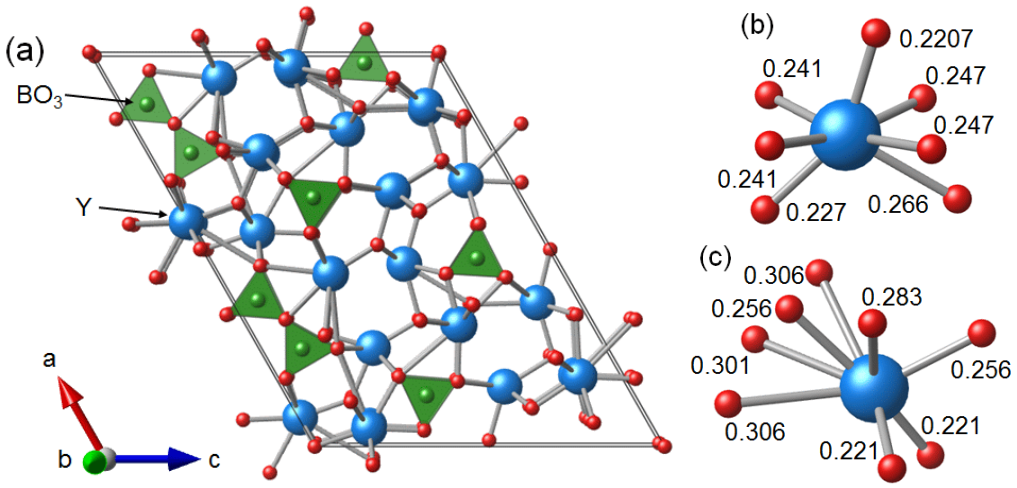

Fig. 4.1 (a) Crystal structure of $Y_{17.33}B_8O_{38}$ host material and (b) the coordination environment of the two different Y^{3+} sites. The unit is nm.

lattice, the Y^{3+} ions in the host lattice form two types coordination, such as YO_7 and YO_8 polyhedra, which has the bond distances of 0.220-0.238 nm and 0221-0.306 nm, respectively,[98] as shown in Fig. 4.1 (b). From the crystallographic approach, $Y_{17.33}B_8O_{38}$ host material is expected to the obtaining the emission band in longer wavelength side when Ce^{3+} doped selectively into the YO_7 polyhedron site in the $Y_{17.33}B_8O_{38}$ lattice, because the YO_7 polyhedra consisting from the shorter bond distances leads to being the strong crystal field strength. In the present chapter, $(Y,Ce)_{17.33}B_8O_{38}$ phosphor was synthesized by a conventional solid-state reaction method, and was investigated luminescence properties. In addition, the 5d levels positions were estimated from spectroscopic data of the $(Y,Ce)_{17.33}B_8O_{38}$ phosphor, and were compared with the other phosphor materials. Furthermore, in order to enhance the emission efficiency of $(Y,Ce)_{17.33}B_8O_{38}$ phosphor, the effects for the co-doping heterogeneous lanthanide cations to luminescence properties were also investigated.

4.2 Experimental section

Synthesis of materials. Polycrystalline $(Y,Ce)_{17.33}B_8O_{38}$ and $(Y,Ce,Ln)_{17.33}B_8O_{38}$ (Ln = La, Gd and Lu) phosphors were synthesized by the conventional solid-state reaction method using the powders of Y_2O_3, H_3BO_3, CeO_2 and lanthanide (La, Gd and Lu) oxides as the raw materials. These powders were mixed in a stoichiometric ratio using an agate mortar with an acetone. After drying, these mixtures were heated at 850°C for 6 h in air. Subsequently, the heated powders were uniformly reground using an alumina mortar, and were calcined at 1200°C for 6 h in a reducing atmosphere.

Materials characterization. The samples were characterized by X-ray powder diffraction (XRD; Mac Science Ltd. MX-Labo). The emission (PL) and excitation (PLE) spectra were measured at room temperature using a spectrofluorometer (Jasco Corp; FP-6500/6600).

4.3 Results and discussion

Ce^{3+}-doped $Y_{17.33}B_8O_{38}$. A crystal phase of the prepared Ce^{3+}-doped $Y_{17.33}B_8O_{38}$ phosphors were determined from XRD pattern, as shown in Fig. 4.2 respectively. All of the diffraction peaks of the Ce^{3+} doped phosphor samples were in good agreement with the monoclinic phase of $Y_{16.86}B_8O_{38}$ from an inorganic crystal structure database (ICSD #84966),[98] and could not observe the peaks corresponding to an impurity phase, which indicates that the single phase of $Y_{17.33}B_8O_{38}$ powder can be obtained in this synthesis condition. The composition of $Y_{17.33}B_8O_{38}$ is deferent to the corresponded monoclinic $Y_{16.86}B_8O_{38}$, which can be explained that the $Y_{16.86}B_8O_{38}$ is isostructural with $Y_{17.33}B_8O_{38}$, and consists of the yttrium defect.[98] Thus, those obtained phosphor samples can be identified to form the isostructural with the monoclinic $Y_{16.86}B_8O_{38}$ phase. A diffraction peak of the Ce^{3+} doped $Y_{17.33}B_8O_{38}$ phosphors were gradually shifted to lower angle side than that of the $Y_{17.33}B_8O_{38}$ host material with increasing the doped Ce^{3+} concentration, as shown in Fig. 4.2. This result indicates that the Ce^{3+} ion could be substituted with Y site in the host structure because the ionic radius of Ce^{3+} ion (0.107 and 0.1143 nm for 7- and 8-coordination,

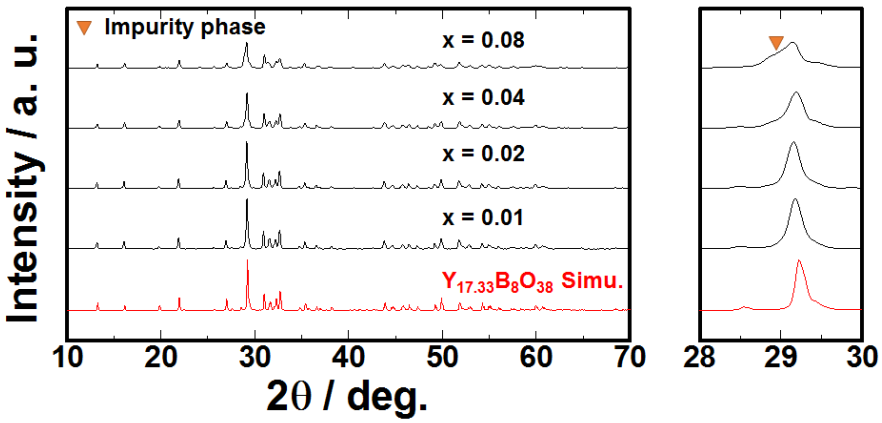

Fig. 4.2 XRD patterns of (a) $(Y_{1-x}Ce_x)_{17.33}B_8O_{38}$ ($0 \le x \le 0.08$) phosphors.

respectively)[61] is larger than that of Y^{3+} ion (0.096 and 0.1019 nm for 7- and 8-coordination, respectively),[61] which leads to the lattice expansion. Furthermore, in the $(Y_{0.92}Ce_{0.08})_{17.33}B_8O_{38}$ phosphor, the peaks due to an impurity phase were observed, and the diffraction peak was not shifted to both angle sides which indicates that a solid-solubility limit of Ce^{3+} into $Y_{17.33}B_8O_{38}$ host lattice can be estimated to locate in the between x = 0.04 and 0.08.

We could observe the two emission spectra under the irradiation of different excitation wavelengths, UV-light and blue light. Figure 4.3 shows the photoluminescence excitation and emission spectra of the $(Y_{0.96}Ce_{0.04})_{17.33}B_8O_{38}$ phosphor sample. Here, the emission spectrum of Fig. 4.3 (a) and (b) were measured using a UV-light excitation of 360 nm and a blue-light excitation of 430 nm, respectively. From Fig. 4.3 (a), the excitation spectrum of $(Y_{0.96}Ce_{0.04})_{17.33}B_8O_{38}$ phosphor sample consists of a broad band from 300 to 400 nm centered at 360 nm, which is due to the optical absorption from the $4f^1$ ground levels to excited $5d^1$ level of Ce^{3+} ion. The emission spectrum exhibits a broad blue emission from 350 nm to 500 nm peaked at 424 nm owing to the $5d^1 \rightarrow 4f^1$ arrowed transition of Ce^{3+} ion. In contrast, under blue-light irradiation excitation of 430 nm, the emission band of same phosphor sample located the red region at 620 nm, which corresponds similar to the luminescence mechanism in the case of under the UV-light excitation. In general, the emission spectrum of Ce^{3+} consists of two emission bands due to $^2D_{3/2} \rightarrow {}^2F_{5/2}$ and $^2F_{7/2}$ transitions corresponding to an energy gap of approximately $\sim 2\times10^3$ cm^{-1}.[43,68,73,99-101] However, Ce^{3+}-doped $Y_{17.33}B_8O_{38}$ phosphor consists of significantly different two emission bands with the energy gap of approximately 7.50×10^3 cm^{-1}, which indicates that the Ce^{3+} ions were doped into the completely

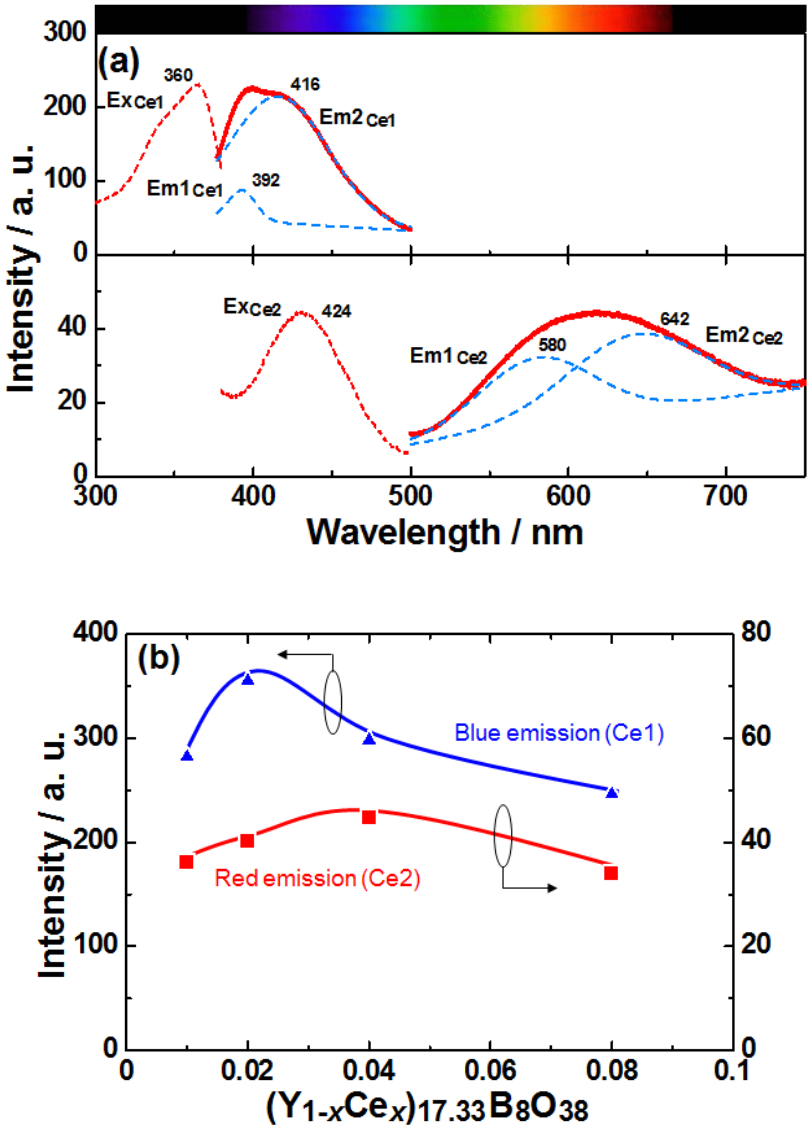

Fig. 4.3 (a) Photoluminescence excitation and emission spectra of $(Y_{0.96}Ce_{0.04})_{17.33}B_8O_{38}$ phosphor under the UV-light excitation of 360 nm, and under the blue-light excitation of 424 nm, with two Gaussian fitting peaks. (b) The emission intensity dependences of the Ce^{3+} concentration of the $(Y_{1-x}Ce_x)_{17.33}B_8O_{38}$ ($0 \le x \le 0.08$) phosphors.

different crystallographic Y^{3+} sites in the host lattice. In the $Y_{17.33}B_8O_{38}$ lattice, the Y^{3+} ions form YO_7 and YO_8 polyhedra by the coordination with the surrounding seven and eight oxygen (see Fig. 4.1). In particular, the bond distance of YO_7 polyhedron is shorter (avg. 0.228 nm) than that of YO_8 polyhedron (avg. 0.273 nm). Thus, YO_7 polyhedra means to form a compact crystallographic site.

These emission spectra were deconvoluted to two Gaussian functions corresponding to the transition from the $^2D_{3/2}$ excited level to $^2F_{7/2}$ and $^2F_{5/2}$ ground levels of Ce^{3+}. In the emission spectrum at blue region, the peak maxima of the deconvoluted emission spectrum located at 392 ($^2D_{3/2}\rightarrow{}^2F_{5/2}$) and 416 nm ($^2D_{3/2}\rightarrow{}^2F_{7/2}$), respectively. The energy difference between the ground levels split by a spin-orbit interaction estimated to be 1.5×10^3 cm^{-1} by the emission bands obtained from the Gaussian deconvolution. On the other hand, the emission spectrum at red region could be also deconvoluted to two Gaussian function with the peaked at 580 and 642 nm, respectively. The energy between $^2F_{5/2}$ and $^2F_{7/2}$ levels could be estimated to be 1.6×10^3 cm^{-1}. Although these energy gap of $^2F_{5/2}$ and $^2F_{7/2}$ levels is slightly less than that of theoretical value of 2000 cm^{-1},[68,73,99-101] since the comparable value of the energy gap was reported in the other Ce^{3+}-activated lanthanide borate phosphors, such as $YBO_3:Ce^{3+}$ (1.55×10^3 cm^{-1})[102] and $Ca_3La_3(BO_3)_5:Ce^{3+}$ (1.77×10^3 cm^{-1})[103].

In order to more deeply understand for the influence for the crystallographic site of luminescence of Ce^{3+}, it is important to know the position of the excited 5d levels of Ce^{3+} ions. According to Dorenbos, the total energy shift from the free ion to the lowest 5d configuration can be written as;[104,105]

$$D(A) = \varepsilon_c + \frac{\varepsilon_{cfs}}{r(A)} - 1.89 \times 10^3 \text{ cm}^{-1} \qquad \text{Eq. 4.1}$$

where a red shift value, $D(A)$ is often used to estimate a total energy depression from the free ion, which is containing the centroid shift and crystal field splitting. The lowering of the average of the five 5d levels is represented by the centroid shift ε_c due to the interaction of the 5d-electron wavefunctions and ligand anions, which relates with a nephelauxetic effect. The strength of the crystal field splitting ε_{cfs} is

defined as the energy gap between highest and lowest 5d levels. The ε_{cfs} value depends on the geometrical shape and size of the polyhedrons. The red shift $D(A)$ gives to a fraction $1/r(A)$, which is usually between 1.7 and 2.4.[105,106] In the case of Ce^{3+}-doped $Y_{17.33}B_8O_{38}$ phosphor, it is not need to calculate the crystal field splitting ε_{cfs}, because there is a need to know the lowest 5d level. Thus, the important factors are the red shift $D(A)$ and centroid shift ε_c in order to obtain the split lowest 5d level. The red shift could be expressed by following equation;[69,107]

$$D(A) = E(Ce, free) + \Delta E^{Ln,Ce} - E(Ln, A), \qquad \text{Eq. 4.2}$$

where $E(Ce, free)$ is the first f-d transition energy Ce^{3+} as a free ion, which used value of 49.34×10^3 cm^{-1},[69,107] $\Delta E^{Ln,Ce}$ is defined as the specific energy difference in f-d transition of Ln^{3+} with that of the first electric dipole allowed transition in Ce^{3+}, as see Ref 69, and $E(Ln, A)$ is the f-d energy difference of compounds A with Ln^{3+} as a dopant. In the case of Ce^{3+}, the $D(A)$ is rewritten as

$$D(A) = 49.34 \times 10^3\ \text{cm}^{-1} - E(Ce, A). \qquad \text{Eq. 4.3}$$

The centroid shift ε_c is associated with anion polarizanility and the average cation electronegativity. The 5d centroid shift can be estimated by gain into account the Ce^{3+}-O^{2-} bond distances combining with average anion electronegativity. The model for the 5d centroid shift is described in the following equation:[108,109]

$$\varepsilon_c = 1.79 \times 10^{13} \sum_{i=1}^{N} \frac{\alpha_{sp}^i}{(R_i - 0.6\Delta R)^6} \qquad \text{Eq. 4.4}$$

where R_i is the bond distance (pm) for the Ce^{3+}-O^{2-} ions in the lattice, ΔR is the deference in the ionic radii for Y^{3+} and Ce^{3+}, and N represents the number of anions coordinated with Ce^{3+} ion. The α_{sp}^i is the spectroscopic polarizability, as described in the following equation;[110]

$$\alpha_{sp}^{i} = 0.33 + \frac{4.8}{\chi_{av}{}^{2}}. \qquad \text{Eq. 4.5}$$

Here, χ_{av} is the weighted average of the cation electronegativity in a given host lattice. The 5d level positions parameters for the red shift $D(A)$, centroid shift are summarized in Table 4.1, and Fig. 4.4 presents the schematic energy diagrams for the each transitions due to Ce1 (blue emission) and Ce2 (red emission) transitions in Ce^{3+}-doped $Y_{17.33}B_8O_{38}$ phosphor.

Using the Eq. 4.3, the red shift $D(A)$ of two f-d transitions in Ce^{3+}-doped $Y_{17.33}B_8O_{38}$ phosphor was found to be 21.7×10^3 cm^{-1} for Ce1 transition and 25.7×10^3 cm^{-1} for Ce2 transition, respectively. Dorenbos has reported to the $D(A)$ data of the more than 350 compounds, which is including the 38 Ce^{3+}-doped borates hosts,[111] and the $D(A)$ value of typical borates is also summarized in Table 4.1. According to the summary in Dorenbos's report, the $D(A)$ borates was generally increased in the order of condensed-, meta-, ortho- and oxy-ortho-borates.[111] The $Y_{17.33}B_8O_{38}$ ($Y_{17.33}(BO_3)_4(B_2O_5)_2O_{16}$) can be classified as the oxy-ortho-borate group because its

Table 4.1 Emission band positions, centroid shifts ε_c, red shift $D(A)$ and Stokes shifts ΔS of each transitions of 4f-5d of Ce^{3+} in $(Y_{0.96}Ce_{0.04})_{17.33}B_8O_{38}$, and the typical borate phosphors.

Borates	Condense group	λem[a]	ε_c[b]	D(A)[b]	ΔS[b]	Ref.
$Y_{17.33}B_8O_{38}$ (Ce1)	oxy-ortho-	392 / 25.5	7.86	21.7	2.27	This work
$Y_{17.33}B_8O_{38}$ (Ce2)	oxy-ortho-	580 / 17.2	15.3	25.7	6.51	This work
SrB_4O_7	condensed-	293 / 34.1	8.44	14.1	1.56	111, 112
$BaTbB_9O_{16}$	condensed-	321 / 31.1	-[c]	15.6	2.52	111, 113
LaB_3O_6	meta-	300 / 33.3	8.99	12.3	3.70	105, 111, 114
$YMgB_5O_{10}$	meta-	300 / 33.3	8.73	12.4	3.57	105, 111, 115
$LaBO_3$	ortho-	352 / 28.4	11.5	19.0	2.30	105, 111, 116
$GdAl_3(BO_4)_4$	ortho-	338 / 29.6	10.3	18.1	1.66	105, 111, 117
YBO_3	ortho-	383 / 26.1	<13.3	20.8	1.88	105, 111, 118
$Ca_4YO(BO_3)_3$[d]	oxy-ortho-	390 / 25.6	<14.3	21.9	2.61	111, 119
$CaYOBO_3$	oxy-ortho-	400 / 25.0	<15.3	21.9	2.40	111, 120

[a] Unit is nm / $\times10^3$ cm^{-1}.
[b] Unit is $\times10^3$ cm^{-1}.
[c] Structural data is not available.
[d] From the structural data of $Ca_{4.084}Y_{0.916}(BO_3)O_{0.96}$

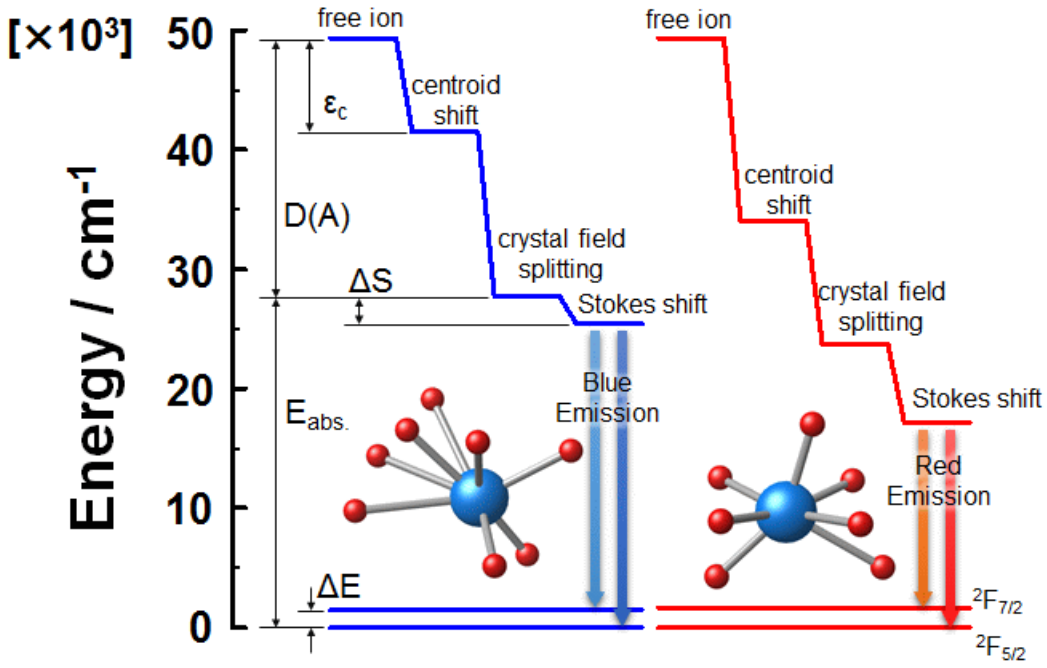

Fig. 4.4 Schematic energy diagrams for the each transitions due to Ce1 (blue) and Ce2 (red) transitions in Ce^{3+}-doped $Y_{17.33}B_8O_{38}$ phosphor.

structure consists of B_2O_5 and BO_4 polyhedra and independent oxygen atoms.[98] The f-d transition for red emission (Ce2) of Ce^{3+}-doped $Y_{17.33}B_8O_{38}$ shows larger $D(A)$ value compared with the Ce^{3+}-doped $CaYOBO_3$ (21.9×10^3 cm^{-1}),[111,120] which shows most large value in borates. Using the above Eq. 4.4 and 4.5, the 5d centroid shift for the transitions due to blue and red emissions of Ce^{3+}-doped $Y_{17.33}B_8O_{38}$ phosphor were estimated to be 7.86×10^3 and 15.3×10^3 cm^{-1}, respectively. The value of centroid shifts for Ce1 transition was similar to that of some typical Ce^{3+}-doped borates phosphor, such as LaB_3O_6 (8.99×10^3 cm^{-1})[114] and $YMgB_5O_{10}$ (8.73×10^3 cm^{-1}).[115] The Ce^{3+} ion was occupied to irregular C_2 and C_1 symmetries for LaB_3O_6 and $YMgB_5O_{10}$, respectively,[105] which suggests that the Ce1 due to blue emission occupied in the irregular symmetry site, *i.e.* the distorted 8-fold coordination sites. On the other

hands, the value of centroid shift for Ce2 transition shows the largest energy depression in the borate phosphors. The 5d centroid shift of $Y_{17.33}B_8O_{38}:Ce^{3+}$ phosphor is more than that of the garnet oxides like the $Y_3Al_5O_{12}:Ce^{3+}$ (14.7×10^3 cm^{-1}),[106,121] as well as, it is comparable to that of nitrides phosphor, such as $CaAlSiN_3:Ce^{3+}$ (19.7×10^3 cm^{-1}) [77] and $(La,Ca)_3Si_6N_{11}:Ce^{3+}$ (28.8×10^3 cm^{-1}).[78] This indicates that the seven-coordinated Y site in $Y_{17.33}B_8O_{38}$ leads to the strong nepherauxetic effect, because the most nitrides induced very large covalency.[122]

In addition, the Stokes shift (ΔS), which determines as the deference between the lowest excitation band and emission band with highest energy, is also important to understand for the luminescence mechanism of Ce^{3+}-doped $Y_{17.33}B_8O_{38}$, as also noted in Table 4.1. The Stokes shifts of the Ce1 and Ce2 transitions were found to be 2.27×10^3 cm^{-1} and 6.51×10^3 cm^{-1}, respectively. The magnitude for the Stokes shift of Ce1 transition, which is due to the blue emission, was comparable to that of the typical Ce^{3+}-doped borate phosphors, as seen in Table 4.1. In contrast, the Stokes shift of the red emitted Ce2 transition was much larger than that of the conventional borates phosphors.[111] van Krevel et al. concluded that the magnitude of Stokes shift decreases with increasing the structural rigidity of the lattice, *i.e.* the Ln^{3+} incorporated into the host lattice with three dimensional framework leads to reduction of the Stokes shift.[123] The $Y_{17.33}B_8O_{38}$ host lattice consists of the non-rigid structural independent BO_3 and B_2O_5 polyhedra, which causes to increase the Stokes shift. Furthermore, the thermal quenching temperature depends on the Stokes shift.[55] In the case of the large Stokes shift, the thermal quenching temperature becomes relatively low.[123]

The thermal quenching properties are typically discussed by an activation energy E_a, which can be explained by following equation;[124]

$$\frac{I_T}{I_0} = 1 + Dexp\left(\frac{-E_a}{kT}\right) \qquad \text{Eq. 4.6}$$

where, the values of I are the emission intensities of the phosphor material at an initial (25°C) for I_0 and the monitored temperature for I_T, respectively, D is an constant, k is the Boltzmann's constant (8.617×10^{-5} eV·K^{-1}) and T is the operating temperature. The activation energies due to each emission of Ce^{3+} were found to be 0.169 eV for Ce1 transition (blue emission) and 0.322 eV for Ce2 transition (red

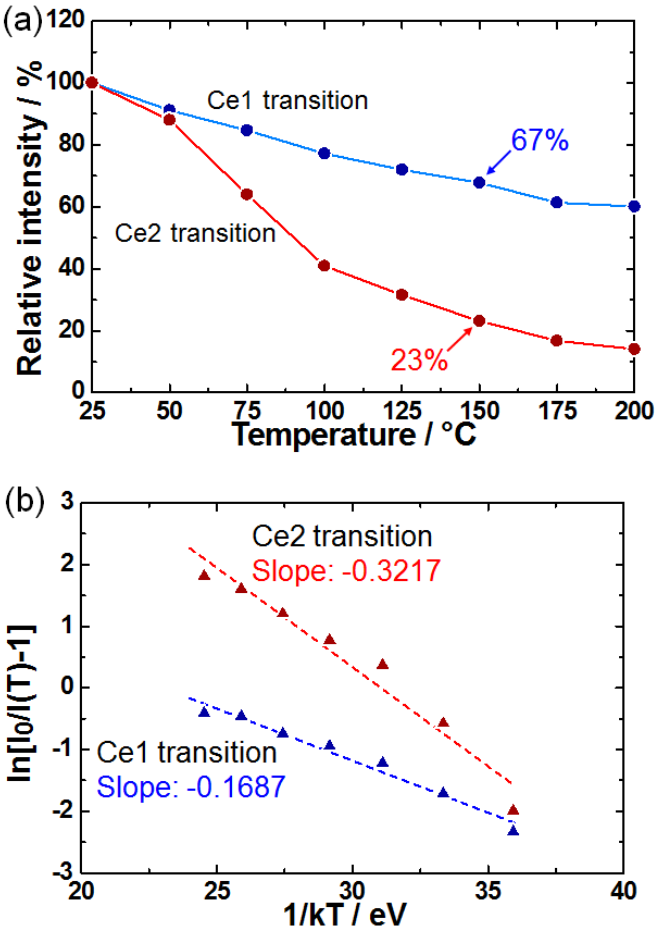

Fig. 4.5 (a) Temperature dependence on the emission intensities of Ce^{3+}-doped $Y_{17.33}B_8O_{38}$ phosphor. (b) The plot of $\ln[I_0/I(T)-1]$ vs. 1/kT of the Ce^{3+}-doped $Y_{17.33}B_8O_{38}$ phosphor.

emission), respectively, as shown in Fig 4.5 (a). In addition, with increasing the temperature up to 150°C, the emission intensities of $(Y_{0.96}Ce_{0.04})_{17.33}B_8O_{38}$ phosphor decrease to 23% for the blue emission of Ce1 and 67% for the red emission of Ce2, respectively, as shown in Fig. 4.5 (b). This results are also reasonable to describe the deference of ΔS between the Ce1 and Ce2 transitions.

Heterogeneous lanthanides co-doping with $(Y_{0.96}Ce_{0.04})_{17.33}B_8O_{38}$. When the Ce^{3+} ions occupy some different crystallographic sites, the emission efficiency cannot be sufficiently obtained by the energy loss due to an energy transfer of a re-absorption mechanism. Therefore, the luminescence efficiency of the red emission enhances by a selective control of the Ce^{3+} doping site in the $(Y_{0.96}Ce_{0.04})_{17.33}B_8O_{38}$ phosphor. This approach calls "crystal-site engineering",[22,37,52] and is extremely effective for the control of the emission color of the phosphor materials because the host lattice of the many phosphor materials has some crystallographic sites. The doping site of the activators in α'_L-type $Ca_2SiO_4:Eu^{2+}$ [22] and $Sr_6Y_2Al_4O_{15}:Ce^{3+}$ [52] phosphors gradually change from large site to small site by the increasing activator concentration, which results in the changing from green to red emission for the $Ca_2SiO_4:Eu^{2+}$ phosphor and blue to orange emission for the $Sr_6Y_2Al_4O_{15}:Ce^{3+}$ phosphor, respectively. [22,37,52] In this case of $(Y_{0.96}Ce_{0.04})_{17.33}B_8O_{38}$ phosphor, the Ce^{3+} concentration cannot be increased because impurity phase observed in x = 0.08 on the composition of $(Y_{1-x}Ce_x)_{17.33}B_8O_{38}$. In order to enhance the red emission intensity of the $(Y_{0.96}Ce_{0.04})_{17.33}B_8O_{38}$ phosphor, some heterogeneous lanthanide cations were co-doped into that phosphor. The different ionic radii lanthanide ions doping the

$(Y_{0.96}Ce_{0.04})_{17.33}B_8O_{38}$ phosphor lattice were discussed an influence to the emission properties.

Figure 4.6 shows the Ce^{3+}, Ln^{3+} (Ln= Lu^{3+}, Gd^{3+} and La^{3+}) co-doped $Y_{17.33}B_8O_{38}$ phosphors. All samples for the Ln^{3+} co-doped $(Y_{0.96}Ce_{0.04})_{17.33}B_8O_{38}$ phosphors were also identified to monoclinic $Y_{16.86}B_8O_{38}$ as the single phase. A diffraction peak of the Lu^{3+} and Gd^{3+} co-doped $(Y_{0.96}Ce_{0.04})_{17.33}B_8O_{38}$ phosphors shifted to higher angle side than that of $(Y_{0.96}Ce_{0.04})_{17.33}B_8O_{38}$ phosphor. By contrast, the diffraction peak of the La^{3+} co-doped $(Y_{0.96}Ce_{0.04})_{17.33}B_8O_{38}$ phosphors shifted to lower angle side. This results indicate that the lanthanide ions was successfully substituted into the same crystallographic site with Ce^{3+} ion doping because the La^{3+} ion (0.110 and 0.1160 nm for 7- and 8-coordination, respectively)[61] has larger ionic size, as well as the Gd^{3+} (0.100 and 0.1053 nm for 7- and 8-coordination, respectively)[61] and Lu^{3+} (0.0977 nm for 8-coordination)[61] ions have lager ionic size compared with the Ce^{3+} ionic size, which respectively results in the lattice volume expansion and contraction.

Figure 4.7 (a) and (b) shows the emission spectra of $(Y_{0.92}Ce_{0.04}Ln_{0.04})_{17.33}B_8O_{38}$ (Ln = La, Gd and Lu) phosphors under the UV light at wavelength of 360 nm and the

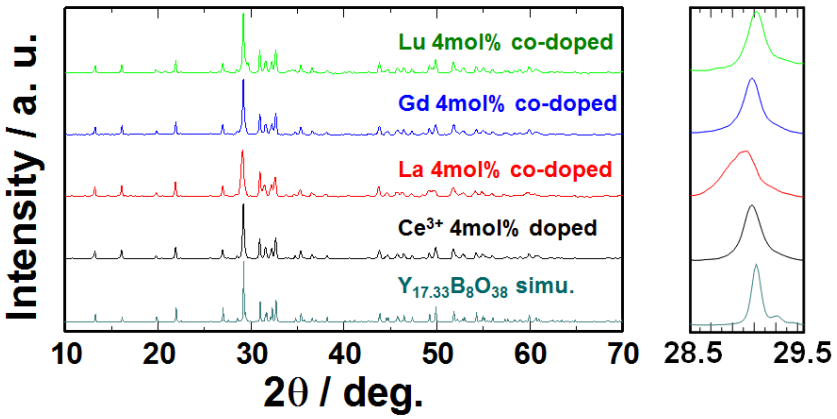

Fig. 4.6 XRD patterns of $(Y_{0.96}Ce_{0.04})_{17.33}B_8O_{38}$ and $(Y_{0.92}Ce_{0.04}Ln_{0.04})_{17.33}B_8O_{38}$ (Ln= Lu^{3+}, Gd^{3+}, La^{3+}) phosphors.

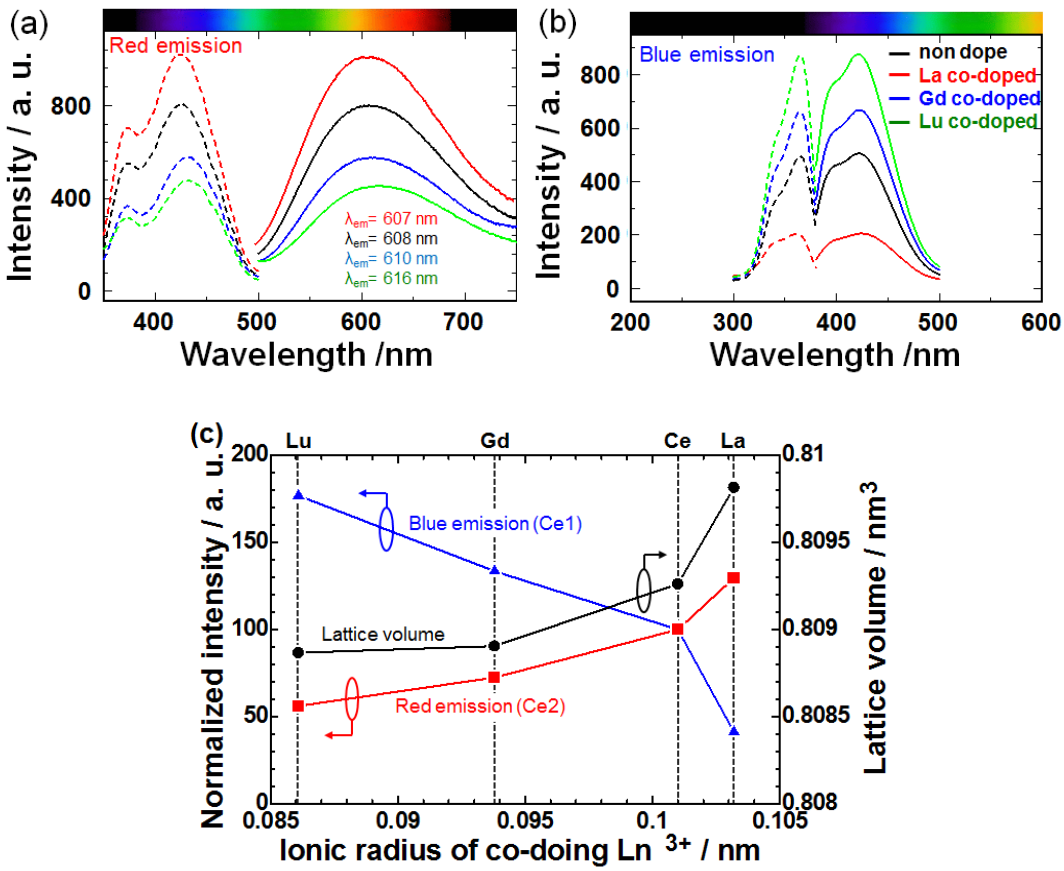

Fig. 4.7 (a) Photoluminescence excitation and emission spectra of $(Y_{0.96}Ce_{0.04})_{17.33}B_8O_{38}$ and $(Y_{0.92}Ce_{0.04}Ln_{0.04})_{17.33}B_8O_{38}$ (Ln= Lu^{3+}, Gd^{3+}, La^{3+}) phosphors under the UV-light excitation of 360 nm. (b) Photoluminescence excitation and emission spectra of these phosphors under the blue-light excitation of 421 nm. (c) Dependences of two emission intensities and lattice volume on ionic radius of the various cations doping into Y site of $(Y_{0.92}Ce_{0.04}Ln_{0.04})_{17.33}B_8O_{38}$ phosphors (Ln = Lu^{3+}, Gd^{3+}, La^{3+}).

blue light irradiation at wavelength of 430 nm, respectively. In addition, Fig. 4.7 (c) shows the emission intensity dependence on the ionic radius of the lanthanide ions co-doped into $(Y_{0.96}Ce_{0.04})_{17.33}B_8O_{38}$ phosphor, and the plot for lattice volumes of the ionic radius of Ln^{3+} ion co-doped into $(Y_{0.98}Ce_{0.04})_{17.33}B_8O_{38}$ phosphor. All samples exhibited a broad emission bands in the blue light region peaking at around 400 and 430 nm corresponding to 5d-4f transition of Ce^{3+} excited at UV light region. The red emission (Ce2 transition) at under the blue light excitation were also observed in the $(Y_{0.92}Ce_{0.04}Ln_{0.04})_{17.33}B_8O_{38}$ (Ln = La, Gd and Lu) phosphors, as similar to the Ce^{3+}

only doped sample. In particular, the La^{3+} co-doped phosphor exhibited the higher red emission intensity than Ce^{3+} only doped phosphor, and the lowest blue emission intensity in the all phosphors. By associating the ratio of these emission intensities and the lattice volume of the Ln^{3+} co-doped phosphors, we found that the ratio of these emission intensities depends on the ionic radius of the co-doping Ln^{3+} ions. The emission intensities at the blue region of $(Y_{0.92}Ce_{0.04}Ln_{0.04})_{17.33}B_8O_{38}$ (Ln = La, Gd and Lu) phosphors gradually decreased with increasing the ionic radius of lanthanides. On the other hands, the red emission intensity enhanced in the La^{3+} co-doping sample, and inhibited in smaller ionic radius ions co-doping samples compared to the ionic radius of Ce^{3+} ion. The increment for the red emission intensity is in good agreement with the lattice volume change in the case of each co-doping Ln^{3+} ions. This indicates that the ratio of the red and blue emission intensity (Ce2/Ce1) increased with an increase in the Ln^{3+} ionic radius, which is co-doped into $(Y_{0.98}Ce_{0.04})_{17.33}B_8O_{38}$ lattice. As mentioned above, the enhancement of the emission intensity, which based on the conventional crystal site engineering technique has been investigated by the increase of the luminescent ions, such as Eu^{2+} and Ce^{3+}.[22,37] By contrast, we succeed to enhance the red emission intensity by doping the lanthanide heterogeneous ions, which is using the lanthanide contraction, in the $(Y_{0.98}Ce_{0.04})_{17.33}B_8O_{38}$ phosphor.

4.4 Summary

We discovered a new borate phosphor material, Ce^{3+}-activated $Y_{17.33}B_8O_{38}$, which consisted of two different optical transitions. One of the luminescence show a broad blue emission with peaking at 430 nm under the UV light irradiation at 360 nm. Another one is simultaneously a red emission at 620 nm excited by the blue light irradiation at 424 nm. In the Ce^{3+}-activated borate phosphors, the red emission is significantly interesting, and this study is the first report in the world. The centroid shifts of these transitions were calculated to be 7.86×10^3 cm^{-1} for the blue emission and 15.3×10^3 cm^{-1} for the red emission, respectively. This indicates that transition of the red emission has the larger energy depression due to a covalency from free energy of Ce^{3+} compared to that of blue emission. In addition, the Stokes shifts, ΔS were also found to be 2.27×10^3 cm^{-1} (blue emission) and 6.51×10^3 cm^{-1} (red emission), respectively, The large ΔS is due to the low dimensional framework of the host lattice. In order to enhance the red emission intensity, the heterogeneous lanthanide ions, such as La^{3+}, Gd^{3+} and Lu^{3+}, were co-doped into the $(Y_{0.98}Ce_{0.04})_{17.33}B_8O_{38}$ phosphor. As the result, the emission intensity at the red region of La^{3+} co-doping phosphor was to be 129% compared to the heterogeneous ion non-co-doping phosphor. In addition, it was found that the ratio of red and blue emission intensities increase with increasing the ionic radius of co-doping ions, which could be explained by a crystal site engineering technique. To the best our knowledge, it is no report the enhancement of the emission intensity based on the crystal site engineering use of the lanthanide ion co-doping. Therefore, the heterogeneous co-doping technique can be expected to control the doping site of the luminescence ion.

Chapter 5

Crystal Structure and Photoluminescence Properties of A Novel Reddish-yellow Emitting Phosphor, $BaCa_2Y_6O_{12}:Ce^{3+}$

5.1 Introduction

In chapter 5, we focused on MRE_2O_4 (*M*=Ca, Sr and Ba, *RE*=rare earths) compounds as a host material with Ce^{3+} activator. These structures including the compact REO_6 octahedra cause the strong crystal field strength.[125] It is well known that almost MRE_2O_4 compounds have an orthorhombic calcium ferrite ($CaFe_2O_4$) type structure, and is suitable for phosphor material by doping the Ce^{3+}.[125-129] In particular, $CaSc_2O_4:Ce^{3+}$ phosphor developed by Shimomura *et al.* shows the green emission peaking at 515 nm with high luminescence efficiency (>90%).[76] On the other hand, $(Ba_{0.33}Ca_{0.67})Y_2O_4$, namely $BaCa_2Y_6O_{12}$ compound has different crystal structure with the orthorhombic $CaFe_2O_4$, and consists of polyhedra with short interatomic bond length of ~0.2357 nm for YO_6 octahedra and ~0.2475 nm for CaO_6 trigonal prism polyhedra, respectively.[130,131] Since the crystal field strength bear an inverse relation to the bond strength between activator and neighbor anions,[132] this crystallographic features are expected to cause the large crystal field splitting, when Ce^{3+} ion introduces to such ion sites.

Generally, a critical concentration of Ce^{3+} (Eu^{2+}) in the conventional phosphors is quite lower of approximately 1~5 mol% than that of 4f-4f for-bidden transitions of other lanthanide ions.[43,133] Therefore, it is difficult to diffuse uniformly the activator using the synthesis of conventional solid state reaction method. Additionally, some oxide raw materials with a high melting temperature, such as

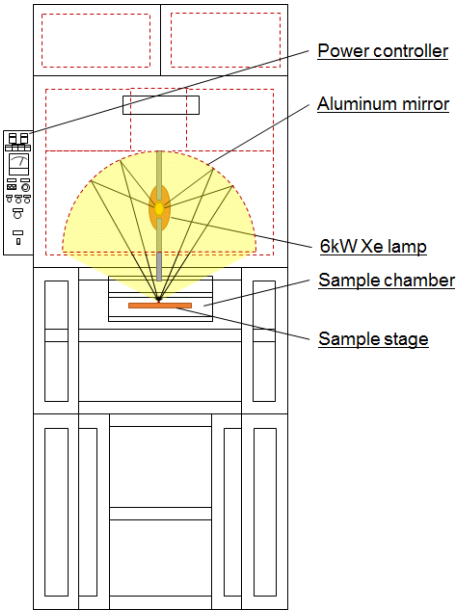

Fig. 5.1 Optical system of an arc imaging furnace.

alkali earth oxides (2899±3°C for CaO), rare earth oxides (2433±3°C for Y_2O_3) and transition metal oxides (2803±3°C for HfO_2),[134,135] have a poor reactivity. In order to overcome such problems, a melt synthesis method using an arc imaging furnace is suitable for the synthesis of phosphor materials with a small amount of the activator.[136-140] Indeed, via the synthesis of a green emitting $Ba_3Sc_4O_9:Ho^{3+}$ phosphor, the melt synthesis method using the arc imaging furnace for ceramic materials has been revealed that ions diffuse more uniform compared to the conventional solid state reaction.[140] The arc imaging furnace, which is illustrated in Fig. 5.1, uses the Xe arc lamp with 6 kW as a light source.[137] The emitted strong energy light from the Xe lamp was reflected by a surrounding ellipsoidal aluminum mirror, simultaneously, the strong light with high energy is corrected on the copper sample stage. The sample is able to be rapidly heated at over 2000°C, and also cooled by removing the sample stage from the focus. The cooling rate is estimated to be more than 100°C/s.[21,137,138]

In this chapter, the Ce^{3+} activated $BaCa_2Y_6O_{12}$ phosphors were prepared by the melt synthesis technique using the arc imaging furnace, and the crystal structure of the obtained sample was refined using powder X-ray diffraction. In addition, the luminescent property was discussed using an estimated values of 5d excited levels of Ce^{3+}.

5.2 Experimental section

Synthesis of materials. Polycrystalline Ce^{3+}-doped barium calcium yttrium oxide samples were prepared by a melt synthesis technique using an arc imaging furnace. High purity raw materials, $BaCO_3$, $CaCO_3$, Y_2O_3 and CeO_2 powder, were mixed using a mortar with an acetone for obtaining a homogeneous chemical mixture, in which Ce^{3+} content was adjusted from 0.1 to 2.0 mol%. And then, the mixtures were calcined at 1000°C for 6 h in air using an electrical box-furnace. After calcination, the samples were reground in an alumina mortar and put on the copper hearth, and melted by the corrected Xe arc lamp with a high-power of 6 kW using the arc imaging furnace in a flow of H_2 (5%)-Ar gas.

Materials characterization. The crystal phase of the powder samples were identified by a powder X-ray diffraction (XRD) analysis using a diffractometer with CuKα radiation (Mac Science Ltd. MX-Labo, λ=1.5418Å, 40 kV×25 mA), and the crystal parameters of the powder sample was refined by Rietveld method using a package of RIETAN-FP program.[63] The photoluminescence and photoluminescence excitation spectra were recorded by a spectrofluorometer of FP-6500/5500 (Jasco Co.) equipped with a 150 W Xe lamp.

5.3 Results and discussion

The crystal phase of all $BaCa_2Y_6O_{12}:Ce^{3+}$ phosphors, which were prepared by the melt synthesis technique, were checked by the X-ray diffraction (XRD). The crystal structure information of $BaCa_2Y_6O_{12}$ from Inorganic Crystal Structure Database (ICSD, No. 63580)[131] was employed as an initial structure parameters for the Rietveld refinement of the $BaCa_2Y_6O_{12}:Ce^{3+}$ phosphors. However, from view point of the R-factors, the pattern fitting and isotropic temperature factors, the unsatisfactory results were obtained in the case of the refinement using this structure model. In order to improve the quality of the Rietveld refinement for $BaCa_2Y_6O_{12}:Ce^{3+}$ phosphor, a site symmetry of the Ba1 (2b) and Ba2 (2a) sites, which extremely has a large isotropic temperature factor and the minus value of the isotropic temperature factor, were decreased, and then these sites were again refined as the shared one site (4e). In addition, the mismatch of the pattern fitting were enhanced by disordering the Ba and Ca ions for M1 (4e) and M2 (2c) sites. As the result of the re-refinement, the final converged weighted-profiles of R_{wp}=6.849%, R_p=5.291% and S=2.1459 are better value than that of the before re-refinement, which indicates the single phase with no unidentified diffraction peaks due to the impurity phase (Table 5.1). Figure 5.2 shows the final results of the data collection refinements for $BaCa_2(Y_{0.998}Ce_{0.002})_6O_{12}$ phosphor. The results of Rietveld refinements from powder XRD pattern indicated that the $BaCa_2(Y_{0.998}Ce_{0.002})_6O_{12}$ phosphor have a hexagonal crystal system with a space group of $P6_3/m$ (No. 176) and the lattice parameters of a=b=1.02178(6) nm, c=0.33612(1) nm and V=0.30391(3) nm^3, respectively. The Ba/Ca mixed ion sites, M1 (4e) and M2 (2c) sites, were occupied by the 0.15Ba/0.10Ca and 0.20Ba/0.80Ca, respectively. The

Table 5.1 *R*-factors and structural parameters of $BaCa_2(Y_{0.998}Ce_{0.002})_6O_{12}$ of Rietveld refinement from XRD data at room temperature.

formula			$BaCa_2(Y_{0.998}Ce_{0.002})_6O_{12}$		
cryst sys.			hexagonal, $P6_3/m$ (No. 176)		
a (nm)			1.02178(6)		
c (nm)			0.33612(1)		
V (nm^3)			0.30391(3)		
Z			1		
R_{wp} (%)			6.849		
R_p (%)			5.291		
R_e (%)			3.192		
R_F (%)			3.027		
S			2.1459		
atom	Wyck.	x	y	z	U_{iso} (nm^2)
M1	4e	0	0	0.347(3)	0.000(2)
M2	2c	0.3333	0.6667	0.25	0.031(2)
Y1	6h	0.3450(2)	0.9959(3)	0.25	0.0072(4)
O1	6h	0.189(1)	0.297(1)	0.25	0.006(3)
O2	6h	0.8630(8)	0.462(1)	0.25	0.027(3)

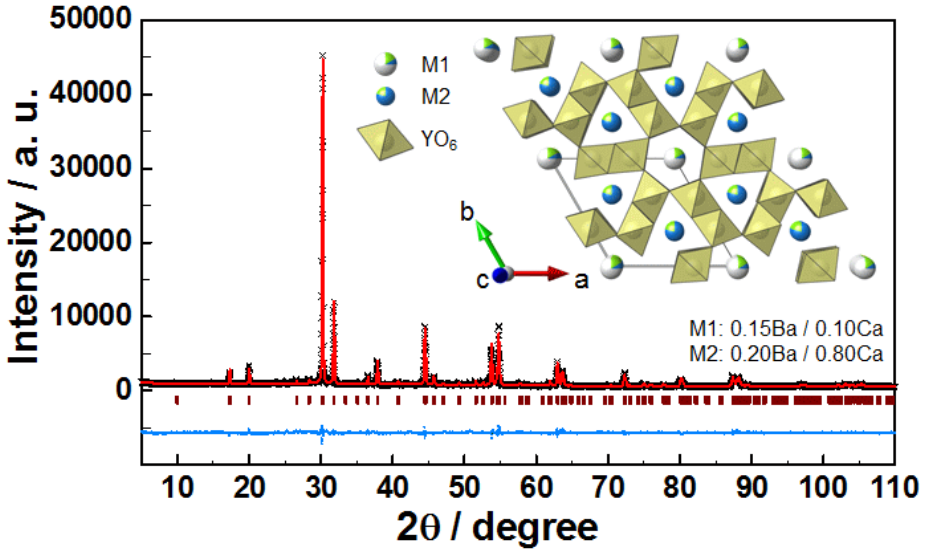

Fig. 5.2 Observed intensities (cross), calculated patterns (red line), Bragg positions (tick mark), and difference plot (blue line) profiles using powder XRD for Rietveld refinement results of $BaCa_2(Y_{0.998}Ce_{0.002})_6O_{12}$ phosphor. Inset shows the crystal structure of the $BaCa_2(Y_{0.998}Ce_{0.002})_6O_{12}$.

crystal structure of the $BaCa_2(Y_{0.998}Ce_{0.002})_6O_{12}$ lattice is also illustrated in the inset of Fig. 5.2 and Fig. 5.3 (a), using VESTA program.[60] The $BaCa_2(Y_{0.998}Ce_{0.002})_6O_{12}$ structure composed of the large amounts of YO_6 octahedral coordination site, which are connected with corner- and edge-sharing each other, and M1 and M2 sites

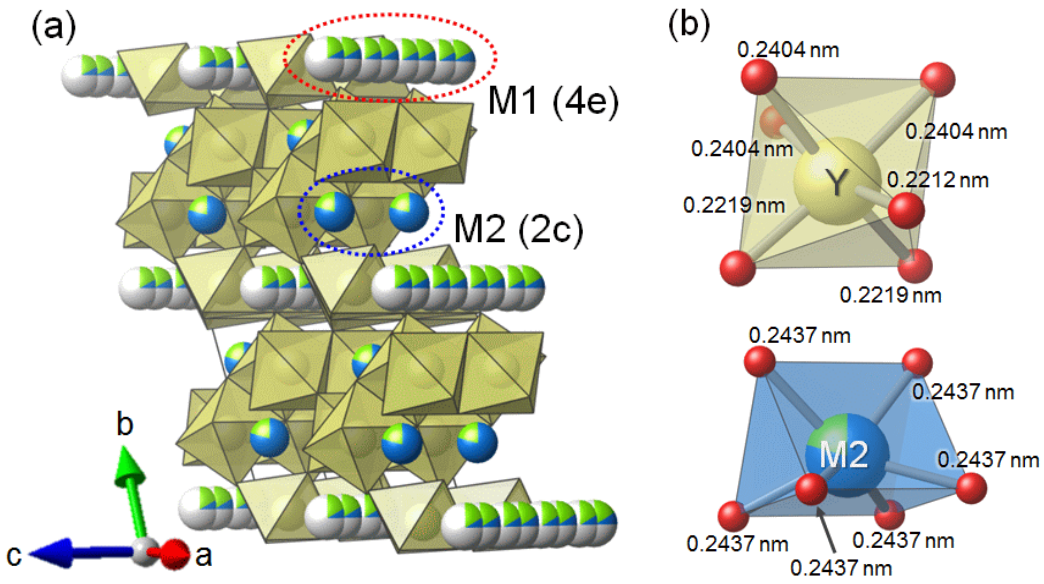

Fig. 5.3 (a)The final refined crystal structure of the $BaCa_2(Y_{0.998}Ce_{0.002})_6O_{12}$. (b) Coordination environment of the YO_6 octahedra and $M2O_6$ triangular prism polyhedra in the $BaCa_2(Y_{0.998}Ce_{0.002})_6O_{12}$.

located in the direction along to *c*-axis at the chinks of YO_6 framework. Figure 5.3 (b) presents the coordination environments of the YO_6 octahedra and $M2O_6$ trigonal prism polyhedra in the $BaCa_2(Y_{0.998}Ce_{0.002})_6O_{12}$ lattice, and the bond distance of these polyhedra are listed in Table 5.2. The average bond distance of YO_6 octahedra in the $BaCa_2(Y_{0.998}Ce_{0.002})_6O_{12}$ was found to be 0.2284 nm, which is shorter than that of $M2O_6$ trigonal prism (0.2212 nm). Additionally, the lattice volume of $BaCa_2(Y_{1-x}Ce_x)_6O_{12}$ ($0.001 \leq x \leq 0.020$) phosphors decreased with increase the Ce^{3+} concentration until x=0.003~0.005, and then increased with increase the Ce^{3+}

Table 5.2 Selected bond distances of $BaCa_2(Y_{0.998}Ce_{0.002})_6O_{12}$ at room temperature.

$BaCa_2(Y_{0.998}Ce_{0.002})_6O_{12}$			
bonding	bond distance (nm)	bonding	bond distance (nm)
(M2/Ce)-O2	0.2436(4)	(Y1/Ce)-O1	0.2212(8)
(M2/Ce)-O2	0.2436(4)	(Y1/Ce)-O1	0.2218(9)
(M2/Ce)-O2	0.2437(8)	(Y1/Ce)-O1	0.2218(9)
(M2/Ce)-O2	0.2437(8)	(Y1/Ce)-O2	0.2250(7)
(M2/Ce)-O2	0.2436(8)	(Y1/Ce)-O2	0.2403(9)
(M2/Ce)-O2	0.2436(8)	(Y1/Ce)-O2	0.2403(9)
Average	0.2436	Average	0.2284

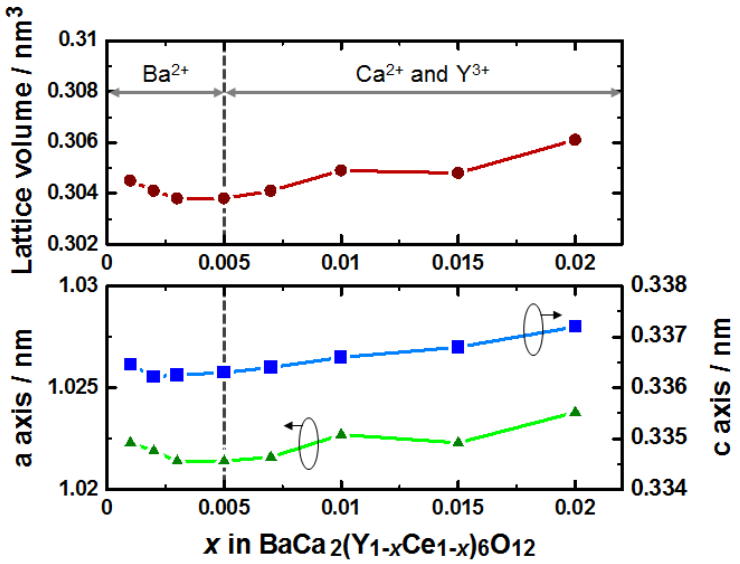

Fig. 5.4 The lattice volume and axis parameters dependence on the Ce^{3+} concentration in the $BaCa_2(Y_{1-x}Ce_x)_6O_{12}$ ($0.001 \le x \le 0.020$) lattice.

concentration, as shown in Fig. 5.4. This result indicates that the Ce^{3+} ion was preferentially doped into the M1 site until x=0.003~0.005, because the ionic radius of these cations, which is six coordination with surrounding anions, are in the following relationship; Ba^{2+} (0.135 nm) > Ce^{3+} (0.101 nm) > Ca^{2+} (0.100 nm) > Y^{3+} (0.0900 nm)[61].

Photoluminescence and photoluminescence excitation spectra of the $BaCa_2(Y_{0.998}Ce_{0.002})_6O_{12}$ phosphor prepared by the melt synthesis method using the arc imaging furnace are presented in the Fig. 5.5. The excitation spectrum consisted of the two absorption bands on a weak UV-light region and a strong blue-light region from 300 to 380 nm and from 400 to 500 nm peaked at 460 nm, respectively, which could be attributed to the spin-arrowed transition from 4f to 5d of Ce^{3+} ion.[6] Under the blue-light irradiation at 460 nm, the $BaCa_2(Y_{0.998}Ce_{0.002})_6O_{12}$ phosphor exhibits a reddish-yellow emission with a broad asymmetric spectrum from 500 to 750 nm

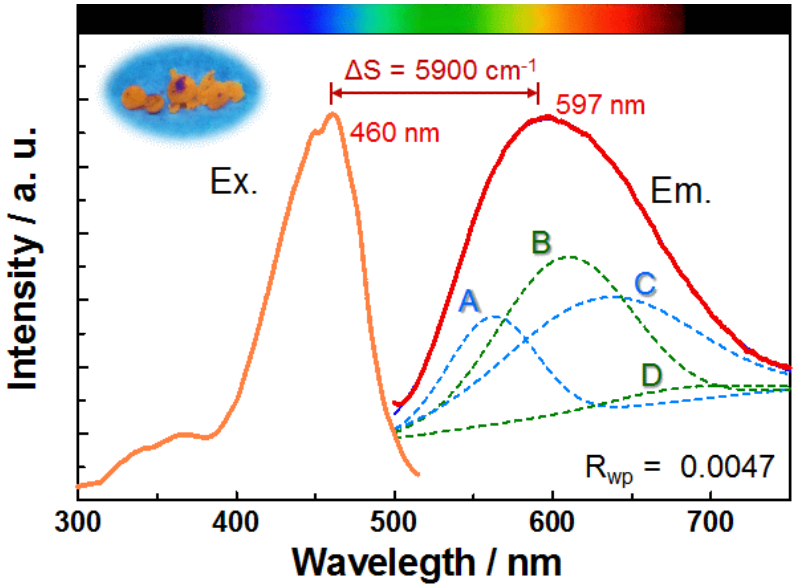

Fig. 5.5 Excitation and emission spectra of $BaCa_2(Y_{0.998}Ce_{0.002})_6O_{12}$ phosphor. Peak deconvolution of excitation and emission bands are indicated as dotted lines. Inset shows the emission photograph under the UV-light irradiation at 365 nm of the phosphor.

centering at 597 nm, which is corresponding to the 5d-4f transition of Ce^{3+}. This asymmetric emission spectrum could be fitted to four Gaussian bands centered at 562 nm (band A; 17,800 cm^{-1}), 608 nm (band B; 16,450 cm^{-1}), 632 nm (band C; 15,830 cm^{-1}) and 680 nm (band D; 14,700 cm^{-1}), respectively. The ground state of Ce^{3+} ion split by a spin-orbit interaction for $^2F_{7/2}$ and $^2F_{5/2}$ levels, and the theoretical energy gap of these ground levels is ~2,000 cm^{-1}.[56,43,101, 141] In the emission spectra of the $BaCa_2(Y_{0.998}Ce_{0.002})_6O_{12}$ phosphor, the energy deference of the A and C (ΔA-C) bands, and the B and D (ΔB-D) bands were found to be 1,970 and 1,740 cm^{-1}, respectively, which is similar to the theoretical value for $^2F_{7/2}$ and $^2F_{5/2}$ levels of Ce^{3+} (~2,000 cm^{-1}).[56,101,141] This result indicate that the Ce^{3+} ion in the $BaCa_2(Y_{0.998}Ce_{0.002})_6O_{12}$ lattice were incorporated into the two deferent crystallographic sites. In order to the determination of the Ce^{3+} doping

crystallographic site in the host lattice, the emission peak of Ce^{3+} can be estimated using following empirical equation given by Van Uitert:[31]

$$E = Q\left[1 - \left(\frac{V}{4}\right)^{1/V} 10^{-(n\,ea\,r)/80}\right] \qquad \text{Eq. 5.1}$$

where, E is the position in the energy of the 5d band edge for the Ce^{3+} ion, Q is the energy position of the lowest 5d band edge for the free ion (50,000 cm^{-1}), V is the valence state of the active cation Ce^{3+}, n represents the number of anions in the immediate shell about the activator, ea is the electron affinity of the anion atoms dependent on the anion complex type, and r is the ionic radius of the host cation replaced by Ce^{3+}. According to the eq. 5.1, the calculated emission band positions of Ce^{3+} at the different coordination of $M1O_9$, $M2O_6$ and YO_6 were found to be 415, 617 and 685 nm, respectively. Since the emission spectrum is observed by under the blue-light excitation at 460 nm, the blue emission (415 nm) due to Ce^{3+}, which replaces to $M1O_9$, could not be observed at the measurement condition. The emission bands of A and C of 562 and 632 nm were attributed to the Ce^{3+} replaced in the $M2O_6$, and those of B and D of 608 and 680 nm were corresponding to the Ce^{3+} replaced in the YO_6, because these observed emission band positions were similar to the calculated values replaced in $M2O_6$ (632 nm) and YO_6 (680 nm), respectively. Figure 5.6 present the excitation and emission spectra of the $BaCa_2(Y_{1-x}Ce_x)_6O_{12}$ ($0.001 \leq x \leq 0.020$) phosphors with various Ce^{3+} concentrations. All phosphor samples exhibit the similar spectra to the $BaCa_2(Y_{0.998}Ce_{0.002})_6O_{12}$ phosphor, which indicate that the photoluminescence of all samples are due to the 5d-4f transitions of Ce^{3+} incorporated in two different site, $M2O_6$ and YO_6 in the host lattice. The luminescence intensity increased with the amount of Ce^{3+} until it reached a maximum at x = 0.002 in $BaCa_2(Y_{1-x}Ce_x)_6O_{12}$, and then decreased due to the

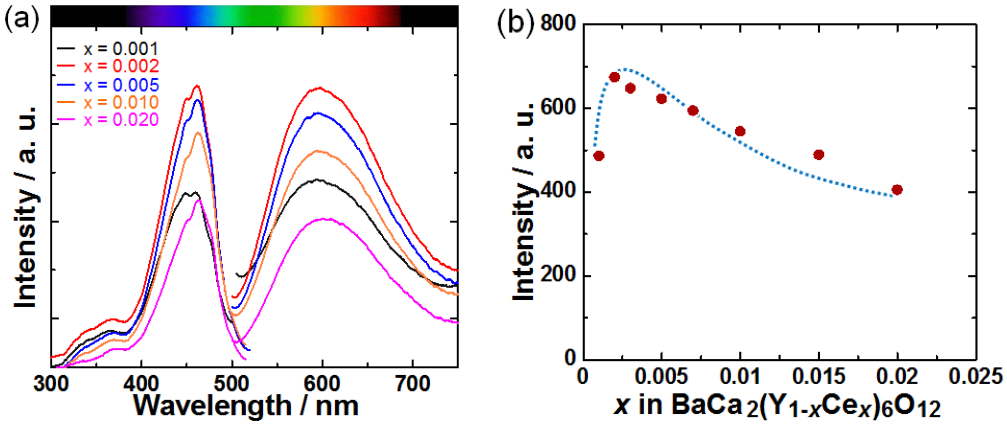

Fig. 5.6 Dependence on (a) the excitation and emission spectra and (b) emission intensity of Ce^{3+} concentration in the $BaCa_2(Y_{1-x}Ce_x)_6O_{12}$ ($0.001 \leq x \leq 0.020$) phosphors prepared by a melt synthesis technique using the arc imaging furnace.

concentration quenching effect (as see the Fig. 5.6 (b)).[43,142] Therefore, the optimal Ce^{3+} concentration in $BaCa_2(Y_{1-x}Ce_x)_6O_{12}$ was found to be 0.2 mol%.

In order to more understand the luminescence mechanism, the centroid shift, crystal field splitting and Stokes shift of the $BaCa_2(Y_{0.998}Ce_{0.002})_6O_{12}$ phosphor have been estimated from equations by P. Dorenbos. The total energy shift from the lowest 5d level edge can be described as[69,]

$$D(A) = 49{,}340\ \mathrm{cm}^{-1} - E(Ce, A). \qquad \text{Eq. 5.2}$$

Here, $E(Ce, A)$ is an excited 5d level edge estimated from the excitation spectrum, and a red shift $D(A)$ is containing the centroid shift and crystal field splitting. The red shift of the Ce^{3+} due to incorporating each sites in $BaCa_2(Y_{0.998}Ce_{0.002})_6O_{12}$ phosphor were same values because of the having same excitation edge, which is found to be 21,700 cm^{-1}. The centroid shifts, ε_c were estimated by following equation:[105,109,110]

$$\varepsilon_c = 17{,}900 \times \sum_{i=1}^{N} \frac{\alpha_{sp}^{i}}{(R_i - 0.6\Delta R)^6} \qquad \text{Eq. 5.3}$$

where, R_i represents the bond distance for the Ce^{3+}-O^{2-} ions in the host lattice, ΔR is the deference in the ionic radii for Ce^{3+} and the host cation replaced by Ce^{3+} (Y^{3+} and Ca^{2+}), and N is the number of anions coordinated with Ce^{3+} ion. The α_{sp}^{i} is the spectroscopic polarizability, which is described as[105,109,110]

$$\alpha_{sp}^{i} = 0.33 + \frac{4.8}{{\chi_{av}}^2}. \qquad \text{Eq. 5.4}$$

χ_{av} is the weighted average of the cation electronegativity in a given host lattice. From eq. 5.3 and 5.4, the centroid shifts of the Ce^{3+} replacing Ca^{2+} and Y^{3+} sites were estimated to be 16,500 and 21,400 cm^{-1}, respectively. The calculated centroid shift values of were comparable to that of simple oxide and transition metal oxide hosts, such as CaO:Ce^{3+} (20,500 cm^{-1}), $CaZrO_3$ (17,200 cm^{-1}) and *etc*.[106] The centroid shift mostly increases with the decrease electronegativity of the cation central to the complex.[106] The $BaCa_2Y_6O_{12}$ host consists of lower valence cations with lower electronegativity, which results in the large centroid shift. Dorenbos concluded that the crystal field splitting ε_{cfs} of 5d levels were affected by the Ce^{3+} coordinated polyhedron size and shape. The octahedral YO_6 can be estimated by the following equation:[105,143]

$$\varepsilon_{cfs} = \beta_{poly}^{Q} {R_{av}}^2. \qquad \text{Eq. 5.5}$$

Here, β_{poly}^{Q} presents a constant depending the shape and coordination number, in which the octahedral β_{octa} is 1.35×10^9 pm^2cm^{-1} for Ce^{3+}. R_{av} is an average bond distance of the polyhedral, which is defined as[143]

$$R_{av} = \frac{1}{N}\sum_{i=1}^{N}(R_i - 0.6\Delta R). \qquad \text{Eq. 5.6}$$

R_i are the bond distance of Ce^{3+}-O^{2-} to the N coordinating anions; ΔR is deference of ionic radii for central cation and Ce^{3+}. The ε_{cfs} of the octahedral YO_6 could be

found to be 24,400 cm^{-1}. On the other hands, the ε_{cfs} of the trigonal prismic $M2O_6$ could be calculated to be 22,600 cm^{-1}. However, the actual ε_{cfs} of trigonal prism are smaller than the calculated values, which is difficult to calculate the actual ε_{cfs} of trigonal prismic $M2O_6$ in $BaCa_2Y_6O_{12}$.[105] The Stokes shift ΔS, which is the energy gap of the excitation and emission bands of the luminescence due to the two deferent sites can be determined to be 5,900 cm^{-1} for the replacing the Ca^{2+} ion and 7,000 cm^{-1} for the replacing the Y^{3+} ion, respectively. The Stokes shifts of Ce^{3+} ion in the $BaCa_2Y_6O_{12}$ host represented larger values compared to that of the conventional yellow emitting Ce^{3+} activated complexed-oxide phosphors, such as the γ-Ca_2SiO_4:Ce^{3+} (4,560 cm^{-1}),[68] YAG:Ce^{3+} (~2,700 cm^{-1})[92,145] and $Lu_2CaMg_2Si_3O_{12}$:Ce (2,550 cm^{-1})[53] phosphors, and are comparable to that of the Ce^{3+} activated simple and transition metal oxide phosphors, such as SrY_2O_4:Ce^{3+} (7,332 cm^{-1})[111,144] and $LaLuO_3$:Ce^{3+} (7,962 cm^{-1}),[111] which may imply a strong electron-lattice interaction for the Ce^{3+} centers.[145] A larger Stokes shift mostly indicates a strong coupling of the 5d electrons with lattice phonons, which results in a broader emission band of Ce^{3+}.[47] Actually, the value of full width at half maximum (FWHM) for the emission spectrum of $BaCa_2(Y_{0.998}Ce_{0.002})_6O_{12}$ were found to be 3,660 cm^{-1} (134 nm), and were larger than that of a smaller Stokes shift phosphor, ~3500 cm^{-1} (~100 nm; as the estimated by us) for $CaSc_2O_4$:Ce^{3+} with Stokes shift of 2,561 cm^{-1}.[76]

The thermal quenching property of the $BaCa_2(Y_{0.998}Ce_{0.002})_6O_{12}$ phosphor was investigated, and the recorded temperature dependence of the emission intensity for in $BaCa_2(Y_{0.998}Ce_{0.002})_6O_{12}$ phosphor normalized with respect to the value at 25°C is presented in Fig. 5.7. With increasing the temperature up to 150°C, the emission intensity of the $BaCa_2(Y_{0.998}Ce_{0.002})_6O_{12}$ phosphor decreases to 4.8% of the initial

value of 30°C, which is quite large thermal quenching. Furthermore, the activation energy, E_a was calculated by following Arrhenius equation for more deep understanding of the thermal quenching properties:[146]

$$I(T) = \frac{I_0}{1+A\exp(-E_a/kT)} \qquad \text{Eq. 5.7}$$

where, E_a is the activation energy for thermal quenching, I_0 and $I(T)$ represent the luminescence intensity at the temperature of initial and T, respectively, A is a constant, k is a Boltzmann constant and T is a recorded temperature. A plot of ln[(I_0/I(T))-1] vs. $1/kT$ of the thermal dependence on luminescence intensity of $BaCa_2(Y_{0.998}Ce_{0.002})_6O_{12}$ phosphor is shown in the inset of Fig. 5.7. Using Arrhenius equation, the activation energy (E_a) of the thermal quenching of the $BaCa_2(Y_{0.998}Ce_{0.002})_6O_{12}$ phosphor could be found to be 0.358 eV, which is significantly higher value than that of $CaSc_2O_4:Ce^{3+}$ phosphor (E_a =0.294 eV;

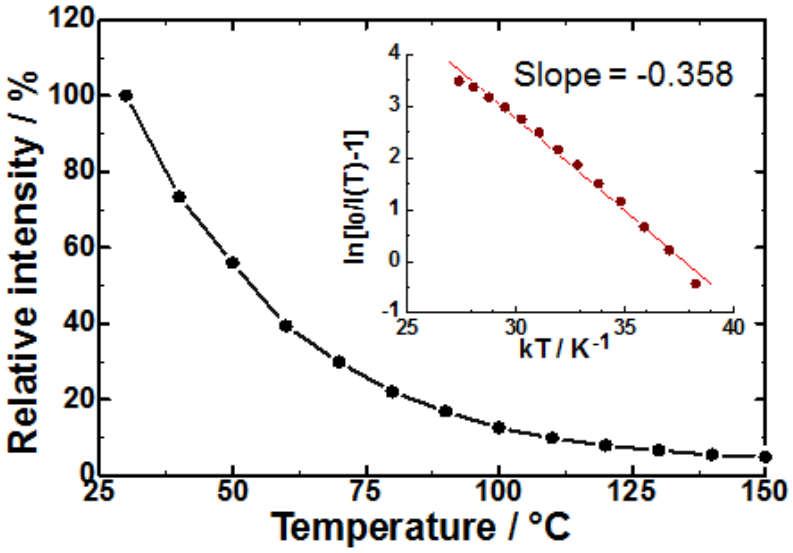

Fig. 5.7 Temperature dependence of the emission intensity for $BaCa_2(Y_{0.998}Ce_{0.002})_6O_{12}$ phosphor under the blue-light excitation at 460 nm. Inset shows the activation energy ΔE of the $BaCa_2(Y_{0.998}Ce_{0.002})_6O_{12}$ phosphor.

estimated by us) with a small Stokes shift ΔS (2,561 cm^{-1}).[147] It is well-known that the larger stokes shift leads to the thermal quenching at lower temperatures.[123] Therefore, the non-excellent thermal stability of $BaCa_2(Y_{0.998}Ce_{0.002})_6O_{12}$ phosphor is reasonable.[27]

5.4 Summary

In this chapter, new red-emitting oxide phosphor, Ce^{3+}-activated $BaCa_2Y_6O_{12}$, have been discovered by the melt synthesis method using an arc imaging furnace. The crystal structure of $BaCa_2(Y_{0.998}Ce_{0.002})_6O_{12}$ phosphor were analyzed by a Rietveld refinement. As the results, the $BaCa_2(Y_{0.998}Ce_{0.002})_6O_{12}$ lattice has a hexagonal system with a space group of $P6_3/m$, and it was revealed that the atomic position sites of the alkali earth ion are occupied by the disordering Ba^{2+}/Ca^{2+} of 0.15/0.10 for M1 site (4e site) and 0.20/0.80 for M2 site (2c site), respectively. The Ce^{3+} ion was preferentially incorporated into the M1 site, because the lattice volume of the $BaCa_2(Y_{1-x}Ce_x)_6O_{12}$ ($0.001 \leq x \leq 0.020$) phosphors was decrease until x = 0.003~0.005, and then it was increased. Under the blue-light excitation at 460 nm, the phosphors exhibit the broad reddish-yellow emission spectrum including the four Gaussian function peaked at 562 nm (band A), 608 nm (band B), 632 nm (band C) and 680 nm (band D), respectively, which are due to the 5d-4f transitions of Ce^{3+}. It could be estimated that the decomposed emission bands A and C were attributed to the Ce^{3+} replaced in the M2 site, and bands B and D were attributed to the Ce^{3+} replaced in the Y site. In addition, the 5d levels of the centroid shift and crystal field splitting of the Ce^{3+} replacing Y^{3+} site were larger than that of the Ce^{3+} replacing M2 site and that of the simple oxide phosphors. The larger Stokes shift (~7,000 cm^{-1}) affected to the low thermal stability of 4.8% at 150°C of the initial value of 25°C. We concluded that the selection of the host material is important to obtain the red emission in the oxide lattice, and the simple oxides are suitable as the host material.

Chapter 6

Efficient Red Emission of Blue-Light Excitable New Structure Type $NaMgPO_4:Eu^{2+}$ Phosphor

6.1 Introduction

Although there are many candidates for new advanced phosphor materials for use in the white-LEDs, we have focused on sodium magnesium orthophosphate, $NaMgPO_4$, as a host material for the phosphors to realize a novel red-emitting phosphor with high luminescence efficiency. The orthophosphates with the general formula $ABPO_4$ (A: monovalent cations and B: divalent cations) have been investigated as host material for phosphors because of excellent thermal stability and the tetrahedral rigid three-dimensional matrix of the phosphates is thought to be ideal for charge stabilization.[148-156] In particular, Eu^{2+}-doped orthophosphate phosphors can show good luminescence efficiency as phosphor for use in white-LEDs.[149-151,155,156] These phosphors show strong broad optical absorption at violet region and exhibit strong blue- or green emission under violet irradiation. However, there is no report yet on the efficient red-emitting phosphor based on the orthophosphate and some other phosphate materials under blue light irradiation.

In this chapter, a novel red-emitting olivine-type $NaMgPO_4:Eu^{2+}$ phosphor was synthesized for the first time by melt synthesis technique using arc-imaging furnace, and their crystal structure and photoluminescence properties were characterized. In addition, it has been demonstrated in our previous studies that this synthesis method is suitable for synthesizing phosphors with high luminescence efficiency.[136,157,158]

6.2 Experimental section

Synthesis of materials. A mixture of Na_2CO_3, MgO, $NH_4H_2PO_4$, and Eu_2O_3 was mixed using a mortar with acetone for obtaining a homogeneous chemical mixture, in which the Eu^{2+} content was adjusted between 1.0 mol% and 9.0 mol%, and then the homogeneous mixture was calcined at 400 °C for 4h in air. After calcination, the sample was reground in a mortar and placed on a copper hearth, and then melted in a flow of 5%H_2-95%Ar gas using arc-imaging furnace. By the radiation of a 6 kW-Xe lamp, the sample was melted into 3-5 mm spherical globule on the copper hearth, then rapidly cooled by dosing a shutter to cut-off the radiation. It took generally 5-15 sec. from the molten state at around 2000 °C to reach the solid state with a dark color at around 600 °C after closing the shutter. Therefore, the cooling rate was estimated to be more than 100 °C / sec.

Materials characterization. The sample was characterized by X-ray powder diffraction (XRD; Mac Science Ltd. MX-Labo) analysis and the crystal structure analysis was carried out via Rietveld refinement of powder XRD data using the program "RIETAN-FP".[63] The photoluminescence emission (PL) and excitation (PLE) spectra were measured at room temperature with a spectrofluorometer (Jasco Corp. FP-6500/6600), where the emission spectrum was obtained for excitation at 450 nm, and excitation spectrum was obtained for emission at 628 nm. The Commission International de I'Eclairage (CIE) chromaticity coordinate data for the phosphor were measured at room temperature with a luminescence colorimeter (Hamamatsu C7473-36 PMA-11).

6.3 Results and discussion

Although X-ray powder diffraction (XRD) pattern of a $NaMgPO_4:Eu^{2+}$ phosphor prepared in this study was not identical to a single phase of well-known glaserite-type $NaMgPO_4$ structure,[159] impurity phase corresponding to the starting materials was not observed in the pattern. To investigate the crystal structure, the Rietveld refinement analysis is carried out on the $(Na_{0.975}Eu_{0.025})MgPO_4$ prepared in this study, and the result is shown in Fig. 6.1. The obtained XRD pattern of $(Na_{0.975}Eu_{0.025})MgPO_4$ phosphor is well indexed to the single phase of orthorhombic olivine-type $LiMgPO_4$ structure (ICSD #201138).[160] This indicates that the $NaMgPO_4:Eu^{2+}$ phosphor has an orthorhombic olivine-type structure with a space group of *Pnma*, which is built out of PO_4 tetrahedra and MgO_6 octahedra connected to form a three-dimensional framework enclosing tunnels along b-axis occupied by

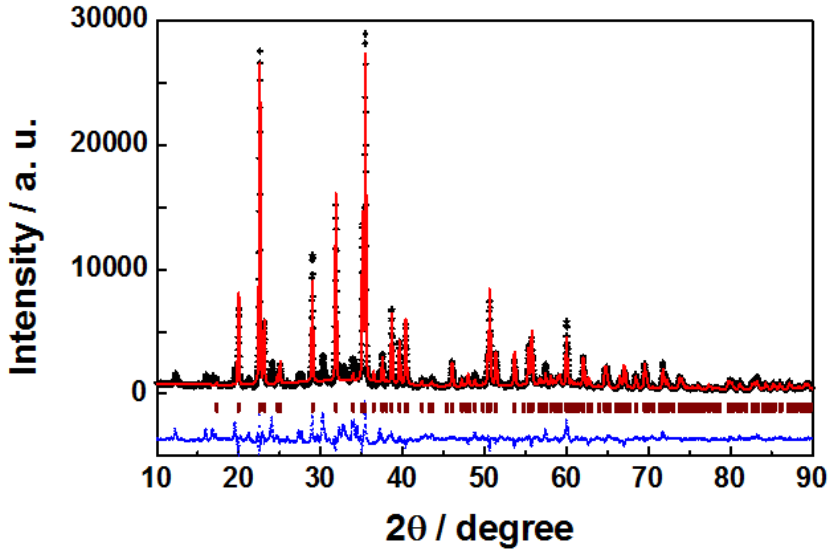

Fig. 6.1 Observed (black plus) and calculated (red line) X-ray powder diffraction data of $(Na_{0.975}Eu_{0.025})MgPO_4$ phosphor prepared in this study as well as the difference profile (blue bottom line) between them. Bragg reflection peak positions are shown as vertical bars.

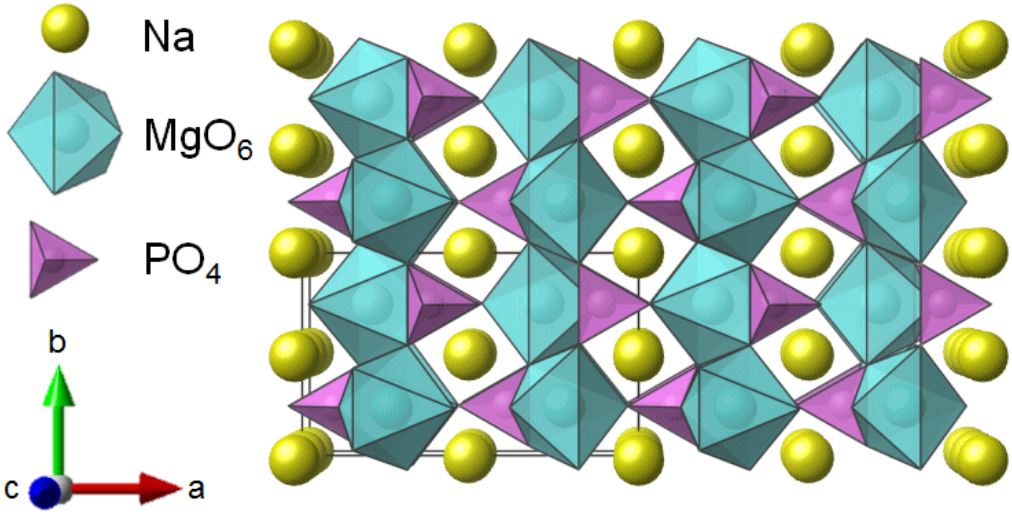

Fig. 6.2 Crystal structure of orthorhombic olivine-type $NaMgPO_4$.

Na^+ ions as illustrated in Fig. 6.2. Na^+ ion has an ionic radius of 0.102 nm for 6 coordination, while Mg^{2+} has an ionic radius of 0.072 nm for 6 coordination.[61] Therefore, in the case of present phosphors, the doping Eu^{2+} ions preferably occupy the Na^+ site in the host lattice, because the ionic radius of Eu^{2+} (0.117 nm for 6 coordination)[61] is similar to that of Na^+ (0.102 nm) which is much larger than that of the Mg^{2+} ion (0.072 nm).

Figure 6.3 presents the photoluminescence excitation and emission spectra of a $(Na_{0.975}Eu_{0.025})MgPO_4$ phosphor. The excitation spectrum is consisted of broad band covering the region from the UV to visible light part, which indicates that the phosphor is very suitable for a color converter using any excitation wavelength as the primary light source. The emission spectrum exhibit a broad red emission band centering at 628 nm, which corresponded to the allowed transition from $4f^65d^1$ to $4f^7$ of Eu^{2+}, under excitation wavelength at 450 nm, and no red line emissions from Eu^{3+} are observed even in a phosphorescence mode. Although a number of the Eu^{2+}-doped orthophosphate phosphors have been reported, which shows strong blue- or

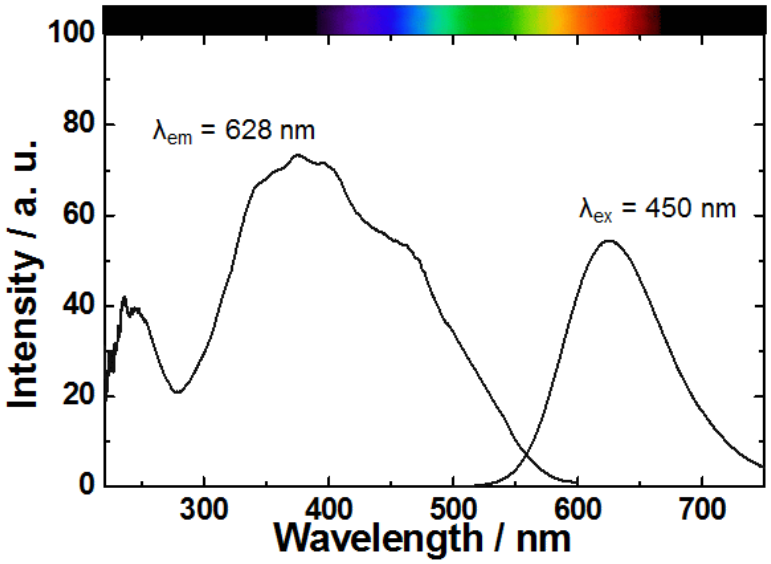

Fig. 6.3 Photoluminescence excitation (PLE) and emission (PL) spectra of $(Na_{0.975}Eu_{0.025})MgPO_4$ phosphor.

green-emission under near UV irradiation,[149-151,155,156] there is no report on the red-emitting phosphor under blue light irradiation. In the present $NaMgPO_4:Eu^{2+}$ phosphor, on the contrary, a strong red emission was observed under blue light irradiation, and this is the first time reported in the phosphors based on phosphates materials.

Figure 6.4 shows the dependence of the emission peak intensity on the Eu^{2+} concentration in the $(Na_{1-x}Eu_x)MgPO_4$ ($0.01 \leq x \leq 0.09$) phosphors. The emission peak intensity increased with the amount of Eu^{2+} until it reached a maximum at x = 0.025 in the $(Na_{1-x}Eu_x)MgPO_4$ ($0.01 \leq x \leq 0.09$) phosphors, and then decreased probably due to concentration quenching. The internal quantum efficiency of the $(Na_{0.975}Eu_{0.025})MgPO_4$ phosphor at the excitation wavelength of 450 nm was 81%. In addition, the CIE chromaticity coordinate values for the $(Na_{0.975}Eu_{0.025})MgPO_4$ phosphor were x = 0.60 and y = 0.38 under blue light irradiation. The x and y values

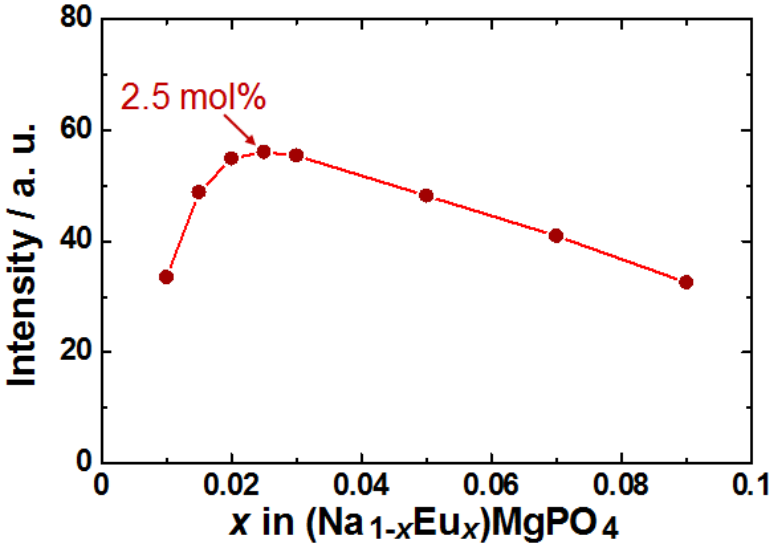

Fig. 6.4 Dependence of the emission peak intensity on the Eu^{2+} concentration in the $(Na_{1-x}Eu_x)MgPO_4$ ($0.01 \leq x \leq 0.1$) phosphors.

of this phosphor are very good for a red-emitting phosphor and are comparable to those of the conventional red-emitting $CaAlSiN_3:Eu^{2+}$ (x = 0.67, y = 0.33) and $Sr_2Si_5N_8:Eu^{2+}$ (x = 0.64, y = 0.36) phosphors.[26,161]

In the white-LEDs application, the temperature dependence of phosphor is important because it has great influence on the light output and color-rendering index. Figure 6.5 (a) presents the temperature-dependent emission spectra of the $(Na_{0.975}Eu_{0.025})MgPO_4$ under excitation at 450 nm. The emission peak wavelength of $(Na_{0.975}Eu_{0.025})MgPO_4$ phosphor shifts to the shorter wavelength (high energy) side with increasing the temperature. It should be considered that thermally activated phonon-assisted tunneling from the excited states of the low-energy emission band to the excited states of high-energy emission band in the configuration coordinate diagram occurs.[162-164] At low temperature, the low-energy emission is dominant. As the temperature increases, the electron population of Eu^{2+} in the upper vibration

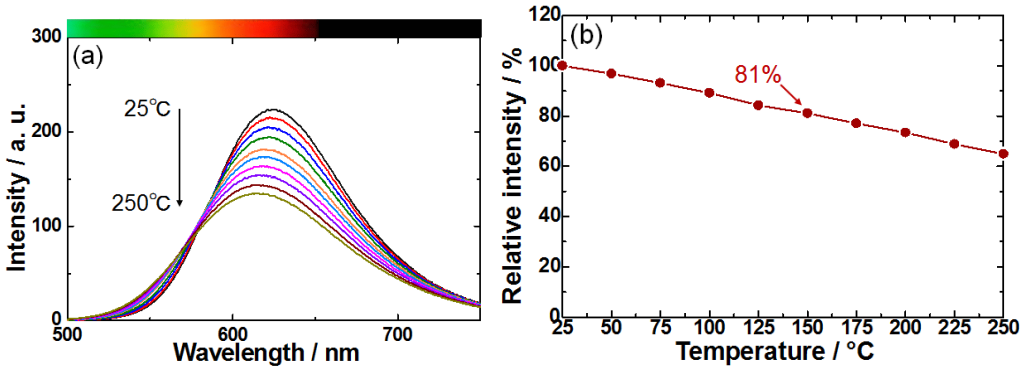

Fig. 6.5 The temperature dependence of the emission spectra (a) and the emission intensity (b) of the $(Na_{0.975}Eu_{0.025})MgPO_4$ phosphor under excitation wavelength at 450 nm.

level of the excited state becomes dominating under phonon assistance, from which radiative transition happens. Therefore, the emission peak wavelength of the Eu^{2+} $4f^65d^1 \rightarrow 4f^7$ transition shows the blue shift with an increase in the temperature. In addition, it is also possible that the expansion of the host lattice with temperature increase causes a reduction in the crystal field splitting, leading to a higher energy for the emission.

Furthermore, it is well known that the emission intensity generally decreases with an increase in the temperature due to thermal quenching. Figure 6.5 (b) shows temperature dependence of the emission intensity of the $(Na_{0.975}Eu_{0.025})MgPO_4$ phosphors normalized with respect to the value at 25 °C. It can be seen that the $(Na_{0.975}Eu_{0.025})MgPO_4$ phosphor has an excellent thermal stability on the temperature quenching effect. With increasing the temperature up to 150 °C, the emission intensity of the $(Na_{0.975}Eu_{0.025})MgPO_4$ phosphor decreases to 86 % of the initial value at 25 °C. These results indicate that the $NaMgPO_4:Eu^{2+}$ phosphors are expected to find application as red-emitting phosphor for use in white-LEDs, although emission peak shift to a shorter wavelength was observed with an increase in the temperature.

6.4 Summary

In summary, novel red-emitting $NaMgPO_4:Eu^{2+}$ phosphors were synthesized for the first time by the melt synthesis technique using arc-imaging furnace. These phosphors obtained in the present study adopt the orthorhombic olivine-type $NaMgPO_4$ structure with high crystallinity. The excitation spectra of $NaMgPO_4:Eu^{2+}$ are consisted of broad band covering the region from the UV to visible light part, and the photoluminescent spectra with excitation at 450 nm showed red emission from $4f^65d^1$-$4f^7$ transition of Eu^{2+}. By the optimization of the Eu^{2+} concentration, highest emission peak intensity was obtained for $(Na_{0.975}Eu_{0.025})MgPO_4$, and the internal quantum efficiency of this phosphor at the excitation wavelength of 450 nm was 81%. Furthermore, the $NaMgPO_4:Eu^{2+}$ phosphor has an excellent thermal stability on the temperature quenching effect. To the best of our knowledge, this is the first report of practical red-emitting phosphate phosphors for the Blue LED based white-LEDs.

Chapter 7

Synthesis of Blue-emitting $(K_{1-x}Na_x)Mg_4(PO_4)_3:Eu^{2+}$ Phosphors

7.1 Introduction

From chapter 2 to chapter 6, we focused on the oxide host materials having the high symmetric octahedral or 7-coordination polyhedral in order to obtain the longer wavelength emission. On the other hands, in this chapter, a novel oxide phosphors was synthesized in order to observe a luminescence of Eu^{2+} located at the low symmetric loose site by the synthesis of the novel phosphor.

A potassium magnesium phosphate, $MMg_4(PO_4)_3$ (M = alkali metal), was focused on as a host material of phosphor to realize an Eu^{2+}-doped blue emitting phosphor with high luminescence efficiency. The crystalline form of alkali metal magnesium phosphate has an orthorhombic structure with a space group of *Pnnm*, which is built out of the PO_4 tetrahedra, MgO_6 octahedra, and MgO_5 polyhedra connected to form a three-dimensional framework enclosing tunnels along the *b*-axis occupied by M^+ ions,[165-167] as shown in Fig. 7.1 (a). It is well known that the tetrahedral rigid three-dimensional matrix of the phosphates is thought to be ideal for charge stabilization.[148-150,154,164] The potassium ion coordinates with eight oxygens, formed a low symmetric polyhedral, as shown in Fig. 7.1 (b). In addition, the phosphate materials have high thermal and chemical stabilities, which are advantageous for obtaining phosphor particles with high crystallinity. The photoluminescence properties of $NaMg_4(PO_4)_3:Eu^{2+}$ phosphors have already been reported by Lan et al. to exhibit blue emission peaking at 424 nm due to the Eu^{2+} $4f^65d^1 \rightarrow 4f^7$ transition, and they succeeded in enhancing the emission intensity through Ce^{3+} co-doping due

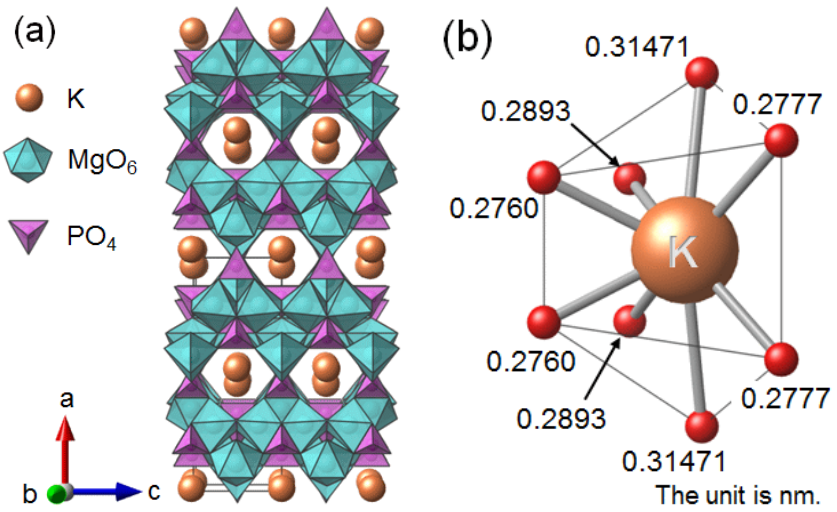

Fig. 7.1 (a) Crystal structure of $KMg_4(PO_4)_3$ and (b) the coordination environment of K site.

to the energy transfer from Ce^{3+} to Eu^{2+}.[170] In addition, they reported that the photoluminescence properties of $KMg_4(PO_4)_3:Eu^{2+}$ phosphors show blue emission peaking at 442 nm, and that the colorimetric purity of $KMg_4(PO_4)_3:Eu^{2+}$ phosphors is higher than that of $NaMg_4(PO_4)_3:Eu^{2+}$ phosphors.[171] The colorimetric purity of $KMg_4(PO_4)_3:Eu^{2+}$ phosphors, however, remains too low for use in optical devices as commercial phosphors. In addition, there has been no report focusing on the relative luminescent intensities in comparison with the commercially available phosphors under UV excitation.

In this chapter, therefore, the blue-emitting $KMg_4(PO_4)_3:Eu^{2+}$ phosphors were synthesized through the conventional solid-state reaction method, and the photoluminescence properties of the prepared phosphors were investigated in detail and were compared with those of the commercially available $BaMgAl_{10}O_{17}:Eu^{2+}$ phosphor. Furthermore, to further enhance the emission intensity of the $KMg_4(PO_4)_3:Eu^{2+}$ phosphors, some of the K^+ ions (ionic radius: 0.138 nm for

six-coordination)[61] in the host $KMg_4(PO_4)_3$ lattice were substituted with smaller Na^+ ions (ionic radius: 0.102 nm for six-coordination)[61] to enhance the crystal field strength around Eu^{2+} in the host lattice, and the emission band of the $KMg_4(PO_4)_3:Eu^{2+}$ phosphors can be shifted to a longer wavelength, which will improve the colorimetric purity of the $KMg_4(PO_4)_3:Eu^{2+}$ phosphors.

7.2 Experimental section

Synthesis of materials. A stoichiometric mixture of K_2CO_3, Na_2CO_3, Eu_2O_3, MgO, and $NH_4H_2PO_4$ was prepared using a mortar with acetone, for obtaining a homogeneous chemical mixture. The Eu^{2+} content was adjusted between 0.5 and 7 mol%, and the Na^+ content was varied from 0 to 50 mol%. The homogeneous mixture was calcined at 900°C for 12 h in a 5%H_2–95%N_2 gas flow for the reduction of Eu^{3+} to Eu^{2+}.

Materials characterization. The crystal structure of the samples was identified through X-ray powder diffraction (XRD; Mac Science Ltd MX-Labo) analysis. The morphology of the phosphor particles was characterized via scanning electron microscopy (SEM; JEOL JMS-5310LV). The size distribution and mean particle size were estimated by measuring the diameters of 100 particles from the SEM photographs. The emission (PL) and excitation (PLE) spectra were measured at room temperature with a spectrofluorometer (Jasco Corp. FP-6500/6600), where the emission spectrum was obtained for excitation at 254 nm, and excitation spectrum was obtained for emission at 450 nm. The relative emission intensities of the $KMg_4(PO_4)_3$:Eu^{2+} phosphors were estimated by comparing the emission peak intensity with that of the commercial blue-emitting $BaMgAl_{10}O_{17}$:Eu^{2+} phosphor (Tokyo Kagaku Kougyou Co., Ltd).

7.3 Results and discussion

The XRD patterns of $(K_{1-y}Eu_y)Mg_4(PO_4)_3$ ($0.005 \le y \le 0.07$) phosphors were in good agreement with a single phase of highly crystalline orthorhombic $KMg_4(PO_4)_3$ structure. In addition, these phosphors present the blue emission band centered at 450 nm under excitation at 254 nm due to the $4f^65d^1 \rightarrow 4f^7$ transition of Eu^{2+}. Figure 7.2 shows the emission intensity dependence on the Eu^{2+} concentration in the $(K_{1-y}Eu_y)Mg_4(PO_4)_3$ ($0.005 \le y \le 0.07$) phosphors. The emission intensity increases with the amount of Eu^{2+} until it reaches the maximum at $y = 0.01$ and then decreases due to concentration quenching. The maximum emission peak intensity was obtained for $(K_{0.99}Eu_{0.01})Mg_4(PO_4)_3$, where the emission peak intensity was 16% compared with that of the commercial blue-emitting $BaMgAl_{10}O_{17}:Eu^{2+}$ phosphor.

To enhance the emission intensity of the $(K_{0.99}Eu_{0.01})Mg_4(PO_4)_3$ phosphor, Na^+ was doped into the K^+ site in the $(K_{0.99}Eu_{0.01})Mg_4(PO_4)_3$ lattice. Figure 7.3 shows the

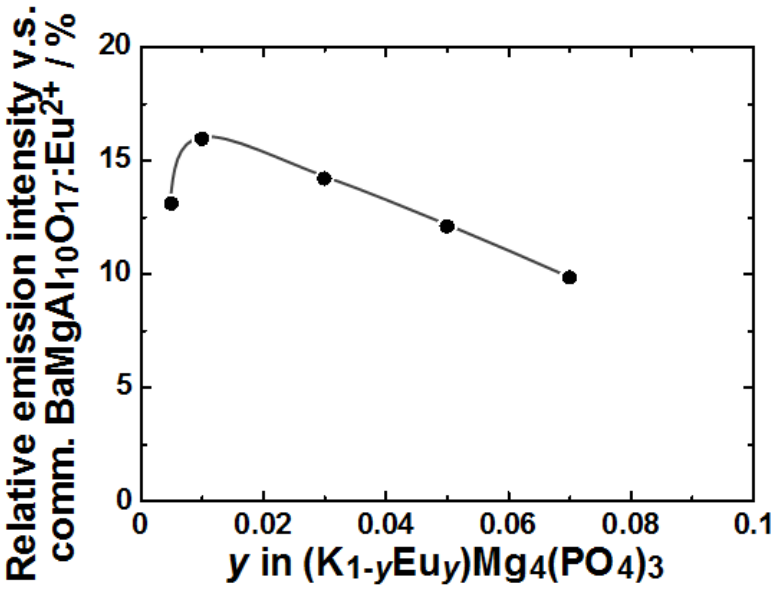

Fig. 7.2 Dependence of the emission intensity on the Eu^{2+} concentration in $(K_{1-y}Eu_y)Mg_4(PO_4)_3$ ($0.005 \le y \le 0.07$) phosphors.

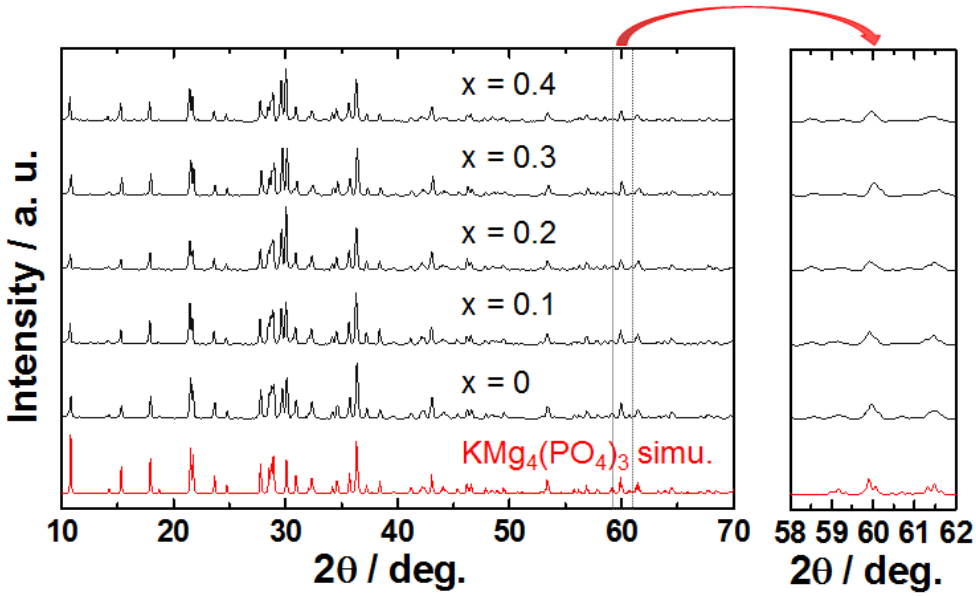

Fig. 7.3 XRD patterns of $(K_{0.99-x}Na_xEu_{0.01})Mg_4(PO_4)_3$ ($0 \le x \le 0.40$) phosphors.

XRD patterns of the $(K_{0.99-x}Na_xEu_{0.01})Mg_4(PO_4)_3$ ($0 \le x \le 0.40$) phosphors. The XRD patterns of all the samples were attributed to be a single phase of orthorhombic $KMg_4(PO_4)_3$ structure with high crystallinity, and there was no diffraction peak corresponding to any impurity in the patterns. In addition, a peak shift to a higher diffraction angle was observed with an increase in the Na+ content in the host $KMg_4(PO_4)_3$ lattice because the K^+ ions (ionic radius: 0.138 nm for six-coordination)[61] in the host lattice were partially substituted with small Na^+ ions (ionic radius: 0.102 nm for six-coordination)[61] to form solid solutions.

Figure 7.4 shows the excitation and emission spectra of $(K_{0.99-x}Na_xEu_{0.01})Mg_4(PO_4)_3$ (x = 0 and 0.35) phosphors. These phosphors exhibit a strong broadband emission, which is a well-known characteristic of Eu^{2+} blue emission, corresponding to the transition from $4f^65d^1$ to $4f^7$ of Eu^{2+}.[172] The position of the emission peak wavelength of the Eu^{2+} 5d–4f transition shifts to the longer wavelength (lower energy) side with increasing Na^+ content in the host $KMg_4(PO_4)_3$

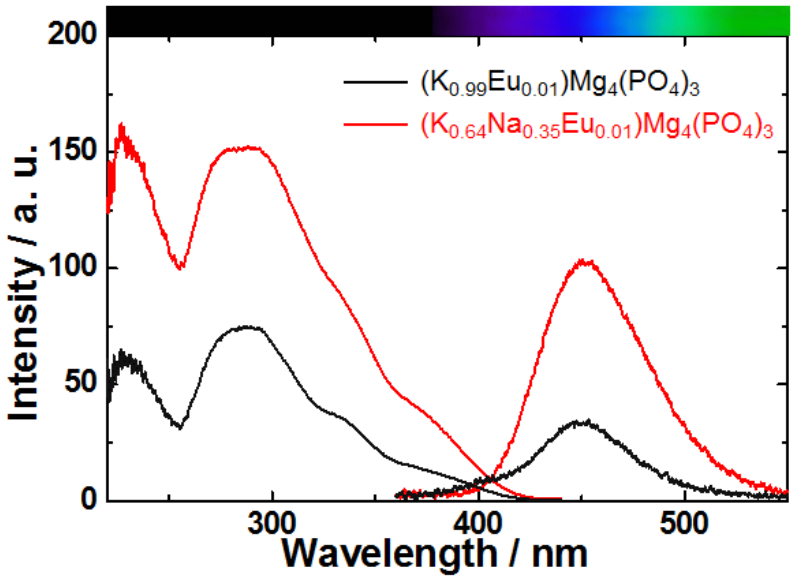

Fig. 7.4 Photoluminescence excitation and emission spectra of $(K_{0.99-x}Na_xEu_{0.01})Mg_4(PO_4)_3$ (x = 0 and 0.35) phosphors.

lattice, which can be attributed to the change in the crystal field strength around Eu^{2+} in the host lattice. The crystal field strength increases with increasing Na^+ substitution for K^+ in the host $KMg_4(PO_4)_3$ lattice because the average Eu^{2+}–O^{2-} bond becomes progressively shorter due to lattice shrinkage.

The dependence of the emission peak intensities on the Na^+ content in the $(K_{0.99-x}Na_xEu_{0.01})Mg_4(PO_4)_3$ ($0 \le x \le 0.40$) phosphors is shown in Fig. 7.5. The blue emission peak intensity was effectively increased by Na+ doping, and the emission reached the maximum intensity for x = 0.35 in the $(K_{0.99-x}Na_xEu_{0.01})Mg_4(PO_4)_3$ lattice. The increase in emission peak intensity with Na^+ doping can be explained by the increase in the crystallinity of the phosphor (Fig. 7.3), which usually results in the absorption enhancement of the excitation spectra (Fig. 7.4). The full-width at half-maximum (FWHM) of the XRD peaks in Fig. 7.3 was estimated for each $(K_{0.99-x}Na_xEu_{0.01})Mg_4(PO_4)_3$ ($0 \le x \le 0.40$) phosphors, and the results are summarized in Table 7.1. The FWHM correlates with the crystallinity of the phosphors, which

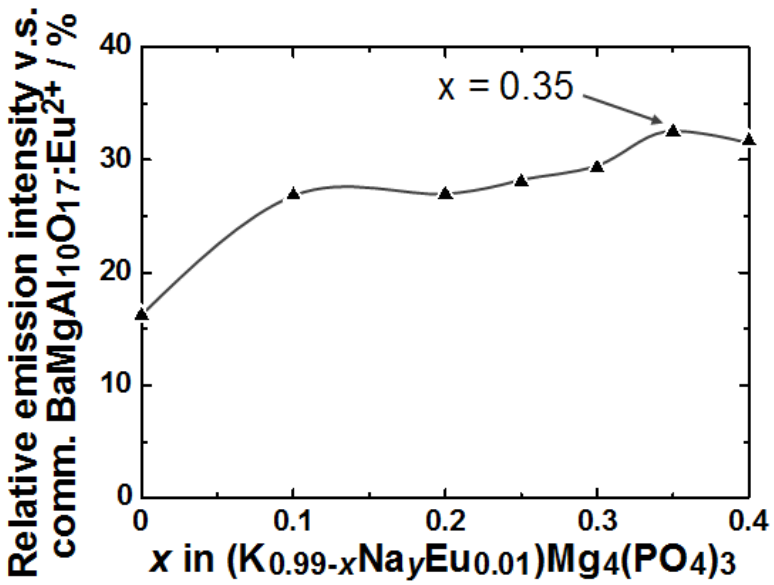

Fig. 7.5 Dependence of the emission peak intensity on the Na^+ content in the $(K_{0.99-x}Na_xEu_{0.01})Mg_4(PO_4)_3$ ($0 \le x \le 0.40$).

Table 7.1 FWHM of the (222) XRD peak for the $(K_{0.99-x}Na_xEu_{0.01})Mg_4(PO_4)_3$ ($0 \le x \le 0.40$) phosphors.

Samples	FWHM / degree
$x = 0$	0.2345
$x = 0.10$	0.2142
$x = 0.20$	0.2038
$x = 0.25$	0.1982
$x = 0.30$	0.1938
$x = 0.35$	0.1891
$x = 0.40$	0.2142

affects the photoluminescence properties. The FWHM of the $(K_{0.99-x}Na_xEu_{0.01})Mg_4(PO_4)_3$ ($0 \le x \le 0.40$) phosphors decreased with increasing Na+ content for $x \le 0.35$, which indicates that the crystallinity is increased by Na^+-doping into the host $KMg_4(PO_4)_3$ lattice. The FWHM was narrowest at $x = 0.35$, and the emission intensity reached the maximum while the relative emission intensity of $(K_{0.64}Na_{0.35}Eu_{0.01})Mg_4(PO_4)_3$ was 33% that of the commercial blue-emitting $BaMgAl_{10}O_{17}:Eu^{2+}$ phosphor. On the other hand, the FWHM for $x = 0.40$ became larger than that for $x = 0.35$, and the emission intensity tended to decrease with an

increase in Na^+ content beyond the optimum concentration. The decrease in emission intensity is probably due to the excessive distortion in the host $KMg_4(PO_4)_3$ lattice, which leads to luminescence quenching.

Figure 7.6 (a) shows the temperature dependence of the emission intensity of the $(K_{0.64}Na_{0.35}Eu_{0.01})Mg_4(PO_4)_3$ phosphor normalized with respect to the value at 25°C. The emission intensity of this phosphor remains at about 80% of the initial value at 25°C with increasing temperature up to 150°C, which indicates that the $(K_{0.64}Na_{0.35}Eu_{0.01})Mg_4(PO_4)_3$ phosphor has excellent thermal stability in the temperature quenching effect. Furthermore, it is well known that the emission wavelength of the Eu^{2+} $4f^65d^1 \rightarrow 4f^7$ transition was shifted to the shorter wavelength side with increasing temperature, and that the peak shift usually causes a reduction of the color rendering index of optical devices.[161-163,173] In the present $(K_{0.64}Na_{0.35}Eu_{0.01})Mg_4(PO_4)_3$ phosphor, however, the emission band wavelength at 450 nm maintains its position with a temperature increase from 25 to 150°C, as shown in Fig. 7.6 (b). This result also shows that the $(K_{0.64}Na_{0.35}Eu_{0.01})Mg_4(PO_4)_3$ phosphor has high thermal stability.

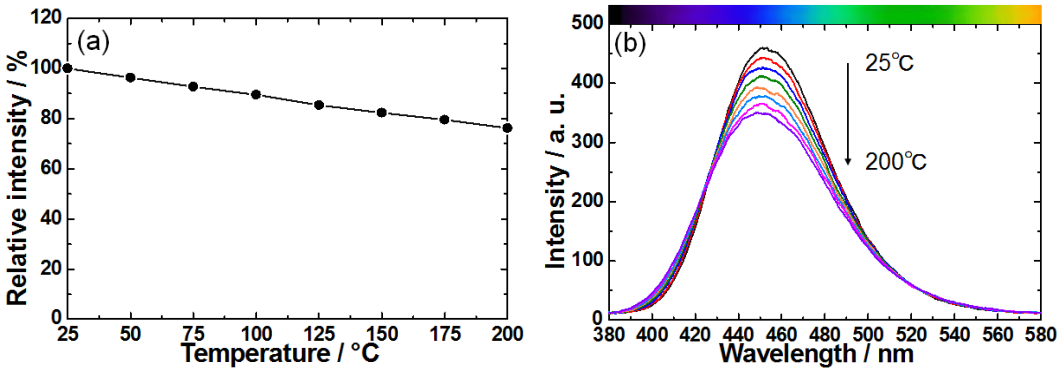

Fig. 7.6 The temperature dependence of the emission intensity (a) and the emission spectra (b) of the $(K_{0.64}Na_{0.35}Eu_{0.01})Mg_4(PO_4)_3$ phosphor under excitation at 254 nm.

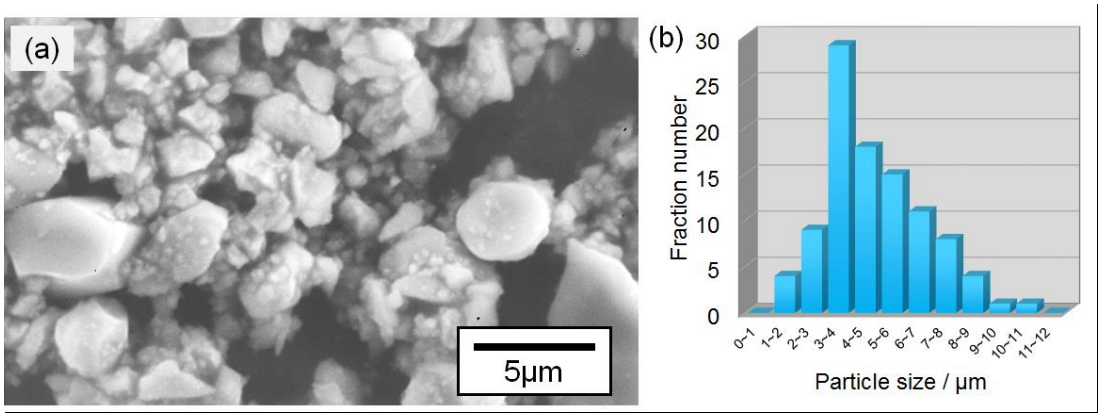

Fig. 7.7 SEM image (a) and the size distribution histogram (b) of the $(K_{0.64}Na_{0.35}Eu_{0.01})Mg_4(PO_4)_3$ phosphor.

Figure 7.7 presents the SEM image (a) and the size distribution histogram (b) of the $(K_{0.64}Na_{0.35}Eu_{0.01})Mg_4(PO_4)_3$ phosphor. The size distribution and mean particle size of the phosphor were estimated by measuring the diameters of the 100 particles on the SEM photographs. It is obvious that the sample obtained in the present study had a granular particle morphology, and that its average particle size was 4μm.

In the present state, although the luminescence efficiency of this phosphor is not sufficient, the critical Eu^{2+} concentration in this phosphor is 1/10 that of the commercial blue-emitting $BaMgAl_{10}O_{17}:Eu^{2+}$ phosphor, which indicates that (K, Na)$Mg_4(PO_4)_3:Eu^{2+}$ phosphors can be applied to optical devices. Furthermore, the improvement of the luminescence properties of this phosphor can be expected through the optimization of the particle morphology and size as well as of the preparation process, such as the flux method.

7.4 Summary

Blue-emitting $(K_{1-x}Na_xEu_y)Mg_4(PO_4)_3$ ($0 \le x \le 0.40$, $0.005 \le y \le 0.07$) phosphors were synthesized in a single-phase form with high crystallinity through the conventional solid-state reaction method. The photoluminescence spectra of the phosphors showed blue emission from the $4f^65d^1$ excited state to the $4f^7$ ground state of Eu^{2+}, and the emission peak intensity was effectively enhanced by Na^+ doping into the host $KMg_4(PO_4)_3$ lattice. The highest emission peak intensity was obtained for $(K_{0.64}Na_{0.35}Eu_{0.01})Mg_4(PO_4)_3$, where the relative emission peak intensity was 33% of that for the commercial blue-emitting $BaMgAl_{10}O_{17}:Eu^{2+}$ phosphor. In addition, the $(K,Na)Mg_4(PO_4)_3:Eu^{2+}$ phosphors were shown to have excellent thermal stability in the temperature quenching effect.

Chapter 8

Concluding remarks

Blue light excitable red-emitting phosphors have been attracted much attention for a new white-LEDs with a high CRI. However, the design concept for obtaining a red emission have not been established. In order to reveal the relation between the luminescence properties and crystallographic coordination, the luminescence properties of the Ce^{3+} and Eu^{2+} with high symmetric coordination in novel phosphors have been investigated. The photoluminescence properties of these phosphors were discussed. The results are summarized as follows;

1. In the chapter 2 to chapter 6, the series of new Ce^{3+}-activated oxide phosphors, which consist of the rare earth elements (Y or Sc) in the host composition, were discovered by high temperature reactions. These host materials are composed of the compact REO_n (*RE* = rare earth; n = 6 or 7) polyhedral with higher symmetry, and the Ce^{3+} ion located in such coordination environment were found to exhibit a longer wavelength side emission than yellow region under the blue-light excitation. To the best our knowledge, the emission with red spectral region more than 600 nm was first report in the Ce^{3+}-activated oxide phosphors.

2. From the results of calculation of the excited 5d positions proposed by Dorenbos, the rare earth host materials tended to cause a large centroid shift (Table 8.1), thereby those emission are easily observed at the long wavelength side. In addition, the large Stokes shift was also observed in the rare earth oxide hosts,

Table 8.1 The emission (λ_{em}) and excitation (λ_{ex}) band positions, coordination number of Ce^{3+}, Stokes shift (ΔS), centroid shift (ε_c) and red shift (D(A)) of the discovered Ce^{3+}-doped phosphors in this thesis.

Phosphors		CN[a]	λex	λem	ΔS	ε_c	D(A)
Host	Ce doping site		(nm)	(nm)	(cm^{-1})	(cm^{-1})	(cm^{-1})
$Sr_3Sc_4O_9$	Sc	6	425	620	7400	-[b]	25800
$Ba_3Sc_4O_9$	Sc	6	430	583	8930	22900	26100
$Y_{17.33}B_8O_{35}$	Y1	8	360	416	2270	7860	21700
	Y2	7	424	642	6510	15300	25700
$LiSr_2YO_4$	Sr	6	443	611	6200	~20100	26800
	Y	6	443	650	7190	23200	
$BaCa_2Y_6O_{12}$	Ca	6	460	632	5900	11600	27600
	Y	6	460	680	7000	18800	

[a]Coordination number.
[b]Detailed crystal structure is unknown.

and these values were comparable to that of the Ce^{3+} activated simple and transition metal oxide phosphors.

3. Unfortunately, thermal stabilities of these Ce^{3+}-activated phosphors were not very high. This results explained that the Stokes shift of the phosphors are quite large. Although the Ce^{3+} doped rare earth oxides showed red emission, they are not easy to apply for white-LED as a red component.

4. In Chapter 3 to 5, the two deferent emission bands are observed in the single host lattice. It is revealed that the emission bands are due to the Ce^{3+} ion occupied into two different site. As the result, the emission spectra were caused a significantly broad band, which is expected to lead the higher CRI. Furthermore, the emission band intensities could be controlled by the heterogeneous ion doping.

5. In chapter 6 and 7, we have developed the two Eu^{2+}-activated phosphate phosphors, olivine-type $NaMgPO_4:Eu^{2+}$ with a red emission and $(K,Na)Mg_4(PO_4)_3:Eu^{2+}$ with a blue emission. Although these phosphors were

composed of the similar elements, these phosphors exhibited a significantly different luminescence properties. This results could be considered that the coordination environment of Eu^{2+} were largely different, which caused to the strong crystal field in the olivine-type $NaMgPO_4$.

As mentioned above, the novel Ce^{3+}- and Eu^{2+}-doped phosphors having the high symmetry polyhedron exhibited a longer wavelength emission. These results suggested that the Ce^{3+} or Eu^{2+} ions occupied to the compact polyhedral coordination show the longer wavelength emission. Therefore, a design concept "***Ce^{3+} and Eu^{2+} ions are arrangement on high symmetric crystal fields***" is useful for the white-LED, but also for the development of phosphor materials as a next-generation.

References

1) M. Sato, S.W. Kim, Y. Shimomura, T. Hasegawa, K. Toda and G. Adachi. *Rare Earth-Doped Phosphors for White Light-Emitting Diodes*" Handbook on the Physics and Chemistry of Rare Earths (2016), *in press*.

2) S. Nakamura, T. Mukai and M. Senoh, *Appl. Phys. Lett.*, 1994, **64**, 1687.

3) H. Amano, M. Kito, K. Hiramatsu and I. Akasaki, *Jpn. J. Appl. Phys.*, 1989, **28**, L2112.

4) H. Amano, N. Sawaki, I. Akasaki and Y. Toyoda, *Appl. Phys. Lett.*, 1986, **48**, 353.

5) H. Lin, B. Wang, J. Xu, R. Zhang, H. Chen, Y. Yu and Y. Wang, *ACS Appl. Mater. Interfaces*, 2014, **6**, 21264.

6) S. Lee and S. Seo, *J. Electrochem. Soc*., 2002, **149**, J85.

7) P. Schlotter, R. Schmidt and J. Schneider, *Appl. Phys. A*, 1997, **64**, 417.

8) S. Nakamura and G. Fasol, *The Blue Laser Diode*, Springer Verlag, Heidelberg, 1997.

9) F.M. Steranka, J.C. Bhat, D. Collins, L. Cook, M.G. Craford, R. Fletcher, N. Gardner, P. Grillot, W. Goetz, M. Keuper, R. Khare, A. Kim, M. Krames, G. Harbers, M. Ludowise, P.S. Martin, M. Misra, G. Mueller, R. Mueller-Mach, S. Rudaz, Y.C. Shen, D. Steigerwald, S. Stockman, S. Subramanya, T. Trottier and J.J. Wierer, *Phys. Status Solidi A*, 2002, **194**, 380.

10) H. Amano, *Seramikkusu*, 2012, **47**, 130.

11) K. Wang, X. Luo, Z. Liu, B. Zhou, Z. Gan and S. Liu, *Opt. Eng.*, 2008, **47**, 013002.

12) K. Narita, in *Phosphor Handbook*, ed. by M. W. Yen, S. Shionoya and H. Yamamoto, CRC Press, Boca Raton, New York, 2nd ed., 2007, Characteristics required for lamp phosphors, 445-449.

13) C.C. Lin and R.S. Liu, *J. Phys. Chem. Lett.*, 2011, **2**, 1268.

14) S. Kamiya and H. Mizuno, in *Phosphor Handbook*, ed. by M. W. Yen, S. Shionoya and H. Yamamoto, CRC Press, Boca Raton, New York, 2nd ed., 2007, Practical lamp phosphors, 451-494.

15) H. Tamaki and Y. Miyazaki, in *Phosphor Handbook*, ed. by M. W. Yen, S. Shionoya and H. Yamamoto, CRC Press, Boca Raton, New York, 2nd ed., 2007, Phosphors for white light-emitting diodes, 533-543.

16) G. Blasse and A. Bril, *Appl. Phys. Lett.*, 1967, **11**, 53.

17) C.C. Lin, A. Meijerink and R.S. Liu, *J. Phys. Chem. Lett.*, 2016, **7**, 495.

18) W.B. Im, Y.I. Kim, N.N. Fellows, H. Masui, G.A. Hirata, S.P. DenBaars and R. Seshadri, *Appl. Phys. Lett.*, 2008, **93**, 091905.

19) J. McKittrick and L.E. Shea-Rohwer, *J. Am. Ceram. Soc.*, 2014, **97**, 1327.

20) J. Zhang, X. Zhang, M. Gong, J. Shi, L. Yu, C. Rong and S. Lian, *Mater. Lett.*, 2012, **79**, 100.

21) S.W. Kim, T. Hasegawa, T. Ishigaki, K. Uematsu, K. Toda and M. Sato, *ECS Solid State Lett.*, 2013, **2**, R49.

22) Y. Sato, H. Kato, M. Kobayashi, T. Masaki, D.H. Yoon and M. Kakihana, *Angew. Chem. Int. Ed.*, 2014, **53**, 7756.

23) D. Deng, H. Yu, Y. Li, Y. Hua, G. Jia, S. Zhao, H. Wang, L. Huang, Y. Li, C. Li and S. Xu, *J. Mater. Chem. C*, 2013, **1**, 3194.

24) N. Komuro, M. Mikami, P.J. Saines and A.K. Cheetham, *J. Lumin.*, 2015, **162**, 25.

25) N. Komuro, M. Mikami, P.J. Saines, K. Akimoto and A.K. Cheetham, *J. Mater. Chem. C*, 2015, **3**, 7356.

26) K. Uheda, N. Hirosaki, Y. Yamamoto, A. Naito, T. Nakajima and H. Yamamoto, *Electrochem. Solid State Lett.*, 2006, **9**, H22.

27) Y.Q. Li, J.E.J. van Steen, J.W.H. van Krevel, G. Botty, A.C.A. Delsing, F.J. DiSalvo, G. de With and H.T. Hintzen, *J. Alloys Compd.*, 2006, **417**, 273.

28) P. Pust, V. Weiler, C. Hecht, A. Tücks, A.S. Wochnik, A.K. Henß, D. Wiechert, C. Scheu, P.J. Schmidt and W. Schnick, *Nat. Mater.*, 2014, **13**, 891.

29) T.M. Tolhurst, T.D. Boyko, P. Pust, N.W. Johnson, W. Schnick and A. Moewes, *Adv. Optical Mater.,* 2015, **3**, 546.

30) Y. Hu, W. Zhuang, H. Ye, S. Zhang, Y. Fang and X. Huang, *J. Lumin.*, 2005, **111**, 139.

31) L.G. van Uitert, *J. Lumin.*, 1984, **29**, 1.

32) R.J. Xie, N. Hirosaki, T. Takeda and T. Suehiro, *ECS J. Solid State Sci. Technol.*, 2013 **2**, R3031.

33) W.J. Yang and T.M. Chen, *Appl. Phys. Lett.*, 2006, **88**, 101903.

34) E.F. Schubert, J.K. Kim, *Science*, 2005, **308**, 1274.

35) Y. Narukawa, J. Narita, T. Sakamoto, T. Yamada, H. Narimatsu, M. Sano, and T. Mukai, *Phys. Status Solidi A*, 2007, **204**, 2087.

36) H. Daicho, T. Iwasaki, K. Enomoto, Y. Sasaki, Y. Maeno, Y. Shinomiya, S. Aoyagi, E. Nishibori, M. Sakata, H. Sawa, S. Matsuishi and H. Hosono, *Nat. Commun.* 2012, **3**, 1132.

37) S. Tezuka, Y. Sato, T. Komukai, Y. Takatsuka, H. Kato and M. Kakihana, *Appl. Phys. Express*, 2013, 6, 072101.

38) B. Ma, Z. Huang, M. Fang, Y. Liu and X. Wu, *RSC Adv.*, 2015, **5**, 9933.

39) Q. Dai, H. Song, M. Wang, X. Bai, B. Dong, R. Qin and X. Qu, H. Zhang, *J. Phys. Chem. C*, 2008, 112, 19399.

40) J. Huang, B. Hou, H. Ling, J. Liu and X. Yu, *Inorg. Chem.*, 2014, **53**, 9541.

41) S. Yan, J. Zhang, X. Zhang, S. Lu, X. Ren, Z. Nie and X. Wang, *J. Phys. Chem. C*, 2007, **111**, 13256.

42) S.H. Park, K.H. Lee, S. Unithrattil, H.S. Yoon, H.G. Jang and W.B. Im, *J. Phys. Chem. C*, 2012, **116**, 26850.

43) T. Kano, in *Phosphor Handbook*, ed. by M. W. Yen, S. Shionoya and H. Yamamoto, CRC Press, Boca Raton, New York, 2nd ed., 2007, Luminescence of rare earth ions, 191-214.

44) L. Zhang, Z. Lu, P. Han, L. Wang and Q. Zhang, *J. Mater. Chem. C*, 2013, **1**, 54.

45) S. Neeraj, N. Kijima and A.K. Cheetham, *Chem. Phys. Lett.*, 2004, **387**, 2.

46) G. Blasse and A. Bril, *Philips Res. Rep.*, 1967, **22**, 481.

47) S. Schmiechen, H. Schneider, P. Wagatha, C. Hecht, P.J. Schmidt and W. Schnick, *Chem. Mater.*, 2014, **26**, 2712.

48) P. Pust, A.S. Wochnik, E. Baumann, P.J. Schmidt, D. Wiechert, C. Scheu and W. Schnick, *Chem. Mater.*, 2014, **26**, 3544.

49) C.J. Duan, X.J. Wang, W.M. Otten, A.C.A. Delsing, J.T. Zhao and H.T. Hintzen, *Chem. Mater.*, 2008, **20**, 1597.

50) C. Hecht, F. Stadler, P.J. Schmidt, J.S. auf der Gunne, V. Baumann, and W. Schnick, *Chem. Mater.*, 2009, **21**, 1595.

51) A.P. Black, K.A. Denault, J.O. Sole and A.R. Goni, *Chem. Commun.*, 2015, **51**, 2166.

52) Y. Kawano, S.W. Kim, T. Ishigaki, K. Uematsu, K. Toda, H. Takaba and M. Sato, *Opt. Mater. Express*, 2014, **4**, 1770.

53) A.A. Setlur, W.J. Heward, Y. Gao, A.M. Srivastava, R.G. Chandran and M.V. Shankar, *Chem. Mater.*, 2006, **18**, 3314.

54) Y.Q. Li, A.C.A. Delsing, G. de With and H.T. Hintzen, *Chem. Mater.*, 2005, **17**, 3242.

55) R. Le Toquin and A.K. Cheetham, *Chem. Phys. Lett.*, 2006, **423**, 352.

56) G. Blasse and B. C. Grabmaier, *Luminescent Materials*, Springer Verlag, Berlin, 1994.

57) P. Dorenbos, *J. Lumin.*, 2003, **104**, 239.

58) P. Dorenbos, in *Phosphor Handbook*, ed. by M. W. Yen, S. Shionoya and H. Yamamoto, CRC Press, Boca Raton, New York, 2nd ed., 2007, Lanthanide level location and its impact on phosphor performance, 139-154.

59) V.I. Spitsyn, L.M. Kovba, M.V. Peromova, I.V. Yudinskaya and I. G. Prokof'eva, *Dokl. Akad. Nauk SSSR,* 1968, **180**, 879.

60) K. Momma and F. Izumi, *J. Appl. Cryst.*, 2000, **41**, 653.

61) R.D. Shannon, *Acta Crystallogr. Sect. A*, 1976, **32**, 751.

62) J.C. Grivel, N.H. Andersen, *J. Alloys Compd.*, 2005, **391**, 292.

63) F. Izumi and K. Momma, *Solid State Phenom.*, 2007, **130**, 15.

64) H. Zhu, C.C. Lin, W. Luo, S. Shu, Z. Liu, Y. Liu, J. Kong, E. Ma, Y. Cao, R.S. Liu and X. Chen, *Nat. Comm.*, 2014, **5**, 4312.

65) I.D. Brown and D. Altermatt, *Acta Crystallogr. B*, 1985, **41**, 244.

66) Y.C. Wu, Y.C. Chen, D.Y. Wang, C.S. Lee, C.C. Sun and T.M. Chen, *J. Mater. Chem.*, 2011, **21**, 15163.

67) T. Hasegawa, H. Kato, Y. Takatsuka, M. Kobayashi, H. Yamane and M. Kakihana, *ECS J. Solid State Sci. Technol.*, 2013, **2**, R3107.

68) A. Kalaji, M. Mikami and A.K. Cheetham, *Chem. Mater.*, 2014, **26**, 3966.

69) P. Dorenbos, *J. Lumin.*, 2000, **91**, 91.

70) P. Dorenbos, *J. Lumin.*, 2008, **128**, 578.

71) K. Uheda, N. Hirosaki and H. Yamamoto, *Phys. Status Solidi A*, 2006, **203**, 2712.

72) H. Watanabe and N. Kijima, *J. Alloys Compd.*, 2009, **475**, 434.

73) Y. Luo and Z. Xia, *J. Phys. Chem. C*, 2014, **118**, 23297.

74) J. Zhong, W. Zhuang, X. Xing, R. Liu, Y. Li, Y. Liu and Y. Hu, *J. Phys. Chem. C*, 2015, **119**, 5562.

75) G. Blasse, *J. Solid State Chem.*, 1986, **62**, 207.

76) Y. Shimomura, T. Kurushima and N. Kijima, *J. Electrochem. Soc.*, 2007, **154**, J234.

77) Y.Q. Li, N. Hirosaki, R.J. Xie, T. Takeda and M. Mitomo, *Chem. Mater.*, 2008, **20**, 6704.

78) T. Suehiro, N. Hirosaki and R.J. Xie, *ACS Appl. Mater. Interfaces*, 2011, **3**, 811.

79) Z. Hao, X. Zhang, X. Wang and J. Zhang, *Mater. Lett.*, 2012, **68**, 443.

80) M. Müller, M.F. Volhard and T. Jüstel, *RSC Adv.*, 2016, **6**, 8483.

81) Y.S. Tang, S.F. Hu, W.C. Ke, C.C. Lin, N.C. Bagkar and R.S. Liu, *Appl. Phys. Lett.*, 2008, **93**, 131114.

82) S. Kubota, Y. Suzuyama, H. Yamane and M. Shimada, *J. Alloys Compd.*, 1992, **268**, 66.

83) Y. Sang, D. Yu, M. Avdeev, H. Qin, J. Wang, H. Liu and Y. Lv, *J. Solid State Chem.*, 2012, **192**, 366.

84) M. Tamatani, in *Phosphor Handbook*, ed. by M. W. Yen, S. Shionoya and H. Yamamoto, CRC Press, Boca Raton, New York, 2nd ed., 2007, Luminescence

centers of transition metal ions, 167-190.

85) H. Baernighausen, *Z. Anorg. Allg. Chem.*, 1967, **349**, 280.

86) H. Baernighausen, *Z. Anorg. Allg. Chem.*, 1970, **374**, 201.

87) T. Hasegawa, S.W. Kim, T. Ishigaki, K. Uematsu, H. Takaba, K. Toda and M. Sato, *Chem. Lett.*, 2014, **43**, 828.

88) A. Katelnikovas, H. Bettentrup, D. Uhlich, S. Sakirzanovas, T. Jüstel, and A. Kareiva, *J. Lumin.*, 2009, **129**, 1356.

89) C.K. Chang, and T.M. Chen, *Appl. Phys. Lett.*, 2007, **91**, 081902.

90) I. Szczygiel, L. Macalik, T. Znamierowska and J. Hanuza, *J. Alloy. Compd.*, 2004, **380**, 274.

91) B. Henderson and G.F. Imbush, *Optical spectroscopy of Inorganic Solids*, Oxford University, Clarendon, Oxford, 1989.

92) V. Bachmann, C. Ronda and A. Meijerink, *Chem. Mater.*, 2009, **21**, 2077.

93) E.V. Kolk, S.A. Basun, G.F. Imbusch and W.M. Yen, *Appl. Phys. Lett.*, 2003, **83**, 1740.

94) W.M. Yen, *Opt. Mater.*, 2005, **27**, 1647.

95) J. Ueda, S. Tanabe and T. Nakanishi, *J. Appl. Phys.*, 2011, **110**, 053102.

96) C.H. Huang and T.M. Chen, *Inorg. Chem.*, 2011, **50**, 5725.

97) A.A. Setlur, E.V. Radkov, C.S. Henderson, J.H. Her, A.M. Srivastava, N. Karkada, M.S. Kishore, N.P. Kumar, D. Aesram, A. Deshpande, B. Kolodin, L.S. Grigorov and U. Happek, *Chem. Mater.*, 2010, **22**, 4076.

98) J.H. Lin, S. Zhou, L.Q. Yang, G.Q. Yao, M.Z. Su and L.P. You, *J. Solid State Chem.*, 1997, **134**, 158.

99) L. Zhang, J. Zhang, X. Zhang, Z. Hao, H. Zhao and Y. Luo, *ACS Appl. Mater. Interfaces*, 2013, **5**, 12839.

100) K.A. Denault, N.C. George, S.R. Paden, S. Brinkley, A.A. Mikhailovsky, J. Neuefeind, S.P. DenBaars and R. Seshadri, *J. Mater. Chem.*, 2012, **22**, 18204.

101) Y. He, J. Zhang, W. Zhou, J. Han, Z. Qiu, L. Yu, C. Rong and S. Lian, *J. Am. Ceram.*

Soc., 2014, **97**, 1517.

102) H. Hara, S. Takeshita, T. Isobe, Y. Nanai, T. Okuno, T. Sawayama and S. Niikura, *J. Alloys Compd*., 2013, **577**, 320.

103) C. Liu, H. Liang, X. Kuang, J. Zhong, S. Sun and Y. Tao, *Inorg. Chem.*, 2012, 51, 8802.

104) P. Dorenbos, *Phys. Rev. B*, 2000, **62**, 15640.

105) P. Dorenbos, *Phys. Rev. B*, 2001, **64**, 125117.

106) P. Dorenbos, *J. Lumin.*, 2002, **99**, 283.

107) R.j. Lang, *Can. J. Res.*, 1936, **14**, 127.

108) W.B. Im, S. Brinkley, J. Hu, A. Mikhailovsky, S.P. DenBaars and R. Seshadri, R. *Chem. Mater.*, 2010, **22**, 2842.

109) P. Dorenbos, *Phys. Rev. B*, 2002, **65**, 235110.

110) P. Dorenbos, *J. Lumin.*, 2003, **105**, 117.

111) P. Dorenbos, *J. Lumin.*, 2000, **91**, 155.

112) J.W.M. Verwey, G.J. Dirksen and G. Blasse, *J. Phys. Chem. Solids*, 1992, **53**, 367.

113) F.W. Tian, C. Fouassier and P. Hagenmuller, *Mater. Res. Bull.*, 1987, **22**, 389.

114) H. Zhiran and G. Blasse, *Mater. Chem. Phys.*, 1985, **12**, 257.

115) W. van Schaik, S.H.M. Poort, J.J.H. Schlotter, E. Dorrestijn and G. Blasse, *J. Electrochem. Soc.*, 1994, **141**, 2201.

116) L. Guerbous, M. Seraiche and O. Krachni, *J. Lumin.*, 2013, **134**, 165.

117) O. Lebbou, C. Dujardin, C. Goutaudier, M.T. Cohen-Adat, C. Pedrini, B. Moine and A.N. Belsky, *preprint for the Proceedings of the 5th International Conference on Inorganic Scintillators and Their Applications*, Moscow, Russia, August 16-20, 1999.

118) L. Zhang, *Elaboration et proprietes de luminescence et de scintillation de materiaux denses a base de lutecium dopes aux ions cerium et praseodyme*; Thesis, l'Universite Claude Bernard-Lyon I, 1997.

119) M. Knitel, *New Inorganic Scintillators and Storage Phosphors for Detection of Thermal Neutrons*; Delft Univ. Press: Delft, 1998.

120) G. Blasse, *J. Inorg. Nucl. Chem.*, 1969, **31**, 1519.

121) T. Tomiki, T. Kohatsu, H. Shimabukuro and Y. Ganaha, *J. Phys. Soc. Jpn.*, 1992, **61**, 2382.

122) R.J. Xie and N. Hirosaki, *Sci. Technol. Adv. Mat.*, 2007, **8**, 588.

123) J.W.H. van Krevel, H.T. Hintzen, R. Metselaar and A. Meijerink, *J. Alloys Compd.*, 1998, **268**, 272.

124) S. Bhushan and M.V. Chukichev, *J Mater Sci Lett.*, 1988, **7**, 319.

125) R.C. Ropp, *Encyclopedia of the Alkaline Earth Compounds*, Elsevier, Oxford, UK, 2013.

126) H. Müller-Buschbaum and R. von Schenk, *Z. Anorg. Allg. Chem.*, 1970, **377**, 70.

127) H. Karunadasa, Q. Huang, B.G. Ueland, J.W. Lynn, P. Schiffer, K.A. Regan and R.J. Cava, *Phys. Rev. B*, 2005, **71**, 144414.

128) H. Kobayashi, H. Ogino, K. Nakamura, T. Mori, H. Yamamura and T. Mitamura, *J. Ceram. Soc. Jpn.*, 1994, **102**, 583.

129) T. Besara, M.S. Lundberg, J. Sun, D. Ramirez, L. Dong, J.B. Whalen, R. Vasquez, F. Herrera, J.R. Allen, M.W. Davidson and T. Siegrist, *Prog. Solid State Ch.*, 2014, **42**, 23.

130) H.T. Hintzen, H.A. M. van Hal, C. Langereis and C.J. M. Denissen, *J. Less Common Metals*, 1989, **155**, 291.

131) F. Schröder and H. Müller-Buschbaum, *J. Less Common Metals*, 1986, **116**, 211.

132) C.K. Jurgensen, *Absorptoin Spectra and Chemical Bonding in Complexes*, Pergamon Press, Elmsford, N.Y., (1962).

133) L. Chen, C.C. Lin, C.W. Yeh and R.S. Liu, *Materials*, 2010, **3**, 2172.

134) T. Yamada, M. Yoshimura and S. Somiya, *J. Am. Ceram. Soc.*, 1986, **69**, C243.

135) T. Yamada, M. Yoshimura and S. Somiya, *High Temp. High Press.*, 1986, **18**, 377.

136) T. Ishigaki, M. Yoshimura, N. Matsushita, K. Uematsu, K. Toda and M. Sato, *J. Eur.*

Ceram. Soc., 2010, **30**, 165.

137) T. Ishigaki, K. Toda, M. Yoshimura, K. Uematsu and M. Sato, *Sci. Technol. Adv. Mater.*, 2011, **12**, 054205.

138) T. Ishigaki, K. Toda, T. Watanabe, N. Sakamoto, N. Matsushita and M. Yoshimura, *J. Mater. Sci.*, 2008, **43**, 4749.

139) S.W. Kim, T. Hasegawa, T. Ishigaki, K. Uematsu, K. Toda and M. Sato, *ECS Solid State Lett.*, 2013, **2**, R49.

140) K. Sugimoto, S.W. Kim, K. Uematsu, T. Ishigaki, K. Toda and M. Sato, *J. Ceram. Soc. Jpn.*, 2015, **123**, 880.

141) Y.C. Wu, Y.C. Chen, T.M. Chen, C.S. Lee, K.J. Chen and H.C. Kuo, *J. Mater. Chem.*, 2012, **22**, 8048.

142) Y. Pan, M Wu and Q Su, *J. Phys. Chem. Solids*, 2004, **65**, 845.

143) P. Dorenbos, *J. Phys.: Condens. Matter*, 2003, **15**, 4797.

144) G. Blasse and A. Bril, *J. Chem. Phys.*, 1967, **47**, 5139.

145) W. Chen, H. Liang, B. Han, J. Zhong and Q. Su, *J. Phys. Chem. C*, 2009, **113**, 17194.

146) R.J. Xie, N. Hirosaki, N. Kimura, K. Sakuma and M. Mitomo, *Appl. Phys. Lett.*, 2007, **90**, 191101.

147) Q. Zhang, H. Ni, L. Wang and F. Xiao, *ECS J. Solid State Sci. Technol.*, 2015, **4**, R23.

148) C. Wu and Y. Wang, *Mater. Lett.*, 2007, **61**, 2416.

149) Z.C. Wu, J.X. Shi, J. Wang, M.L. Gong and Q. Su, *J. Solid State Chem.*, 2006, **179**, 2356.

150) Z.C. Wu, J.X. Shi and M.L. Gong, *Mater. Chem. Phys.*, 2007, **103**, 415.

151) Y.S. Tang, S.F. Hu, C.C. Lin, N.C. Bagkar and R.S. Liu, *Appl. Phys. Lett.*, 2007, **90**, 151108.

152) C. Qin, Y. Huang, L. Shi, G. Chen, X. Qiao and H.J. Seo, *J. Phys. D: Appl. Phys.*, 2009, **42**, 185105.

153) C.C. Lin, Y.S. Tang, S.F. Hu and R.S. Liu, *J. Lumin.*, 2009, **129**, 1682.

154) W.B. Im, H.S. Yoo, S. Vaidyanathan, K.H. Kwon, H.J. Park, Y.I. Kim and D.Y. Jeon, *Mater. Chem. Phys.*, 2009, **115**, 161.

155) W. Tang and Y. Zheng, *Luminescence*, 2010, **25**, 364.

156) W. Tang, D. Chen and H. Yang, *Appl. Phys. A*, 2011, **103**, 263.

157) K.C. Park, H.C. Ahn, H.D. Nguyen, H.Y. Jang and S.I. Mho, *J. Kor. Phys. Soc.*, 2008, **53**, 2220.

158) T. Ishigaki, N. Matsushita, M. Yoshimura, K. Uematsu, K. Toda and M. Sato, *Phys. Procedia*, 2009, **2**, 587.

159) H. Imura and A. Kawahara, *Acta Crystallogr. B*, 1991, **47**, 192.

160) F. Hanic, M. Handlovic, K. Burdova and J. Majling, *J. Crystallogr. Spectrosc. Res.*, 1982, **12**, 99.

161) X. Piao, K. Machida, T. Horikawa and B. Yun, *J. Lumin.*, 2010, **130**, 8.

162) C. Qin, Y. Huang, L. Shi, G. Chen, X. Qiao and H.J. Seo, *J. Phys. D: Appl. Phys.*, 2009, **42**, 185105.

163) J.S. Kim, Y.H. Park, S.M. Kim, J.C. Choi and H.L. Park, *Solid State Commum.*, 2005, **133**, 445.

164) Z. Wu, J. Liu, M. Gong and Q. Su, *J. Electrochem. Soc.*, 2009, 156, H153.

165) P.E. Tomaszewski, M. Maczka, A. Majchrowski, A. Waskowska and J. Hanuza, *Solid State Sci.*, 2005, **7**, 1201.

166) M. Ben Amara, M. Vlasse, R. Olazcuaga, G. Le Flem and P. Hagenmuller, *Acta Crystallogr. C*, 1983, **39**, 936.

167) J. Berak and T. Podhajska-Kazmierczak, *Pol. J. Chem.*, 1991, **65**, 1137.

168) C. Wu and Y. Wang, *Mater. Lett.*, 2007, **61**, 2414 (2007).

169) Z.C. Wu, J.X. Shi and M.L. Gong, *Mater. Chem. Phys.*, 2007, **103**, 415.

170) L. Lan, H. Feng, Y. Tang and W. Tang, *Opt. Mater.*, 2011, **34**, 175.

171) X. Lan, Q. Wei, Y. Chen and W. Tang, *Opt. Mater.*, 2012, **34**, 1330.

172) Kravchenko, *Opt. Laser Technol.*, 1982, **14**, 189.

173) R. Yu, H. Li, H. Ma, C. Wang, H. Wang, B.K. Moon and J.H. Jeong, *J. Lumin.*, 2012, **132**, 2783.

Acknowledgement

The author would like to express his sincere gratitude to my supervisor, Associate Professor Dr. Kenji Toda, Graduate School of Science and Technology, Niigata University, for giving him this precious study opportunity as a Ph. D candidate student in Toda's research group.

The author would deeply like to thank Professor Dr. Mineo Sato, Assistant Professor Dr. Atsushi Itadani, Research Assistant Professor Dr. Sun-wook Kim, Dr. Kazuyoshi Uematsu (ex-Technical Officer) and Postdoctoral researcher Dr. Dai Okada, Niigata University, for their great advises, suggestions and encouragements. The author would also like to thank Associate Professor Dr. Naoki Kano, Niigata University, for their kind informative suggestions in this thesis.

The author also thanks the co-workers, Ms. Mizuki Watanabe, Mr. Ryota Yamanashi, Mr. Shota Kumagai, Mr. Masaru Muto and Mr. Minenori Katsu for their assistance, and all other members of Toda's and Sato's research groups for their helpful and valuable experimental suggestions.

Finally, the author has sincerely grateful to his family, Mitsuhiro Hasegawa, Ikuko Hasegawa, Atsushi Hasegawa and Aki Hasegawa, for providing him a chance to study again at Niigata University.